UNIVERSITÀ DI PISA

PHD IN CHEMISTRY AND MATERIALS SCIENCE

XXX cycle (2015-2017)

PhD thesis

Designed amphiphilic polymers: self-assembly and nanostructure in solution and in thin film

Candidate: Elisa Guazzelli

Supervisors:

Prof. Giancarlo Galli

Dr. Elisa Martinelli

Coordinator:

Prof. Lorenzo di Bari

“There are two possible outcomes:
if the result confirms the hypothesis, then you've made a measurement.
If the result is contrary to the hypothesis, then you've made a discovery.”
E. Fermi

ABSTRACT

Different classes of amphiphilic copolymers were designed to incorporate both hydrophilic and hydrophobic components which could enable investigation of their distinct self-assembly and nanostructure over various states from solution in selective solvents to surface of thin solid films. By taking advantage of the controlled nature of the reversible-deactivation radical polymerisation methods, namely ATRP and RAFT, copolymers with diverse chemical architectures and structures were prepared with a tailored and varied philic/phobic balance. Comonomers, such as those based on a hydrophilic polyethyleneglycol methacrylate, a hydrophobic and lipophobic fluoroalkyl acrylate, a hydrophobic polysiloxane methacrylate, and two hydrolysable trialkylsilyl methacrylates, were selected in order to provide the materials with functional and responsive characters in addition to the capacity of self-assembling and structuring over length scales.

Amphiphilic ATRP random copolymers of polyethyleneglycol methacrylate and either fluoroalkyl acrylate or polysiloxane methacrylate were identified as single-chain folding polymers, where hydrophobic intramolecular interactions led to the copolymer self-assembly in solution to form unimer micelles. Dynamic light scattering (DLS) and small angle neutron scattering (SANS) experiments confirmed the formation of nanosized, unimer micelles at room temperature which turned into collective nano-to-microsized aggregates above a critical transition temperature. Fluorescent molecular probes were used to further investigate the properties of the nanostructures obtained. Molecular dynamics (MD) simulations were carried out to evaluate folding trajectories of the amphiphilic copolymers and supported the single-chain folding model proposed with conformational details. The interaction and self-assembly of hydrophobic side chains in the solid state were evidenced by NMR relaxometry studies of ^{1}H and ^{19}F nuclei. Moreover, the nanostructured, outer surface of thin copolymer films was shown to be preferentially populated by perfluoralkyl chains by angle-resolved X-ray photoemission spectroscopy (AR-XPS) analyses.

Amphiphilic hydrolysable RAFT block copolymers were synthesised with the aim to develop surface-active materials for new marine antifouling/fouling

release coatings. Low elastic modulus and low surface energy were key parameters of the coating envisaged to combat fouling in a way to interfere with aquatic foulant adhesion and favour the biomass removal. These two features were combined in a silicone matrix-based coating that contained the surface-active amphiphilic copolymer carrying labile trialkylsilyl ester moieties at the surface of the film. The responsiveness to the outer environment mediated the reconstruction of the surface at the polymer-water interface to gradually renovate the surface and sustain high efficacy over time without the use of any toxic biocide. Wettability of model coatings was investigated with sessile drop and captive air bubble contact angle measurements. Antifouling and fouling release properties were assessed during a campaign of field immersion tests in natural seawater in Toulon (France) bay by regular and periodic inspections of coatings during seventeen weeks. Adhesion of different foulants, including biofilm, soft foulants and hard foulants, was evaluated which permitted to identify an intensity factor (I) and a severity factor (S) with a corresponding efficacy factor (N) to estimate the bounty of the antifouling potential. Removal of adhered biomass was also evaluated by sponge cleaning the coatings, which pointed to the effectiveness of the fouling-release performance.

ACKNOWLEDGEMENTS

I want to express my sincere gratitude to my supervisors: Prof Galli and Dr Martinelli, that guided me in this path of human and scientific growth.

This work was developed in the Department of Chemistry and Industrial Chemistry of the University of Pisa, taking advantage of the fruitful exchange with many local collaborators. Prof Pucci and Dr Biver for their precious help in fluorescence spectroscopy experiments. Prof Geppi, with Dr Borsacchi and Dr Martini, thank worked on the NMR relaxometry study. Prof Mennucci, with Dr Jurinovich, Dr Cupellini and Dr Caprasecca, that worked on the molecular dynamic simulation.

During the years, other solid collaborations were exploited with other italian and foreign institutions. Prof Glisenti (University of Padua) provided the XPS analysis. Prof Paradossi and Dr Domenici (University of Tor Vergata) and Dr Telling (ISIS, Oxford, UK), closely supported our work in DLS experiments and SANS measurements. All these people helped me expanding my knowledge with experimental contribution and support during the writing process of this dissertation.

Many thanks to Elena Masotti, Luisa Annunziata, Federico Perondi and Giulio Bottoni for their contribution to the preparation and characterisation of the materials presented in this thesis.

A special thank is due to Prof Bressy and all the group of people that work at MAPIEM laboratory in Toulon University, where I spent several wonderful months in 2017.

I really need to thank all my past and present labmates and all the polymer family inhabiting the labs 224 to 218 because in every difficult day, when everything goes wrong, or schedules were impossible, you always have an encouraging word, or something to make me smile again. Same here for the Fame group, that now comprehends some inorganic people: you always made my day, even if the Wang Friday never became a success (my fault, totally).

Sara, Alessia, Elena, Tiziana, Gabriele, Sabrina, Amanda and Jennifer you really are my life support system. I have to thank you, for the support during my phd (and before, and forever, I hope).

The last line is due to my family, that still supports me, even if I've become a *Pisana*.

TABLE OF CONTENTS

1 INTRODUCTION

This dissertation, presented in compliance of the requirements for the Doctoral School in Chemistry and Materials Science of the University of Pisa, is divided into three sections.

This first section will help the reader to understand the context where the work originates from. It begins with an introduction to the large and diversified topic of amphiphilic polymers, emphasising their peculiar self-assembly behaviour in selective solvents. An overview to the much less established field of random copolymer self-assembly will be given, with specific attention to the single-chain folding of synthetic polymers. Enabling a deeper comprehension of their unique spontaneous organisation and nanostructure is a first key objective of this work.

The study of molecular and supramolecular interactions is not trivial, and spectroscopic experiments may help to elucidate self-assembly processes, directly or indirectly. In particular, in this work a lot of effort was devoted to the use of fluorescent molecular rotors (FMR) to monitor aggregation phenomena of amphiphilic polymers. Thus, a brief chapter will describe the fluorescence behaviour of such class of fluorophores, that explains their suitability for the study of macromolecular self-assembly.

Amphiphilic polymers represent a formidable, versatile tool that assists researchers in addressing several industrial, biomedical and environmental issues. Antifouling coatings represent a clever example of the application of amphiphilic polymers to the development of a sustainable solution to economic and environmental concerns. The use of tailored amphiphilic copolymers and their self-assembly in solid state, for antifouling, fouling release marine coatings is a second key objective of this work. Therefore, a chapter will be devoted to the marine biofouling phenomenon and the strategies to mitigate related damages will be briefly examined.

Reversible-deactivation radical polymerisation (RDRP) techniques have allowed the fast development of polymer synthesis toward designed polymers

with a spectacular diversity of chemistries and architectures. Amphiphilic polymer chemistry flourished thanks to this progress, as well as many other fields in polymer science and application. All the copolymers proposed in this thesis were obtained through atom transfer radical polymerisation (ATRP) or reversible addition-fragmentation chain transfer (RAFT) polymerisation, with detailed kinetic studies. Hence, a brief overview of RDRP techniques, with some perspectives of their recent advances will be delivered in the last chapter of this introduction.

The subsequent two sections will report on the original research activity carried out during the last three years. One section will be devoted to the design and characterisation of unimer micelles of amphiphilic random copolymers by single-chain folding in solution, based on the driving force to self-assembly of hydrophilic polyethylene glycol methacrylate and on hydrophobic fluorinated or siloxane (meth)acrylates.

The third and last section of this thesis will report on the research activity developed at MAPIEM laboratory, in the SEATECH School of Engineering of the University of Toulon, with the kind guidance and hospitality of Prof Bressy. In this section the results from synthesis and characterisation of amphiphilic hydrolysable block copolymer for marine fouling release coatings will be reported. These were based on poly(dimethyl siloxane), hydrolysable silyl ester methacrylates and poly(ethylene glycol) methacrylate. Results of their biological performance in field immersion trials are included.

1.1 Amphiphilic polymers

In the literature, amphiphilic polymers are sometimes mentioned as polymeric surfactants, micellar polymers, hydrophobically modified water-soluble polymers, associative polymers, polyelectrolytes or polyampholytes (when they display charged moieties) and similar keywords.

The structural analogy with low molecular weight compounds is straightforward. The simultaneous presence of both hydrophilic and hydrophobic parts in the same macromolecule has been credited for their distinctive properties in solution. These include adsorption at interfaces and

self-assembly into a variety of micellar aggregates above a critical value of concentration, called critical micelle concentration (CMC, or critical aggregation concentration CAC). Actually, the term "solution" in this case should be used carefully, because above CMC the molecules are no longer homogeneously dissolved in the continuous phase.

Depending on the relative distribution of hydrophilic and lipophilic parts, three classes of amphiphilic polymers are commonly recognised (Figure 1).[1]

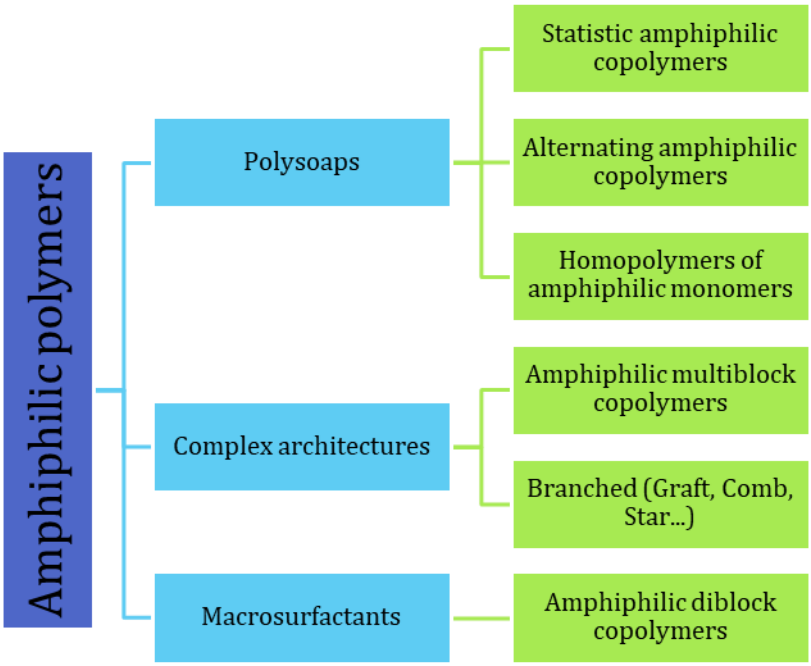

Figure 1: Classification of amphiphilic polymers.

Homopolymers of intrinsically amphiphilic monomers are generally defined polysoaps. Statistic, alternating or segmented multiblock copolymers of hydrophilic and hydrophobic monomers are generally included in this first class. On the contrary, polymers in which there is a neat separation between the hydrophilic/phobic parts are referred to as macrosurfactants. These include essentially amphiphilic linear, branched, and grafted block copolymers. The developments in precise and controlled polymeric synthesis made feasible several complex molecular architectures such as gradient, multiblock, star block, multibranched, and dendrimeric polymers, that can be considered as a different and new class of polymeric surfactant materials.

The most common hydrophobic components (Figure 2, left) are based on polystyrene, poly(meth)acrylates, polyolefin, nonwater-soluble polyethers, but it is also possible to find extremely hydrophobic and lipophobic segments, like fluorinated ones. The library of hydrophilic components is well assorted too (Figure 2, right). It comprehends either negatively or positively charged monomers, and some cases zwitterionic monomers, such as vinylic or (meth)acrylic monomers bearing sulfonated, carboxylic, or amino groups. Neutral components, which are essentially poly(ethylene glycol) (PEG) moieties or water-soluble (meth)acrylates such as 2-hydroxyethyl methacrylate (HEMA) or PEGylated (meth)acrylic monomers, are equally popular.

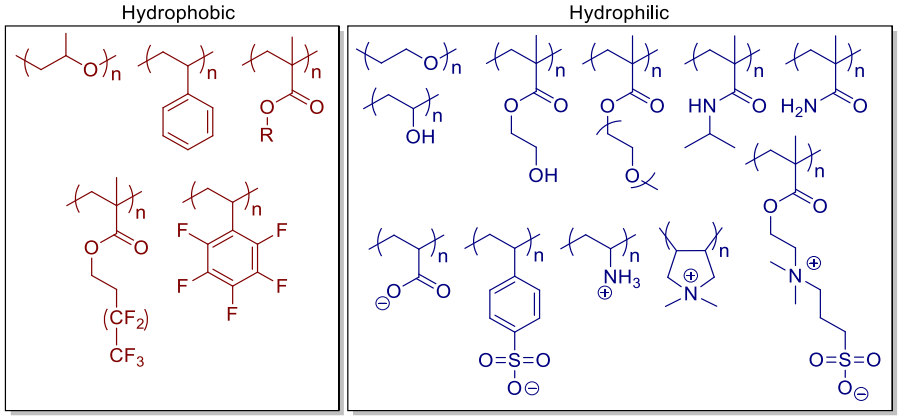

Figure 2: Common hydrophobic and hydrophilic structures in polymer chemistry, that can be combined in amphiphilic copolymers.

It is not surprising that amphiphilic polymers have received increasing attention in the last few decades for their actual and potential applications in several fields including (mini)emulsion polymerisations, coatings, biotechnology, nanotechnology, medicine, pharmacology, cosmetics, agriculture, water purification, electronic, optoelectronic, and enhanced oil recovery. Also of great interest from the applicative point of view is the possibility of introducing responsive behaviour to external parameters (such as pH, temperature, electrolyte concentration, and UV irradiation), which is at the basis of the design of smart materials.

The case of poloxamer (Figure 3), better known as Pluronic (block copolymer of polyethylene oxide PEO and polypropylene oxide PPO) is emblematic of how successful the evolution of a polymeric surfactants could be. Being a simple,

relatively low-cost material, it was first commercialised (by BASF) as industrial detergent.[2] It found afterwards important applications in cosmetic and in medicine as drug carriers.[3] In recent years, the interest in these polymers increased even more, as they showed potential in treatment of cancer.[4]

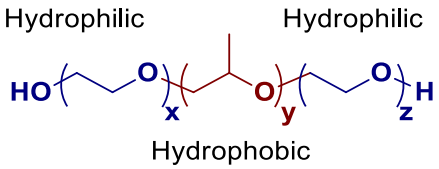

Figure 3: General structure of poloxamer amphiphilic copolymer.

An example of the influence of the different architecture on the properties of amphiphilic polymers is sketched in Figure 4. A polysoap (polymer of an intrinsically amphiphilic monomer or a random copolymer of hydrophilic and hydrophobic monomers) can undergo intramolecular aggregation in water. Block copolymers with hydrophilic and hydrophobic blocks, on the other hand, will mostly give intermolecular aggregation. Also, the arrangement at the water/air interface can be sensibly different. From this, completely different properties can be expected and are, in fact, observed. Little is known about the association behaviour of amphiphilic polymers characterised by complex architectures.

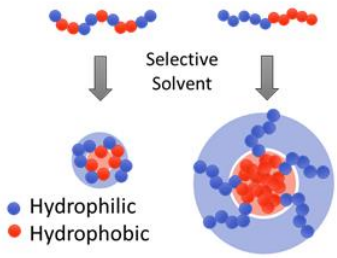

Figure 4: Schematic representation of the different behaviour displayed in solution by polysoaps (left) and macrosurfactants (right).

Ionic living polymerisation (especially anionic) has always been a method of choice for synthesising well-defined amphiphilic block copolymers and other complex structures.[5] However, after the development of reversible-deactivation radical polymerisation methods, such as NMP, ATRP and RAFT, the number of easily available compositions and structures has increased enormously. Details

will be given in a later chapter. These synthetic techniques have provided a really solid basis to better study the effect of composition and molecular architecture on the properties of amphiphilic copolymers, given the possibility to prepare well defined structures with almost no limitations in geometry and chemistry.[1]

1.1.1 Applications

Being possible to build macromolecular structures with tailored characteristics of molecular weight, molecular weight distributions, composition, and architecture, it is possible to study systematically the structure–property relationships and ultimately to select the structures more suitable for a desired application. In fact, these designed polymer systems still represent a stimulating challenge from a fundamental point of view. The macromolecular nature of amphiphilic polymers affords a range of architectures, peculiar rheological behaviour, formation of self-assembled structures, length scales, time scales, and levels of interactions much wider than those offered by small amphiphilic molecules. Such diversity poses great challenges in the characterisation and understanding of the solution and surface properties of large amphiphiles.

Amphiphilic polymers have been extensively studied for their self-assembling properties in bulk phase, and even more in solution. In general, a variety of possible micelles and similar structures are possible. These micelles represent a crucial topic when considering applications of these materials in the biological/biomedical world as drug stabilisers and carriers, or in catalysis as nanoreactors. Micellisation and related applications are based on the dependence of the hydrophilicity of some moieties on external parameters (such as temperature, pH, and ionic strength). This can induce the controlled formation and disruption of micelles when the polymeric aggregate experiences some change in such parameters, when introduced in a living system, and in particular conditions.

The most applied polymers are block copolymers (di- and triblocks, mostly), where the hydrophilic moiety is constituted by PEO and the hydrophobic one is PPO, poly(butylene oxide) PBO, or, more rarely, styrene. These kinds of polymeric surfactants have been extensively employed as dispersants and as

emulsion stabilisers and can be found in formulations for detergents, dyestuffs, paints, coatings, agrochemicals, ceramics, printing inks, etc.[1]

One environment-friendly application of amphiphilic polymers in coating is represented by antifouling fouling-release marine coatings.[6] Being this topic of specific interest for this work, a detailed chapter will follow.

Another significant example of application of amphiphilic polymers to significant industrial issue is enhanced oil recovery.[7] Chemical methods for enhanced oil recovery consist of the injection of a displacing fluid in oil reservoirs, in order to mobilise the crude oil adsorbed in the porous rocks. The displacing fluid is generally constituted by a dilute water solution containing an inorganic base, a surfactant, a water-soluble polymer to increase viscosity. The scope of the base is to decrease the interfacial tension between water and oil phases, reacting with the organic acid components of the crude oil, forming a surfactant *in situ*. The use of polymeric surfactants could represent a favourable option because in principle a decrease in interfacial tension and an increase in viscosity are expected to occur at the same time, with a subsequent positive effect on the process.[7,1]

1.1.2 Micellisation and critical micelle concentration (CMC)

The relatively high molecular weight of polymeric surfactants, as opposed to low molecular weight ones, allows a fine-tuning of the micelle properties, together with other molecular parameters like components chemical nature, composition and topology. Micellisation is also affected by temperature, pH, external shear field, and ionic strength.

Examining the case of a diblock copolymer, the CMC, taken as representative for the aggregation as well as the surface activity behaviour, is in most cases clearly dependent on block length and structure. Indeed the change in Gibbs energy for micellisation (ΔG_{mic}) is usually expressed as:[8]

$$\Delta G_{mic} = - RT\ ln(CMC) \qquad \text{Eq. 1}$$

with R being the ideal gas constant and T being the absolute temperature. ΔG_{mic} is in turn a function of the chemical structure as well as block length, with the dependence becoming explicit when making allowance for group contribution theories, often used for the calculation of ΔG_{mic} values[1]. Theoretical treatments of CMC predict that the CMC decreases exponentially with the length of the hydrophobic block. Experimentally, it has been shown that CMC ≈ $exp(-cN)$ where c is a parameter dependent on the Flory–Huggins interaction parameters and N is the length of hydrophobic block. For higher N (>20) the dependence becomes weaker and CMC scales with $exp(-cN^{1/3})$ (Figure 5).[9]

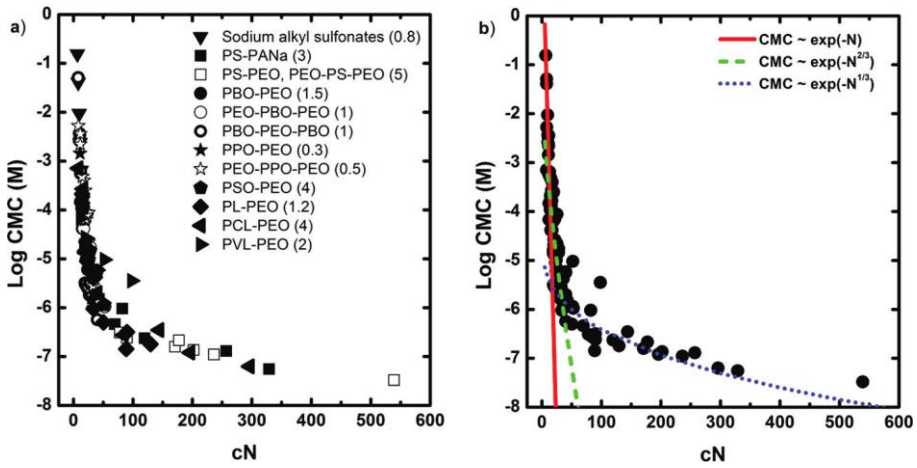

Figure 5: (a) Master plot of CMC as a function of cN for aqueous micelle solutions. Values of c are provided in the legend in parentheses. (b) Comparison of master plot data to different trend lines. Reproduced from ref.[9]

This behaviour seems to be unrelated to the chemical nature of the copolymers, as shown by the data collected for several systems. It is worthwhile remarking how hydrophobic interactions might dominate over both electrostatic repulsion as well as steric hindrance in determining the aggregation behaviour.

Despite this general principle, exceptions are often reported, when more complex than diblock architectures are involved. An amphiphilic polymer, when dissolved in water, causes a decrease in the corresponding surface tension. This is normally attributed to a specific orientation of these copolymers at the surface with hydrophobic block pointing at the air side of the surface. Indeed, for copolymers displaying the same CMC as a function of the average molecular weight or copolymer architecture, it is possible to observe a different surface

activity.[10] Usually a lower solution surface tension is observed for smaller molecular weights (Figure 6).

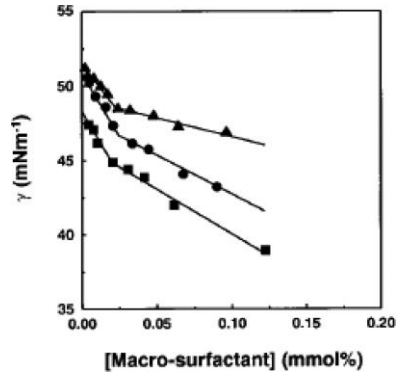

Figure 6: Critical micelle concentrations of PEO-PPO-PEO macro-surfactants determined from the measurement of surface tension: M_n = 1100 g/mol (■); M_n = 2000 g/mol (●); M_n = 2800 g/mol (▲). Reproduced from ref.[10]

In general, an AB diblock copolymer in a selective solvent for the A block will adopt one of three "classical" morphologies: spheres, cylinders, or bilayers, thereby producing spherical micelles, worm-like micelles, and vesicles, respectively. In each case the solvophobic B block will form a single nanoscale domain. Higher interfacial energy between the core block and the solvated corona favours flatter interfaces and larger core domains. The interfacial energy, in turn, depends on factors that include solvent choice, temperature, and pH. On the other hand, a larger corona block, or a more swollen corona block, favours higher interfacial curvature and smaller core dimensions. The stretching of the core blocks can also play a role, especially when the corona blocks are short (the so-called "crew-cut" micelle regime); core block stretching also favours smaller micelles. This competition between interfacial energy and chain conformations produces the universal diblock sequence of spherical micelles → cylindrical micelles → bilayer/vesicles, whether in water and other solvents.[11,12]

If, on the other hand, the copolymer architecture gets more complicated and a second solvophobic component C is included in the system, for example in an ABC block terpolymer, then it is possible to access many more elaborate structures, with subdivided B and C core domains (Figure 7).

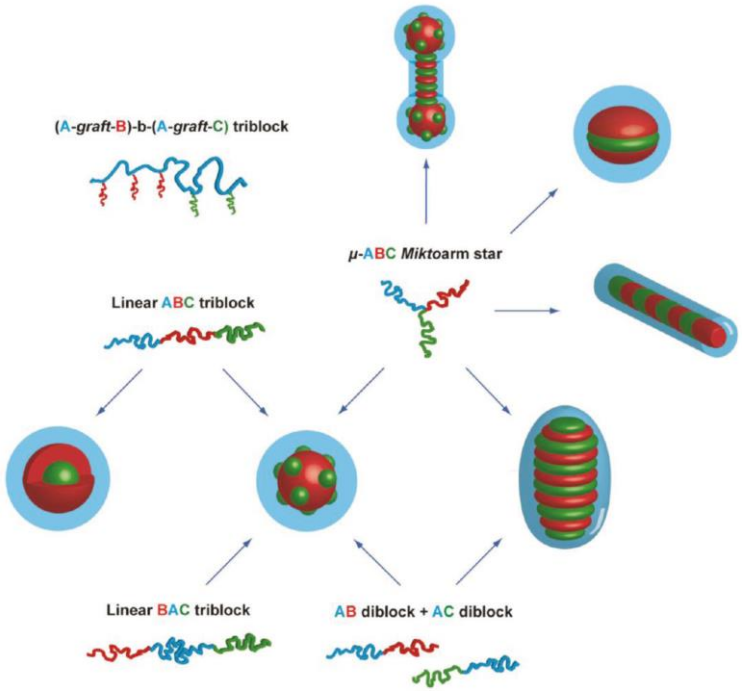

Figure 7: A schematic representation of the five principal strategies adopted for multicompartment micelle production with an illustrative example of the morphology produced. Reproduced from ref.[11]

This directed self-assembly is a powerful strategy that leads to a step-wise structure build-up, for example by changing the external environment (Figure 8).[11] It yields well-defined multicompartment micelles with precisely tunable nanoscale patchiness, with control over the hierarchical assembly up to the microscale, while using simple linear ABC triblock terpolymers.[13] Such multicompartment micelles represent a significant step toward hierarchical self-assembly with multiple functions and designed architectural features on several length scales. As such, they hold great promise for advanced nanotechnological applications.[11]

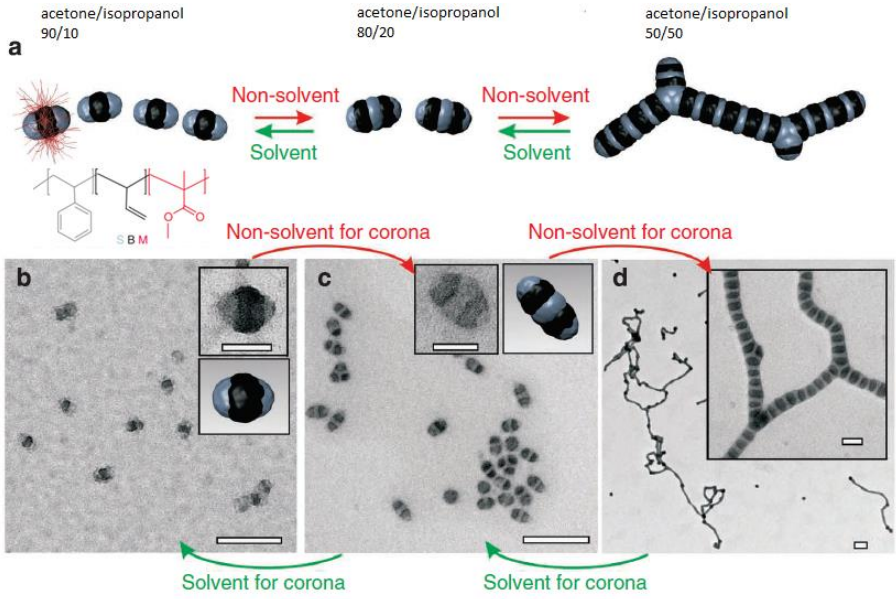

Figure 8: (a) Mesoscale assembly of multicompartment micelles. The red corona chains emerge from the black compartments, but are mostly omitted for clarity. (b-d) TEM images (OsO_4-staining except (b) RuO_4, acetone/isopropanol fractions are given in v/v). Scale bars are 200 nm and 50 nm in insets. Adapted from ref.[13]

1.1.3 Self-assembly of random copolymers

For many years, the field of polymer self-assembly has been dominated by block copolymers. A distinct advantage of block copolymers is that there exists a structure-property correlation that provides the guidelines for the type of assembly that one would anticipate from the type of amphiphilic blocks used and the molecular weights of the blocks. This type of understanding is certainly lacking in random copolymers based self-assembly.

As one example, among self-assembling random copolymers,[14] amphiphilic random copolymers containing hydrophobic dodecyl chain and hydrophilic L-glutamic acid were prepared with different compositions.[15] Under appropriate conditions giant vesicle (artificial cell-like system, useful to mimic living cell lipidic membranes) were obtained, while previously reported giant vesicles are

mainly from the well-defined block copolymer self-assembly (Figure 9). Furthermore, for polymers with a higher hydrophilic content, films with organised nanostructures could be obtained.

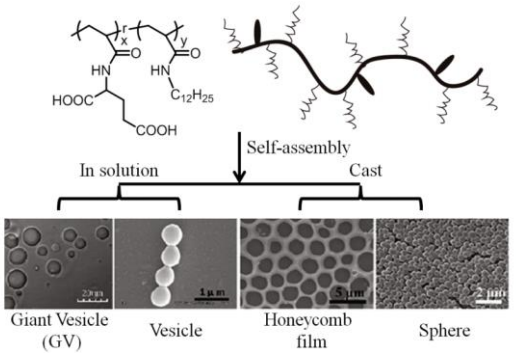

Figure 9: Molecular structures of copolymers and TEM images about the assemblies from these copolymers using different condition. Reproduced from ref.[14]

Compared to block copolymers, preparation of random copolymers is relatively easy, as they are typically achieved in a one-step copolymerisation of two (or more) different monomers. Therefore, it is intriguing to highlight the supramolecular capabilities of random copolymers in self-assembly.

While the self-assembly strategies outlined above are based on the controlled aggregation of several polymer chains, there is also a great interest in the possibility of preparing nanoparticles through the intramolecular crosslinking, folding or collapse of single polymer chains, that is a prerogative of random copolymer instead of block ones.[14]

Many natural polymers are, in fact, amphiphilic, and display structures far from those of block copolymers. The most notable example is represented by proteins. The well-known catalytic perfection of enzymes is mainly due to a delicate balance of hydrophilic and hydrophobic amino acids, that drive the folding of the protein toward the best active and efficient tertiary and quaternary structures. Even though they are generally not considered from this point of view, in many cases proteins are found in natural systems as emulsion stabilisers such as casein in milk. Another class of naturally occurring polymeric surfactants is the one of polysaccharides. Emulsan (a lipopolysaccharide) and chitosan are notable examples.

Considering the arrangement of amino acids in the sequence of a polypeptide that has the ability to form a regular three-dimensional structure, random copolymers are usually used to mimic this unimolecular self-assembly process.

1.1.4 Single-chain folding polymers

Mecerreyes, Hawker, Miller and co-workers in 2001 introduced the concept of single-chain nanoparticle (SCNP) via the intramolecular cross-linking of linear precursor containing pendant acryloyl or methacryloyl functionalities. The particles produced in this way (with controlled hydrodynamic diameter between 4 and 13 nm) were applied to the generation of nanoporous thin films, as sacrificial porogens.[16] Since then, single-chain folding technology has grown significantly and rapidly and features high potential in biomimetic applications, precision catalytic systems and sensor materials.[17,18] Isotropic interactions (that is, random intramolecular self-associations) can be exploited to transform polymer coils into globular entities.[19] Such approaches are sometimes described as 'chain collapse' or 'chain compaction' rather than 'folding'. Furthermore, they allow unimolecular engineering. Taking advantage of intramolecular interactions, the folding of linear polymer chains into architecturally defined single-chain nanoparticles (5-20 nm in diameter) is feasible.[20] While the research on single-chain folding polymers is primarily fundamental in nature, a tailored synthesis and in-depth characterisation of size, shape and core-shell structure and conformation of these materials may drive to exploitation in environmental chemistry, industrial catalysis, biomedicine and drug delivery.

A chronological review of the strategies applied in single-chain folding was recently published by Pomposo and co-workers (Figure 10),[21] accounting separately for the covalent intramolecular crosslinking that leads to permanent nanostructures and the reversible nanostructures obtained via supramolecular and dynamic covalent approaches.

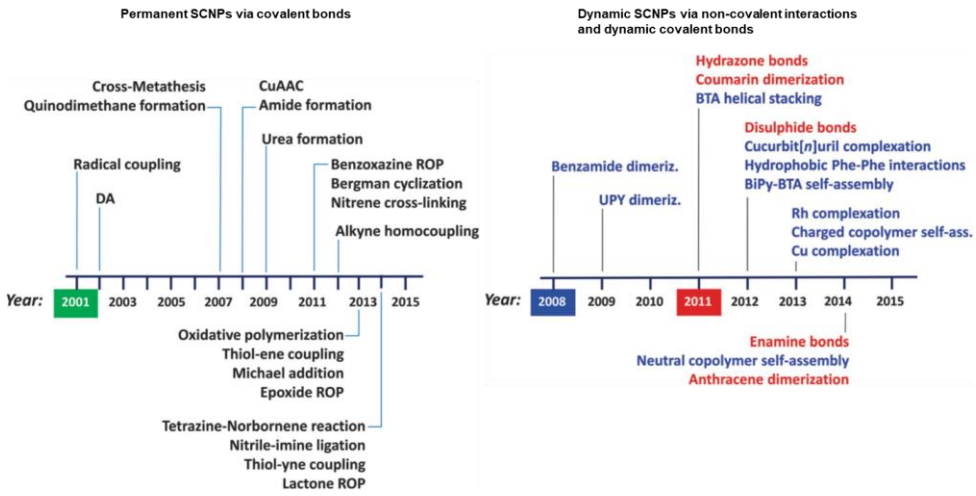

Figure 10: Summary of the advances in single chain technology applied to the construction of permanent SCNPs (black) and structurally dynamic SCNPs synthesised via supramolecular, non-covalent interactions (blue) and dynamic covalent bonds (red). Adapted from ref.[21]

In addition to the originally proposed radical intramolecular crosslinking procedure, the introduction of new and refined strategies to covalently stabilise the unimolecular nanoobjects into soft particles, demonstrated the growing interest in this field. As depicted in Figure 11, in any case, proper functional groups are introduced in polymer precursors during the polymerisation or with polymer post-modification. Then precursor is crosslinked in an additional reactive step. Different chemistries are employed, including Diels–Alder (DA), cross-metathesis, quinodimethane formation, copper(I)-catalysed azide–alkyne cycloaddition (CuAAC), benzoxazine ring opening polymerisation (ROP), Bergman cyclisation, nitrene cross-linking, alkyne homocoupling, oxidative polymerisation, thiol-ene coupling, Michael addition, epoxide ROP, and tetrazine–norbornene reaction, nitrile–imine ligation, thiol-yne coupling, lactone ROP. All these proposed strategies have been extensively reviewed in the literature[17,22–24] and we will not enter into details here due to the moderate interest of covalent intramolecular cross-link, in this dissertation.

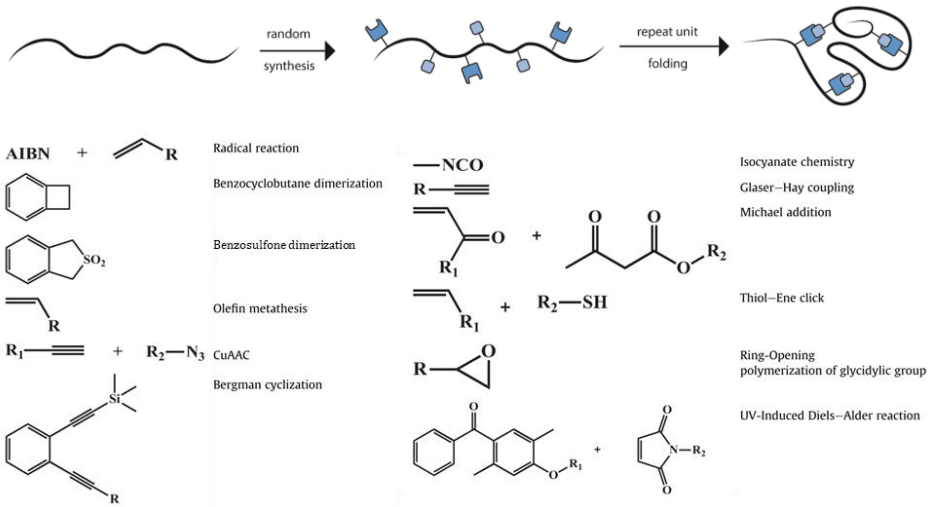

Figure 11: Covalent crosslinking chemistry proposed for the SCPNs fabrication. Adapted from ref.[18,24]

In addition, the developments in the preparation of structurally dynamic or reversible folded polymers via supramolecular interactions and dynamic-covalent bonds is illustrated in Figure 10 (right).

In the completely different realm of structurally dynamic nanostructure, without covalent intramolecular crosslinking, polymer chains undergo reversible folding and maintain a tunable, stimuli responsive character mimicking the self-adaptive, self-replicating and self-healing character of natural smart systems.

Different non-covalent bonding-based strategies have been introduced over recent years to afford the preparation of responsive SCNPs. The first acknowledged report of such reversible folding was in 2008,[25] via benzamide dimerisation through hydrogen bonding (Figure 12).

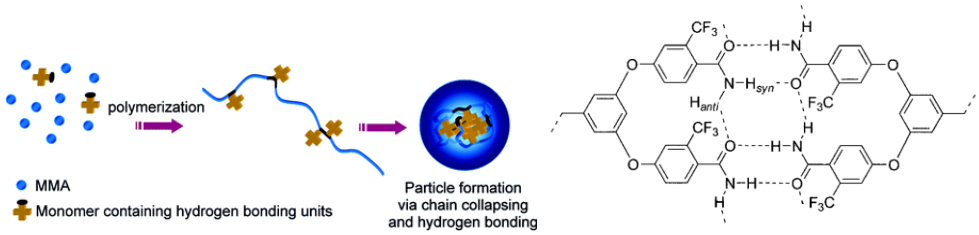

Figure 12: Schematisation of chain collapsing process and illustration of the proposed hydrogen bonding pattern. Adapted from ref.[25]

After that, several supramolecular motifs where used such as ureido-pyrimidinone (UPY) dimerisation,[26] benzene-tricarboxamide (BTA) helical stacking[27], cucurbit(8)uril complexation,[28] hydrophobic L-phenylalanine interactions,[29] metal complexation[30] and charged amphiphilic random copolymer[31] self-assembly. Lately, self-assembly of neutral amphiphilic random copolymers was also shown to create unimolecular particles.

In particular, graft copolymers composed of poly(γ-glutamic acid) and L-phenylalanine (Phe) represent the first study focused on the preparation and characterisation of unimer nanoparticles tuning the hydrophilic−hydrophobic balance of graft copolymers (Figure 13).[29]

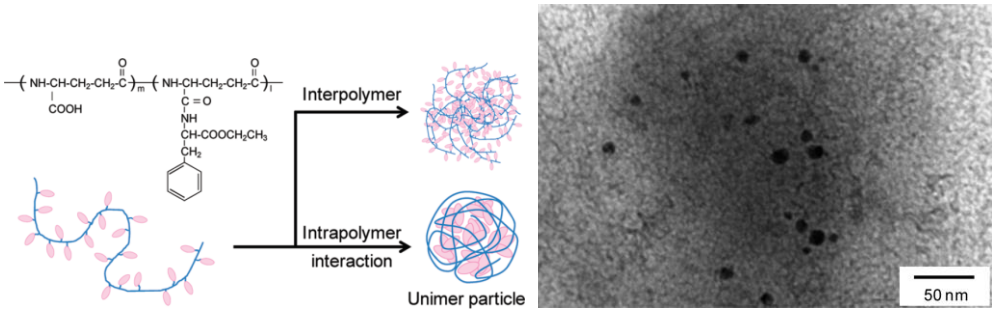

Figure 13: Self-association behaviour of biodegradable graft copolymers composed of poly(γ-glutamic acid) and L-phenylalanine (Phe) γ-PGA-graft-Phe. TEM images of unimer nanoparticles obtained. Adapted from ref.[29]

After that, multi-responsive SCNPs displaying spherical morphology in solution constructed via single chain folding of neutral amphiphilic random copolymers in water have been reported by Sawamoto and colleagues.[32] As depicted in Figure 14, their amphiphilic random methacrylate copolymers, consisting of PEG and alkyl side groups were found to undergo spontaneously reversible

single-chain self-folding in water to SCNPs comprising hydrophobic compartments.

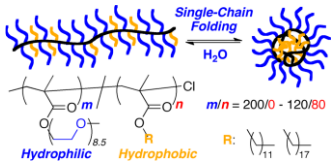

Figure 14: PEGMA/alkylMA amphiphilic random copolymers that display single-chain folding behaviour in water. Reproduced from ref[32].

The self-assembled nanoparticles were dynamic, reversible and stimuli-responsive in water. They were unfolded via the addition of methanol. PEG-based polymers often show lower critical solution temperature (LCST)-type phase separation in water, that in these case is modulated as function of the hydrophobicity of the copolymer.[32] Interestingly, these SCNPs were stable even at a high concentration in water, due to the PEG side-groups acting as efficient steric stabilisers.

Later, Sawamoto and co-workers proposed amphiphilic/fluorous random copolymers as a new class of non-cytotoxic polymeric materials for protein conjugation,[33] that possessed multimodal self-assembly character (Figure 15): large aggregates from the intermolecular multi-chain association and compact unimer micelles from the intramolecular single-chain folding.

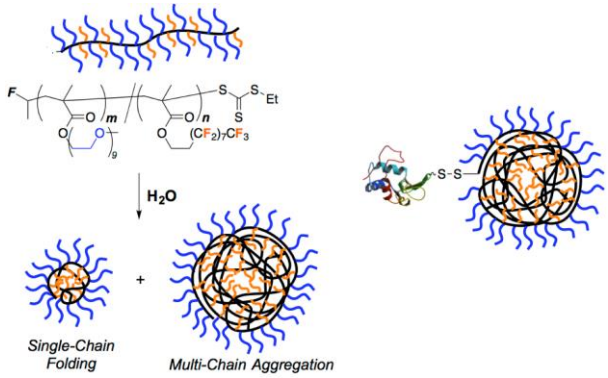

Figure 15: Biocompatible amphiphilic/fluorous random copolymers displaying self-folding and multi-chain association and schematic representation of thiolated lysozyme conjugated onto the large aggregate. Adapted from ref.[33]

Because this field is still in its infancy, only a limited number of proof-of-concept investigations have been carried out to endow single chain soft nanoobjects with useful functions. Despite this limitation, the possibilities offered by these unimolecular nanoentities for a variety of potential applications are stimulating. The main advantages of folded/collapsed single chains over their linear counterparts are foreseeable in nanomedicine, where higher circulation half-lives and reduced degradation profiles are expected for carriers.[21] The application as image contrast agents is also possible,[34] by photochemical design of functional fluorescent SCNPs or intrinsic contrast provided by structural element like perfluorinated moieties in ^{19}F magnetic resonance imaging.[35]

The application of single-chain folded nanoobjects to catalysis is an equally important outcome. For example, learning from the natural enzymes, these SCNPs may be decorated with metalorganic or organic catalytic centres to improve their catalytic efficiency and stereo-selectivity.[27,36] Due to their adaptability, these artificial enzymes may be more intelligent through the regulation of stimuli signals, which may help to exert better control towards the catalytic reactions.[21]

Reduced size and hydrodynamic volume are especially relevant for applications where a reduction in viscosity is required, as rheology-improving agents for the melts of thermoplastics, elastomers, nanocomposites and paints. Amphiphilic single chain nanoobjects offer additional possibilities as emulsifiers and lithography agents, because of their particular self-assembly behaviour.[21]

All the efforts to control the chemistry that governs single-chain technologies pose the question of what advantages single macromolecules have over conventional collective assemblies. Two obvious answers are size reduction and atom economy. The manipulation of single polymer chains makes it possible to work in a size range that is below the length scale of present nanotechnology.[19] The recent ability to manipulate and visualise single atoms at atomic level has given rise to modern bottom-up nanotechnology. The design of ultra-small unimolecular soft nanoobjects endowed with useful, autonomous and smart functions is the expected, long-term valuable output of single chain technology.

1.2 Fluorescent molecular rotors

Among all the fluorescent dyes, molecules that can undergo an intramolecular twisting motion in the fluorescent excited state are commonly named fluorescent molecular rotors (FMRs).[37] These fluorophores are a particular class in a bigger family of luminophores characterised by aggregation induced emission (AIE).[38] Since their discovery, at the beginning of the 2000s AIE fluorophores showed an outstanding impact on energy, optoelectronics, life science and environment practical applications, providing high luminescence in aggregates and solid state, that, in conventional fluorophores, suffer because of aggregation-caused quenching.[38]

In FMR structure three subunits are generally present: an electron donor unit, an electron acceptor unit, and an electron-rich spacer unit to maintain the donor and acceptor units in conjugation, thus facilitating electron movement between this pair (Figure 16 A). Three typical examples,[39] of such structures are also reported in Figure 16: 1,4-dimethylamino benzonitrile (DMABN, B), 9-(dicyanovinyl) julolidine (DCVJ, C), p-(dimethylamino) stilbazolium (p-DASPMI, D). The arrows highlight bonds that provide easy conformational alteration, by intramolecular rotation.

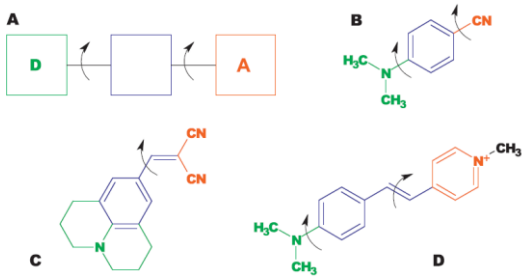

Figure 16: General motif of a molecular rotor (A) and some representative chemical structures (B-D), highlighting the electron donating subunit (green), the electron accepting subunit (orange), and the spacer unit (blue). Reproduced from ref.[39]

Haidekker and Theodorakis also describe in detail the fluorescence behaviour of FMR, referring to their Jabłonski diagram in Figure 17.[39] In the ground state S_0, the three subunits assume a planar or near-planar configuration. Diversely, intramolecular charge transfer from the donor to the acceptor unit occurs, when the molecule is excited by a photon, and electrostatic forces induce an

intramolecular twisting motion of the subunits relative to each other. The molecule enters a twisted intramolecular charge transfer state with a lower excited-state energy, usually named TICT state. At that point, the destiny of the excited molecule depends on the specific chemical structure, and two pathways are generally recognised (Figure 17, A and B). If possible, relaxation from the twisted state is associated with a red-shifted fluorescence emission, as seen for DMABN that exhibits a distinct second emission band, different from the locally excited state (LE) fluorescence. Otherwise, non-fluorescent relaxation takes place to ensure energy dissipation, when the TICT energy gap is much smaller than the LE energy gap, as commonly seen for DCVJ and p-DASPMI.

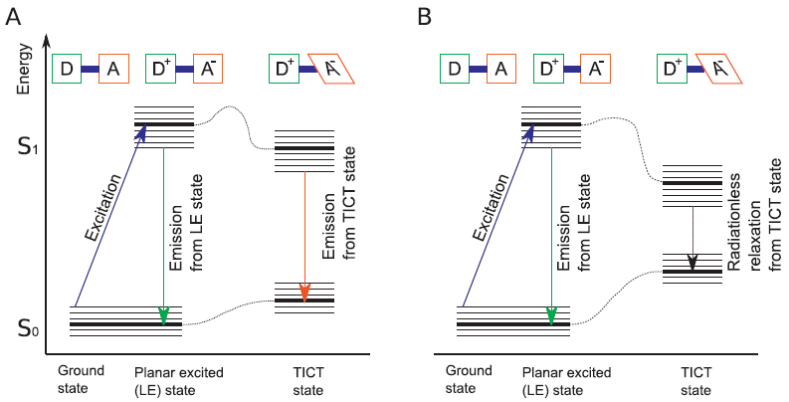

Figure 17: Extended Jabłonski diagram for molecular rotors. Reproduced from ref.[39]

Notably, the twisted state formation rate depends on the local microenvironment. The contribution of local microviscosity is predominant. Higher viscosity favours the radiative decay from the TICT state in FRMs that allow this transition, or it increases the fluorescece quantum yield of the photon emission from LE state, in the case of FMRs that exhibit nonradiative relaxation from the twisted state. In this latter case, LE-state fluorescence quantum yield Φ and bulk viscosity η follow a power-law relationship that is widely referred to as the Förster-Hoffmann equation:

$$\log(\phi) = C + x\log(\eta) \qquad \text{Eq. 2}$$

From this environment sensitivity stems the obvious application of FMRs in evaluation of bulk viscosity of fluids, even in complex conditions, where mechanical viscosity measurement could be inaccessible.[40] Since molecular rotors are affected only by their immediate microenvironment, they can be used

to report spatially resolved microviscosity with resolution limited only by the optical equipment. These two features explain the popularity of molecular rotors in tissue, cell and vesicle imaging and research.[41,42]

In detail, time resolved fluorescence decay of a suitable molecular probe was successfully exploited to characterise relevant features of the self-assembly of an amphiphilic block copolymer in water solution.[43] Poly(N,N-dimethylacrylamide)-block-polystyrene (PDMA-*b*-PS) copolymers form core–corona nanoparticles when water is gradually incorporated into DMF solutions. When micellisation occurs in the presence of the FMR AzeNaph1, a photoluminescence (PL) decay was observed in pure DMF and at different water/DMF solution with varying water content (Figure 18). The green curve in Figure 18 indicates the AzeNaph1 decay profile in bulk PS. At higher water content PL decay is superimposable on that in bulk PS. This demonstrates that the local environment experienced by the probe in micelles is indistinguishable from bulk PS. The rotor, completely insoluble in water, loads in the rigid apolar PS core behaving accordingly. Conversely, the probe decay in pure DMF is very fast. The red curve shows that at intermediate water content the probe decay can be fitted in terms of a biexponential decay having a fast component identical to that measured in DMF and a slow one corresponding to that observed in bulk PS. The probe is in this case partially loaded into the rigid cores of micelles and partially dispersed in solution along with the still disorganised copolymer chains.

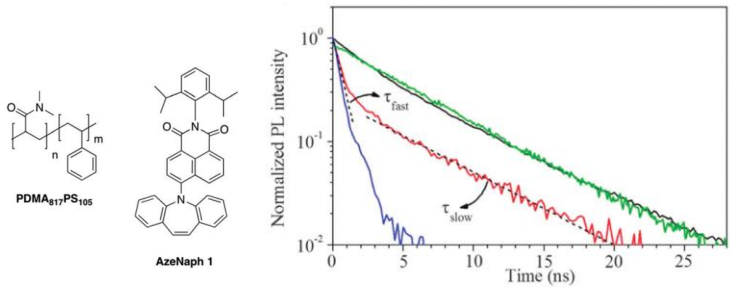

Figure 18: Time decay profile of AzeNaph1 in DMF solution containing the PDMA817-b-PS105 copolymer before addition of water (blue curve) and after addition of 20% v/v (red curve) and 500% v/v (black curve) water. The decay profile of AzeNaph1 dispersed in a polystyrene bulk sample (green curve) is shown as a reference. Adapted from ref[43].

Molecular rotors have been used to investigate protein aggregation and protein conformational changes.[44,45] Another popular application of molecular rotors is real-time *in situ* probing of aggregation[45,43] and polymerisation[46] processes.

Furthermore, FMRs can be utilised as effective dyes for the preparation of smart-polymeric films with vapour sensing characteristics.[47–49] In this case, interactions between a polymer matrix and vapours of a suitable solvent are able to induce a decrease in the local microviscosity, affecting the dye emission. As an example, in Figure 19 is reported the optical response of different cyanovinyljulolidines, triggered by the increased mobility of the PS macromolecular chains with solvent uptake.[47] Appropriate design of the dye largely enhanced the effect for the F8CVJ, that was preferentially distributed at the outer film surface thanks to the surface segregation of the perfluorinated side chain. This example demonstrates how FMR/PS films might be exploited for the realisation of reliable VOC sensing plastic materials.

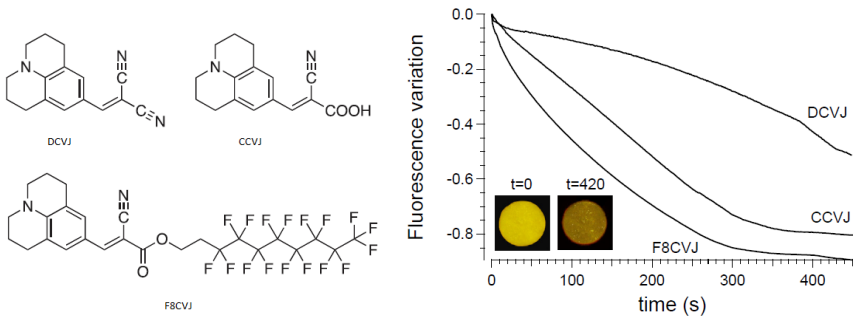

Figure 19: Variation of the fluorescence maximum intensity with exposure time for all 0.05 wt.% FMR/PS films. Inset: images of the 0.05 wt.% F8CVJ/PS film before and after chloroform exposure. Adapted from ref.[47]

1.3 Marine biofouling

Biofouling is a dynamic process, which spans numerous length and time scales, not only related to the marine environment. Every clean surface immersed in water is always subjected to fouling to some extent. In the marine environment

different phases of the process are generally acknowledged, and are schematised in Figure 20.

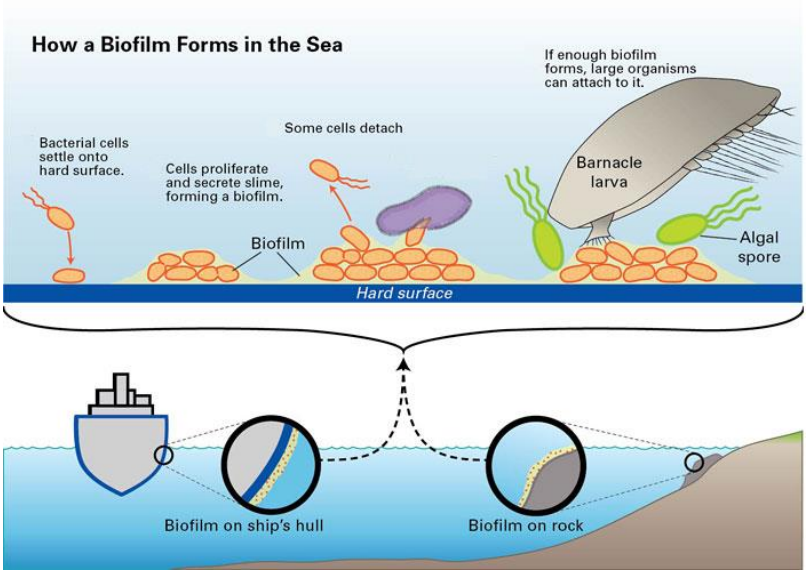

Figure 20: Biofilms form onto a hard surface, creating the platform for the whole fouling process. Adapted from ref.[50]

In a first stage a conditioning film of organic molecules, like proteins and polysaccharides, adsorbs to a pristine surface, within seconds to minutes after immersion. Afterwards, in some hours after immersion, primary colonisation occurs by microorganisms such as bacteria and diatoms, followed by unicellular colonisation by algal spores. A biofilm is defined as the community of attached microorganisms connected by an extracellular polysaccharide (EPS) coating. The EPS coating is both an adhesive and protective layer that modulates the diffusion of molecules in the biofilm, to the bacterial colony, providing, for example, nutrients and resistance to antibiotics. Biofilms could stimulate the settlement of secondary macro-organisms (that colonise the surface in days after immersion) such as larvae of barnacles and tubeworms. On the contrary, avoiding the formation of biofilm is not enough to control the secondary colonisers. Finally, the attachment of multicellular macrofoulants takes place in weeks and month.

Principal marine fouling species, the time-scale and the impact on roughness of their adhesion are outlined in Figure 21.

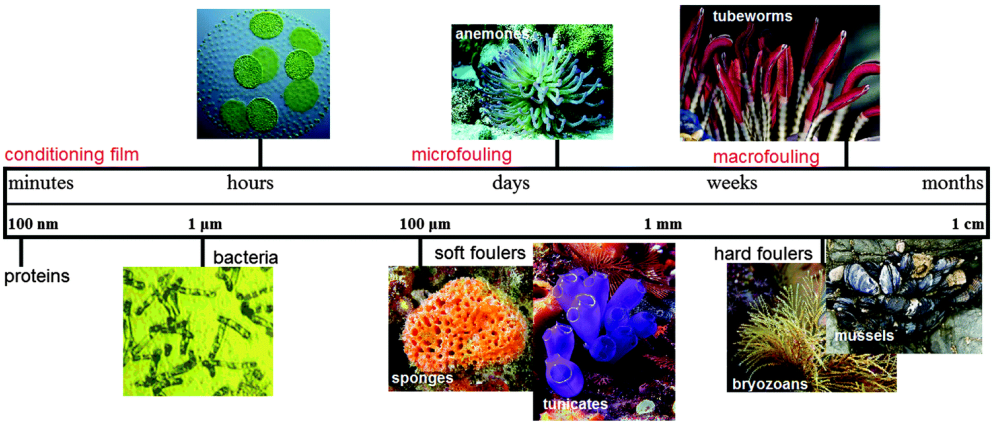

Figure 21: Different phases of marine biofouling: time-line evolution and respective roughness increase. Reproduced from ref.[51]

Fouling settlement has detrimental effects on all industrial equipment and structures employed in contact with water: filtration membranes, turbines, heat exchangers and pipelines, sensors. Biofouling is a major challenge for the biomedical industry as well.[52] Healthcare associated-infections are attributed to biofilms on surfaces such as countertops, doors, beds, surgical tools, or medical devices such as catheters, prothesis, contact lenses, sensors. Moreover, the formation of an atherosclerotic plaque within the arterial wall can be broadly described as a biofouling process itself.[53]

Antifouling (AF) coatings have been developed to prevent the settlement of fouling organisms. The earliest techniques proposed were pitch, tar, wax, heavy metals (lead), or toxic (arsenic-based) coatings. In the mid-1960s, self-polishing AF paints incorporating tributyl tin (TBT-based compounds) were the first to show durable efficiency with a modest cost of production. The restriction on the use of TBT (in 2008) led to a renewed use of paints incorporating high levels of copper and other biocides. However, copper (and zinc) may also pose problems for the aquatic environment.[54] Ships are still slowed today by the growth of algae, barnacles, and slime on their hulls due to the absence of a universal, green, antifouling system. It has been shown that the increased roughness presented by a heavily fouled ship hull can result in powering penalties of up to 86% at cruising speed; even relatively light fouling by diatom 'slimes' can generate a 10–16% penalty.[55] Without effective antifouling measures, in order to maintain

speed, fuel consumption (and therefore greenhouse gas emissions) increase significantly.[56] The United States (US) Naval Sea Systems Command estimates figures based on the present AF coating system, cleaning and fouling level (typically heavy slime) of the Navy. The approximate cost of hull fouling is between $180 and 260 million per annum,[56] only for the US Navy. Moreover, fouled ship hulls can transport invasive alien species in a non-native environment, thus causing problems to the ecosystems.[57]

1.3.1 Toward sustainable antifouling coatings

The current generation of commercial antifouling coatings is normally based on self-polishing copolymer paints (SPC), which contain high levels of copper (40–75 wt%) and booster biocides, such as zinc and copper pyrithione.[58] Due to environmental concerns, biocidal coatings are becoming increasingly more regulated, creating a demand for high performance non-toxic alternatives.[6] The current research on this subject may be divided in two main approaches (Figure 22): biocide-release and non-biocide fouling-release based AF coatings.[51]

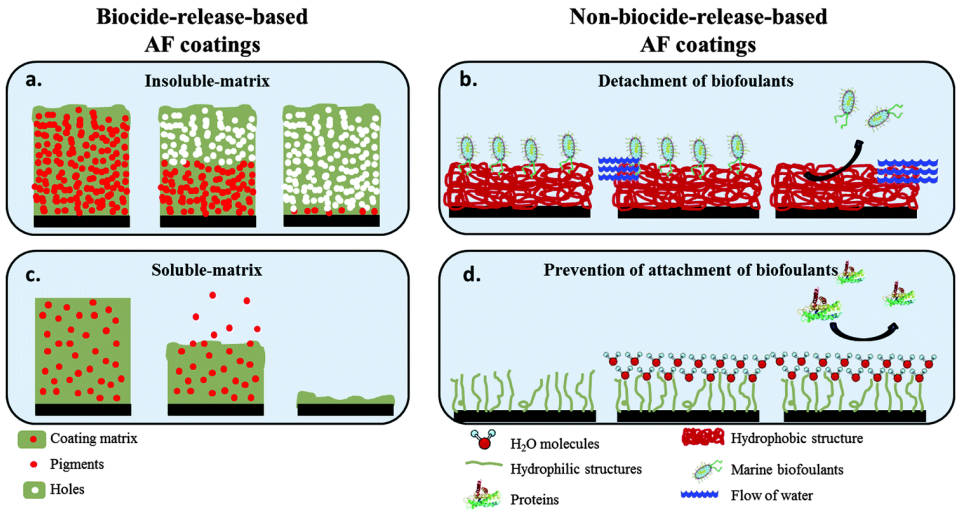

Figure 22: Schematics of marine antifouling coating approaches: (a and c) biocide-release based strategies; (b and d) non-biocide-release based strategies. Reproduced from ref.[51]

Biocide-release based AF coatings apply the same principle as the TBT-based systems, but with less-toxic biocides. These coatings are dispersion of pigments in different types of polymeric binders (soluble or insoluble matrix) which release the pigments into the seawater over time. Insoluble matrix, based on high molecular weight acrylics, vinyls, epoxyes, chlorinated rubber polymers and rosin, are mechanically robust, not susceptible to cracking and generally resistant to atmospheric exposure. After a certain service time, the pigments dispersed in the matrix have to diffuse through such a thick leached layer that the rate of release becomes lower than the minimum value required to prevent fouling.[59]

Controlled depletion polymer (CDP) coatings are soluble matrix paints containing biocides which are mixed with a large proportion of seawater-soluble rosin and synthetic organic resins which are more resistant than rosin derivatives and control the hydration and dissolution of the soluble binder. The key difference between CDP paints and self-polishing paints (SPC) is that the ablative mechanism of the former is hydration and dissolution, not hydrolysis, thus penetration of water deep in the CDP coating results in a fast depletion of biocide, reducing efficacy. SPC coatings are based on acrylic or methacrylic, mainly hydrophobic copolymers, which are easily hydrolysable in seawater. Hydrolysable copolymers blended with biocides confer the ability of controlling/regulating biocides leaching rate through controlling the binder erosion rate. Overall hydrophobicity of the matrix limits the penetration of water and reduces leached layer thickness, maintaining high efficiency over time. Fouling organisms, which attach on the surface of a paint film are eliminated together with the matrix during erosion, resulting in the self-polishing effect.[59]

Non-toxic, fouling-release (FR) coatings approaches should be preferred since they are the greener alternatives, compliant with the current environmental and health regulations. Unfortunately, they suffer of many drawbacks that limit their application, as low efficacy in static conditions. Two working principle are generally proposed for such coatings. First, proper surface design promotes weaker interactions with biofoulants, that can detach simply because of the water flow upon ship navigation. Second, surface chemistry can prevent the attachment of some biofoulants, for example controlling protein adsorption.

The adhesion of marine organisms has been reported to be strongly related to the surface energy of materials. A correlation (Figure 23) between relative adhesion of biofouling organisms and the critical surface tension of the substrate was proposed by Baier.[60] Hence, to design fouling-release coating, one should seek for surfaces within this range of critical surface energy values, typically hydrophobic materials such as fluorocarbons, hydrocarbons and poly(dimethylsiloxane) (PDMS).[6,59]

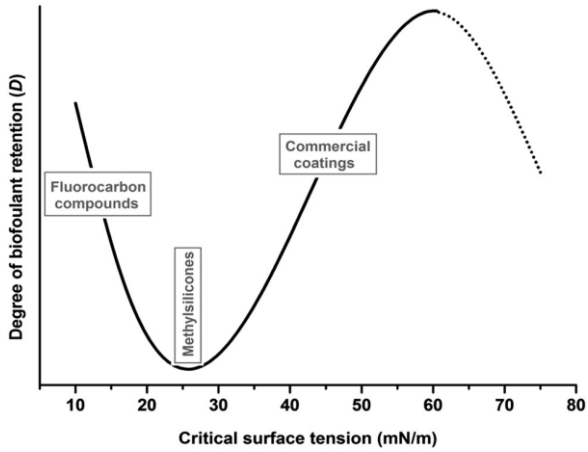

Figure 23: The Baier curve displaying the relative amount of biofouling versus the critical surface tension of various chemical substrates.

The mechanical properties of the coatings should also be considered when targeting weak adhesion facilitating the detachment of biofoulants. This is why PDMS based coatings offer additional advantages. Together with the critical surface energy of the substrates, two properties are important in breaking adhesive joints: the elastic modulus and thickness of the coatings.[61]

For surfaces with much higher critical surface tension, some other AF principle can be explored. PEG polymer brushes and other PEGylated surfaces are a typical example. These surfaces typically have a very strong hydrophilic character and retain a permanent hydration layer. The attachment of biofoulants to the surface is therefore thermodynamically unfavourable as it would require dehydration and confinement of a system which previously had high conformational entropy. This is a common approach in the design of protein resistant surfaces.[62,63]

Biofoulant settlement and colonisation is a natural phenomenon that develops at the interface between specific structural elements of the organism's adhesive and the outermost few nanometres of the substrates. Thus, modifying the properties of a surface at a molecular level, taking advantage of amphiphilic polymer chemistry could be a winning strategy.[6] Intrinsic "ambiguity" of an amphiphilic surface-active polymer can be associated with dynamic responsivity and morphological rearrangement in the aquatic environment. Surface-active polymer in a network could generate hydrophilic and hydrophobic domains, with a critical length scale, proper to inhibit interaction necessary for a colonising organism. The network systems, moreover, with a suitable elastomeric bulk which favourably complements the surface amphiphilicity, would enhance fouling-release property of the entire coating.

The use of amphiphilic polymers in antifouling coatings is a bright example of the use of such polymer platform to help in solving global environmental problems caused by older chemical technologies.

1.4 Reversible-deactivation radical polymerisation (RDRP)

In conventional radical polymerisation (CRP, Scheme 1), three fundamental steps of the process are generally acknowledged:

- chain initiation,
- chain propagation,
- chain termination and, in case, chain transfer.

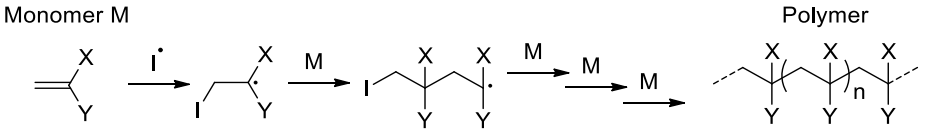

Scheme 1: Radical polymerisation of a vinylic monomer.

The process is a classical chain reaction, usually described kinetically with the assumption of a stationary state with respect to the concentration of radical chain carriers. The lifetime of an individual radical is very short (< 1 s), and

represents the only time frame when chain growth is possible, until a termination event occurs, usually involving the mutual recombination of two chain carriers. This, from a polymer chemist point of view, generally results a distribution of average molecular weights, that is rather broad for polymers synthesised in CRP processes. Another great disadvantage is the impossibility to reinitiate the polymerisation for a terminated chain, limiting the variety of macromolecular architectures accessible with this technique.

Nevertheless, polymers produced by CRP industrial processes represent roughly 40–45% of all industrial polymers, which ranks this method among the most important industrial polymerisation techniques.[64] The dominant position of CRP in industry originates from intrinsic unique characteristics. Thus, in contrast to ionic or coordination polymerisations, CRP is tolerant of protic solvents and trace impurities such as oxygen or monomer stabilizers. Consequently, it can be conducted in polar solvents such as alcohols or, more importantly, water with monomers that are not rigorously dried or purified. For example, the cost to polymerise styrene by anionic polymerisation is about 50% higher than for radical polymerisation.[64] Thus, from an economical point of view, CRP is the technique of choice, in its bulk, solution, suspension and emulsion inflections.

Moreover, that there are other industrially important polymer technologies and applications that are based on radical processes. Unsaturated polyester resins are cross-linked with radical initiators, predominantly peroxides. Photopolymerisation of coatings, printing inks, adhesives, and microelectronic components is a rapidly growing business. Controlled degradation of the molecular weight of polypropylene, and modification of polyolefins by grafting of polar monomers are other examples. Finally, radicals are involved in the thermally and photochemically induced degradation of polymers resulting in the market of stabilisers used to prevent or retard this deterioration.

In the effort of improving conventional radical process, it has been found that the outcome of a polymerisation can be controlled by reversible-deactivation of chain carriers. A 2010 IUPAC recommendation[65] proposes the term reversible-deactivation radical polymerisation (RDRP) for polymerisations previously called controlled radical polymerisation or living radical polymerisation. Since the 1980s, different additives have been studied for this purpose, leading to several specific types of polymerisation widespread nowadays. These include

nitroxide-mediated polymerisation (NMP), reversible addition-fragmentation chain-transfer (RAFT) polymerisation, atom-transfer radical polymerisation (ATRP) and its developments Cu(0)-mediated RDRP.

All reversible-deactivation radical polymerisations display a similar mechanism (Scheme 2). The additives (A) react with propagating species resulting in deactivated (dormant) chains, unable to participate in propagation or terminations (R-M-A). Most of chains are in the deactivated form, and at any given time only a small fraction are active chains capable of chain growth. As long as the interconversion between active and dormant forms is rapid, compared to propagation, all chains grow at the same rate. Meanwhile, chain termination and irreversible chain transfer are disfavoured by the low concentration of active radical species. In this way, the period of chain growth of every chain may be extended indefinitely, allowing even sequential chain extension, as in truly living polymerisation. In addition, if the initiation step is fast enough, all chains grow to similar length and the distribution of molecular weights of the products can be much narrower than in the conventional radical polymerisation.

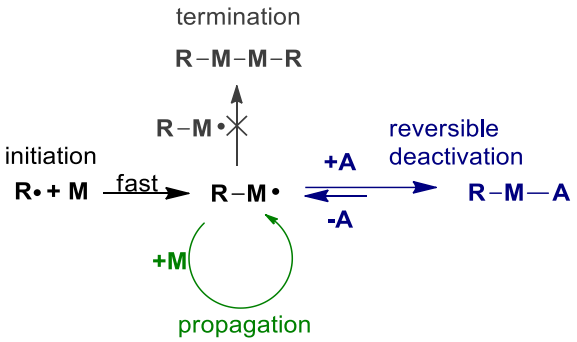

Scheme 2: General reversible-deactivation radical polymerisation mechanism.

RDRP opens completely new possibilities for the design and synthesis of novel materials, as testified by the remarkable number of scientific reports of such polymerisation techniques.[66,67] Very optimistic forecasts of their commercial potential were made. Today, the known industrial applications of RDRP are still few and it is now clear that it will not affect the production of large-volume commodity polymers. However, its potential for the development and production of high-value polymeric specialties remains intact. Possible target

products include adhesives, binders, compatibilisers, cross-linkers, dispersants, emulsifiers, levelling agents, lubricants, sealants, and thermoplastic elastomers. These products are expected to find applications in various industries such as aerospace, aircraft and automobile, biomedical and cosmetic, coatings, electronics, home and personal care, and nanotechnology. Not all RDRP techniques known today are equally well suited for upscaling from small laboratory experiments into large-scale industrial processes. For example, the controlling agent must be cost effective and ecologically sound. Furthermore, residual metals in ATRP or the chemical nature of the end groups in RAFT may be an issue. The attempts to overcome these issues helped maintaining the high interest of the scientific community on the further development of already established polymerisation techniques.

The first industrially applied RDRP was most likely the iodine-transfer polymerisation used by Daikin Industries for the preparation of fluorinated thermoplastic elastomers. Another success was registered by Kaneka, which commercialised the XMAP range of products, moisture and photocurable telechelic polyacrylates prepared by ATRP for use as sealants and adhesives, or in coatings.[68] Matyjaszewski at the Carnegie Mellon University guide CRP Consortium (2001–present) with the goal to assist major industrial companies in this transfer. From the process point of view, a RAFT agent can simply replace the conventional chain transfer agent, requiring little or no change in established industrial setups, provided that RAFT agents must be readily available. For example, are now well-known the trithiocarbonate BlocBuilder® DB, developed by Arkema to commercial stage, and the xanthate Rhodixan® A1 that can be obtained under licence from Rhodia.

1.4.1 Reversible addition-fragmentation chain-transfer (RAFT)

The first reports of the direct use of addition-fragmentation transfer agents to control radical polymerisation appeared in the late 1980s. Only in 1998 Moad, Rizzardo and Thang from CSIRO diffused “a new living free-radical polymerisation of exceptional effectiveness and versatility”.[69] Nowadays, reversible addition-fragmentation chain transfer (RAFT) is one of the most

popular method for conferring living characteristics on radical polymerisations, based on degenerate-transfer radical mechanism, in presence of an adequate chain-transfer agent (Figure 24).

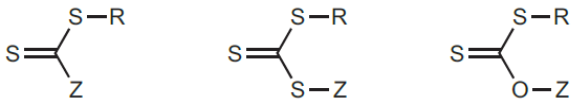

Figure 24: General structures of RAFT chain-transfer agents: thiocarbonylthio, trithiocarbonates and xanthate moiety.

The first step in RAFT polymerisation is the radical initiation step, where a radical is created from a conventional radical source (AIBN, peroxides, photoinitiators) and form oligomers. Then, the oligomeric radicals produced in the initiation step (R' in Scheme 3) react with the RAFT chain-transfer agent before further propagation. This is due to the highly reactive C=S bond of the RAFT agent, which means that radical addition is favoured over the addition to any of the double bonds that are present on the monomer. The radical intermediate can fragment back to the original RAFT agent and an oligomeric radical or fragment to yield an oligomeric RAFT agent and a reinitiating R· radical. The structure of R· should be such that it is a good reinitiating group. Following re-initiation, polymer chains grow by adding monomer, and they rapidly exchange between existing growing radicals (as in the propagation step) and the species capped with a thiocarbonylthio group, maintaining a limited amount of propagating chains. Although limited, termination reactions still occur via combination or disproportionation mechanisms.

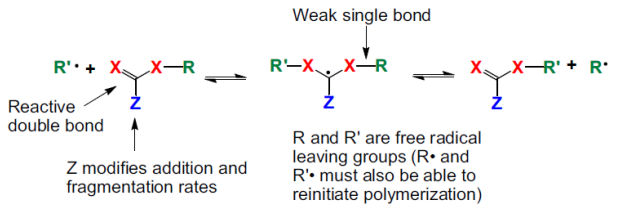

Scheme 3: Main equilibrium in reversible addition-fragmentation chain transfer mechanism.

The structures of the R and Z groups are of critical importance to a successful RAFT polymerisation (Figure 25). The Z group of a RAFT agent is important in

the pre-equilibrium stage of the polymerisation. The R group should be a better leaving group than the propagating radical and must efficiently reinitiate monomer as an expelled radical.

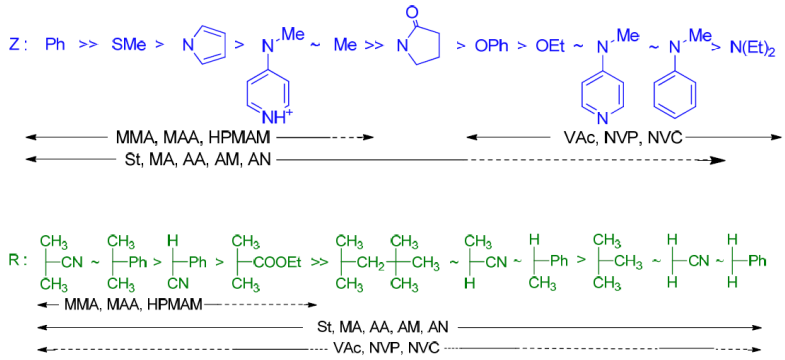

Figure 25: Guidelines for selection of RAFT agents (Z-C(=S)S-R) for various polymerisations. For Z, addition rates and transfer constants decrease and fragmentation rates increase from left to right. For R, fragmentation rates decrease from left to right. A dashed line indicates limited control. Reproduced from ref.[70]

Most of the monomers that are polymerised via conventional free-radical polymerisation can also be prepared using the RAFT methodology, with an adequate chain-transfer agent. This opens the route to a wide range of functionality and makes the RAFT process a technique of choice to produce functional polymeric architectures. Dithioester and trithiocarbonate RAFT agents are appropriate for the polymerisation of more activated monomers such as methyl methacrylate (MMA), methacrylic acid (MAA), hydroxypropyl methacrylamide (HPMAM), methyl acrylate (MA), acrylic acid (AA), acrylamide (AM), acrylonitrile (AN) and styrene (St). Xanthates and dialkyl dithiocarbamates are suited to the polymerisation of less activated monomers such as vinyl acetate (VAc), N-vinylpyrrolidone (NVP) and N-vinylcarbazole (NVC).[70]

1.4.2 Atom transfer radical polymerisation (ATRP)

One of the most popular techniques that has emerged in the RDRP panorama is the transition metal mediated living radical polymerisation which was introduced almost simultaneously but independently by Sawamoto[71] and Matyjaszewski[72,73] in the 1990s. Among other transition metals, both ruthenium and copper have been successfully utilised as the catalyst source, although copper remains, to date, the most studied transition metal, mainly due to its large availability, low cost, and ease of handling. When copper, rather than ruthenium, is utilised, the process is typically termed ATRP. Radical generation usually involves an alkyl halide undergoing a reversible redox process catalysed by a transition metal complex such as a copper halide (Figure 26).

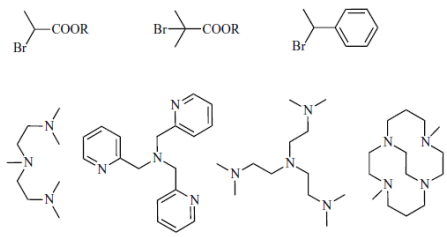

Figure 26: Common halides (secondary α-bromoester, tertiary α-bromoester and benzylic halide) and ligands (N,N,N′,N′′,N′′-pentamethyldiethylenetriamine, tris(2-pyridylmethyl)amine, tris(2-dimethylaminoethyl)amine, bridged cyclam) for ATRP.

The general order of Cu complex activity in ATRP for ligands is tetradentate (cyclic-bridged) > tetradentate (branched) > tetradentate (cyclic) > tridentate > tetradentate (linear) > bidentate ligands. The nature of nitrogen atoms in ligands also plays a role in the activity of the Cu complexes and follows the order pyridine ≈ aliphatic amine > imine < aromatic amines. It is important to select a sufficiently reactive species for an efficient ATRP initiation for the selected monomer. Reactivity of alkyl halides follows the order of tertiary > secondary > primary, in agreement with bond dissociation energy needed for homolytic bond cleavage. Also, radical stabilisation is enhanced by the presence of an α-cyano group which is more activating than either an α-phenyl or ester group. The most active initiator is ethyl α-bromophenylacetate, with combined

activation effect of both benzyl and ester species, which is >10 000 times more active than 1-phenylethyl bromide, and >100 000 times more active than methyl 2-bromopropionate. Moreover, alkyl halide reactivities follow the order I > Br > Cl.[74]

ATRP regulation of chain reaction is determined by an equilibrium between propagating radicals and dormant species, predominately in the form of initiating alkyl halides/macromolecular species (P_n-X) (Scheme 4).

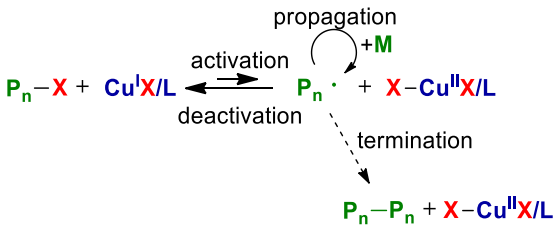

Scheme 4: Atom transfer radical polymerisation mechanism.

The deactivated species periodically react with transition metal complexes in their lower oxidation state, to intermittently form growing radicals (P_n·) and deactivator–transition metal complexes in their higher oxidation state, coordinated by an additional, abstracted halide ligand. Irreversible radical termination always occurs to some extent. However, in ATRP the small amount of bimolecular termination present at the initial stage of the reaction is beneficial for the polymerisation as it provides further control over the molecular weight distributions. This phenomenon is known as the persistent radical effect (PRE). Thus, propagating radicals may be irreversibly terminated via bimolecular termination, resulting in a slight excess of deactivating species in the system which will provide more control over the radical propagation, by shifting the equilibrium toward the dormant species.

As in many fields, polymer synthesis has seen a substantial drive toward environmentally friendly synthesis, resulting in the development of so-called "green chemistry" techniques. Of particular relevance in ATRP, there has been a conscious effort to reduce the catalyst loading to parts per million levels, which led to the development of activator (re)generated by electron transfer ATRP (A(R)GET-ATRP) and initiators for continuous activator regeneration ATRP (ICAR-ATRP). In A(R)GET-ATRP a reducing agent is utilised to (re)generate the active catalyst from the deactivating species that accumulate via unavoidable

termination reactions. A wide range of reducing agents have already been successfully employed, including tin(II) 2-ethylhexanoate (Sn(EH)2), glucose, ascorbic acid, phenol, hydrazine, phenylhydrazine, and nitrogen containing ligands and monomers.[67] In a similar vein to A(R)GET-ATRP, ICAR-ATRP could also be considered as a "reverse" ATRP where a source of organic free radicals (usually AIBN) is typically employed to continuously regenerate the $Cu^{I}Br$ activator which would otherwise be consumed via termination reactions, particularly when the metal is used at very low concentrations. Both A(R)GET and ICAR-ATRP can provide access to well defined polymers while the low concentration of metal reduces the need for extensive purification, at least for some applications. Nevertheless, both A(R)GET-ATRP and ICAR-ATRP do have a number of limitations, such as relatively long reaction times (typically 24–48 h), moderate conversions (typically 10–80%), and the need to purify the macroinitiators prior to block copolymerisation. Nevertheless, the development of versatile and rapid polymerisation techniques with low catalyst loading, high end-group fidelity, even at quantitative conversions, would be a further significant breakthrough.

1.4.3 Cu(0)-mediated RDRP

The use of zero-valent metal in ATRP is known since shortly after the origin of ATRP itself.[75] Cu(0)-mediated RDRP is also known as single electron transfer living radical polymerisation (SET-LRP) mainly due to the contribution of Percec[76] and Haddleton's subsequent innovation with respect to aqueous systems,[77] or supplemental activator and reducing agent ATRP (SARA-ATRP)[67] from the Matyjaszewski's perspective. Cu(0)-mediated RDRP is nowadays an independent, popular topic,[78] that has attracted considerable interest due to its relative simplicity, mild conditions, tolerance to air, simple catalyst removal and reuse.

A fervent debate is alive in the literature regarding the actual mechanism of Cu(0)-mediated polymerisation, and the major catalytic species involved. The two proposed models (Figure 27) of SET-LRP and SARA-ATRP acknowledge the presence of the exact same components, but the contribution of every reaction is different on the overall controlled and rapid polymerisation.

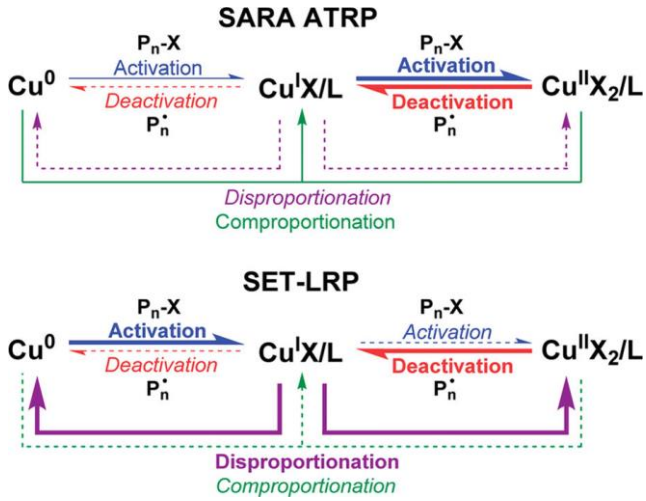

Figure 27: Proposed Mechanisms of SET ATRP (bottom) and SARA ATRP (above). Dotted lines indicate the slowest reactions that can be kinetically neglected.

SET-LRP mechanism suggests that Cu(0) acts as the major activator of alkyl halides and that no major activation occurs by $Cu^{I}Br$ complexes due to their rapid and instantaneous disproportionation in the presence of polar solvents and N-containing ligands that preferentially stabilise $Cu^{II}Br2$ rather than $Cu^{I}Br$. From the SARA-ATRP point of view, $Cu^{I}Br$ is the major activator, like in conventional ATRP, and Cu(0) plays the role of reducing agent as it is able to regenerate $Cu^{I}Br$ through comproportionation, maintaining the catalytic activity of $Cu^{I}Br$ during the polymerisation. In both cases, $Cu^{II}Br_2$ keeps the key role of main deactivator.

Regardless of the mechanism, Cu(0)-mediated RDRP can undoubtedly be considered a versatile technique that can be used to create well-controlled polymers with complex architectures.

1.4.4 Polymerisation induced self-assembly (PISA)

Polymerisation-induced self-assembly (PISA) attracted a considerable attention in recent years, being a convenient alternative route to produce block copolymer nanoobjects.[79,80] The process is schematically drawn in Figure 28.

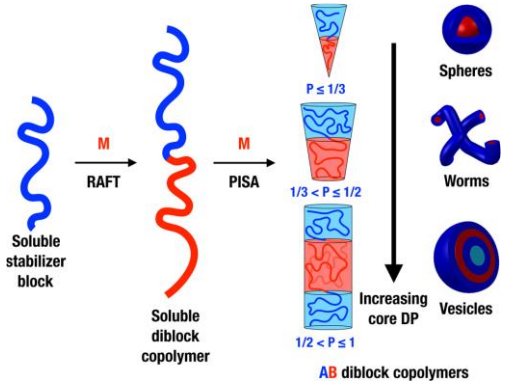

Figure 28: Schematic of the synthesis of diblock copolymer nanoobjects via polymerisation-induced self-assembly (PISA) from ref.[79]

Actually, conventional block copolymers nanostructures are generally achieved in at least two steps: first, initial dissolution of preformed amphiphilic copolymer, then reduction of the solvency for one of the blocks to obtain microphase separation. Differently in PISA process a soluble homopolymer (A) is prepared via solution polymerisation, with a living character that allows subsequent chain-extension with a second insoluble block (B) via either dispersion or aqueous emulsion polymerisation (depending on the monomer solubility in the continuous phase). The AB copolymer gradually becomes insoluble, which drives *in situ* self-assembly to form nanoobjects. By varying the relative volume fractions of the two blocks, either spheres or higher order morphologies (e.g., worms or vesicles) can be obtained, as well as fancy structures as shown in Figure 29 (lamellae, framboidal vesicles, spaced concentric vesicles and yolk/shell particles).[79] This wide range of well-defined morphologies illustrates the versatility and remarkable control afforded by PISA. However, the construction of phase diagrams is crucial for the reproducible targeting of desired morphologies and represents one major objective in this young field.

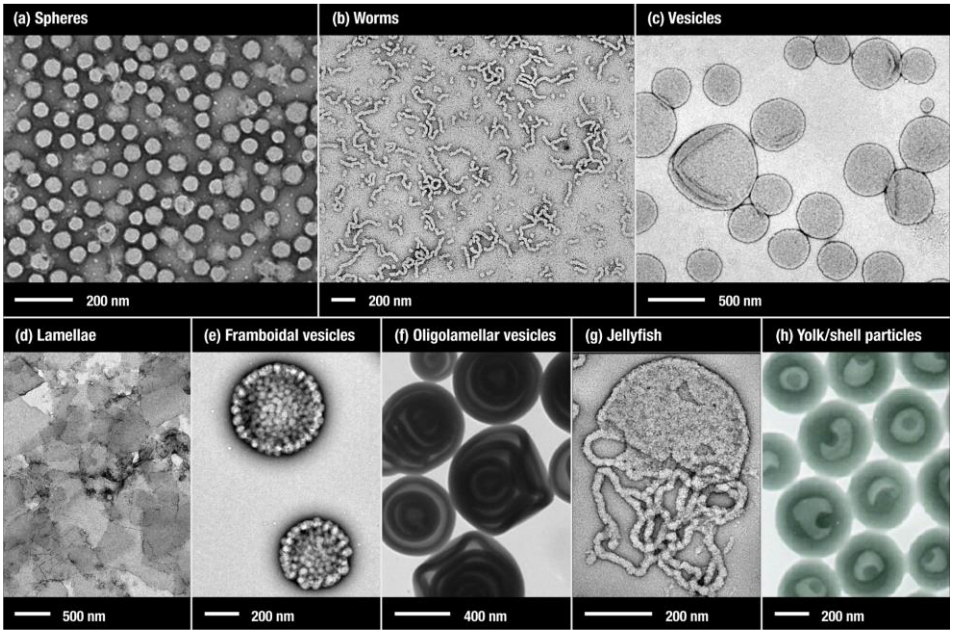

Figure 29: Representative transmission electron microscopy (TEM) images for various morphologies that can be produced using RAFT-mediated PISA. Reproduced from ref.[79]

In principle, PISA syntheses can be conducted using any type of RDRP but in practice, most of literature reports are based on RAFT polymerisation.[79] The development of ATRP techniques[81,82] and in particular its Cu(0)-mediated[83] derivation, thanks to its compatibility with aqueous systems, were fundamental in extending the PISA field to metal-mediated polymerisations. Nitroxide mediated polymerisation was equally explored.[84,85]

Despite the majority of PISA formulation, designed for aqueous environment, a wide range of monomers have been utilised for both the stabiliser and core-forming blocks to produce diblock copolymer nanoparticles in organic solvent either polar or non-polar (including supercritical CO_2 and ionic liquids) via RAFT dispersion polymerisation.[86]

To conclude, the advantages of particle preparation by PISA compared to conventional amphiphilic copolymer synthesis include the ability to conduct polymerisations at higher concentrations (25–50% w/w solid content), with a one-pot process, and the elimination of a separate post-polymerisation purification and preparation step for self-assembly. Both advantages result in a more efficient process with reduced solvent consumption.

2 UNIMER MICELLES OF AMPHIPHILIC RANDOM COPOLYMERS BY SINGLE-CHAIN FOLDING

In this chapter are reported the design and synthesis of amphiphilic copolymers and the study of their properties and self-assembly in solution, in bulk and at the surface of thin films. Most of the monomers and intermediates are commercially available. Polyethylene glycol methyl ether methacrylate (PEGMA M_n = 300 g/mol) was carefully selected as a hydrophilic, thermoresponsive component. Different comonomer species were selected: two strongly hydrophobic/lipophobic perfluorohexylethyl (meth)acrylate monomers (FA and MAF) and a hydrophobic polydimethylsiloxane monomethacryloxypropyl terminated (SiMA M_n = 680 g/mol). Moreover, a fluorescent probe was covalently introduced into copolymers following different strategies, to study the self-assembly through fluorescence emission spectroscopy.

The major objective of this part of the work was to obtain nanomaterials via the single-chain folding of an amphiphilic macromolecule, promoted by intramolecular interactions. In particular, solvophobic interactions, between segments randomly distributed along a single copolymer chain, can lead to the formation of unimer micelles (Figure 30) in a selective solvent, typically water.

These entities differ from the amorphous random coil state, and are characterised by hydrophobic segregated compartments and a more compact conformation.

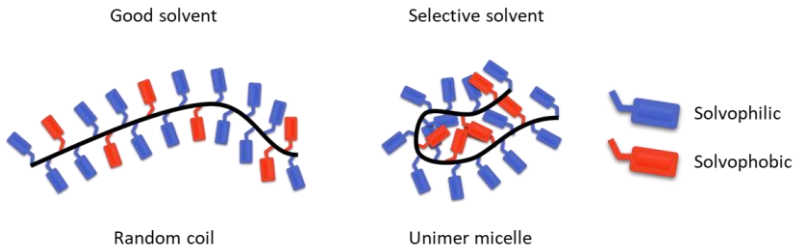

Figure 30: Schematic representation of the unimer micelle concept.

This idea is inspired by the extremely precise folding process typical of natural polymers. These, from a given primary structure, can convey complex functions, strictly related to their secondary and tertiary structures. Synthetic polymer self-assembly is still far from nature perfection. Nevertheless, a tailored synthesis and in-depth characterisation of size, shape, core-shell structure and conformation of these materials might drive to their future exploitation in environmental chemistry, industrial catalysis, biomedicine and drug delivery.

2.1 Results and discussion

2.1.1 Polymer synthesis

2.1.1.1 PEGMAx-*co*-FAy random copolymers

A series of amphiphilic random copolymers from hydrophilic poly(ethylene glycol) methyl ether methacrylate (PEGMA) and hydrophobic/lipophobic perfluorohexylethyl acrylate (FA) was synthesised via atom transfer radical polymerisation, maintaining the same monomer:initiator ratio and changing the PEGMA:FA molar ratio in the feed in a wide range. The resulting copolymers were named PEGMAx-*co*-FAy, where x and y are the mole percentage contents of the respective repeating units.

The synthesis of PEGMA77-*co*-FA23 will be discussed in detail (Scheme 5), as a representative example for the whole series.

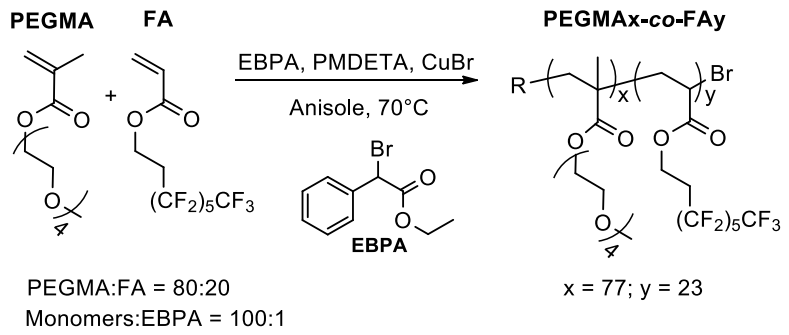

Scheme 5: Synthesis of amphiphilic/fluorous random copolymers via ATRP.

The copolymerisation was carried out at 70°C using EBPA as initiator, CuBr as catalyst, PMDETA as ligand (1:1:1 molar ratios) and anisole (0.5 ml/g of monomers) as solvent.

In order to assess the effective control on the polymerisation, we monitored the kinetics of PEGMAx-*co*-FAy copolymer formation by ^{1}H NMR and SEC chromatography. Figure 31 (left) illustrates the kinetic plot of $\ln([M]_0/[M])$ versus time for PEGMA and FA separately, evaluated from the disappearance of vinyl protons (5.6 and 6.1 ppm for PEGMA; 5.9, 6.25 and 6.4 for FA) in ^{1}H NMR spectra. The plot has a linear trend up 75% of total conversions, indicating that the polymerisation proceeded with a first order kinetics. Then, a deviation from linearity was observed, denoting the appearance of termination reactions. Chain transfer reaction to ethylene glycol side chains was also possible.[87,88] It is reported to be responsible for broadening in molecular weight distribution and gelation of the products, when the polymerisation is not efficiently controlled.

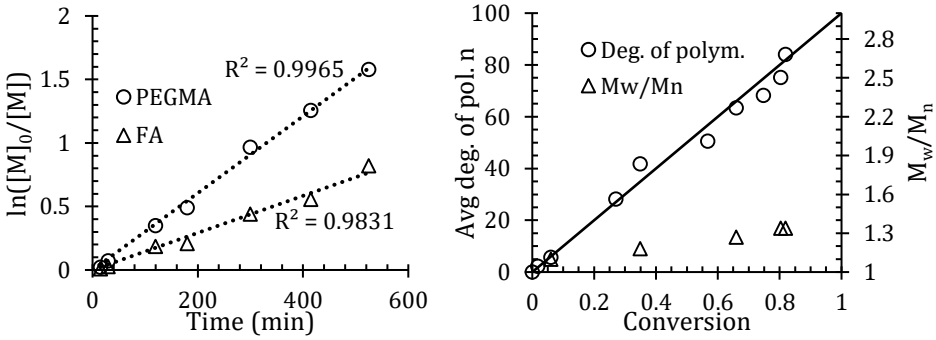

Figure 31: Kinetics plot (left) and degree of polymerisation and dispersity M_w/M_n from SEC analysis vs conversion (right) for PEGMA and FA copolymerisation.

Nevertheless, up to 82% conversion when the reaction was stopped, the number average degrees of polymerisation (n) were consistent with the theoretical values of an ATRP (Figure 31, right) calculated as:

$$n = \frac{[M]_0}{[I]_0} p \qquad \text{Eq. 3}$$

where p is the monomer conversion and $[M]_0$ and $[I]_0$ are the initial molar concentrations of both monomers and initiator, respectively. Number average degrees of polymerisation (n) were calculated from ^{1}H NMR; dispersity M_w/M_n was obtained from SEC traces (Figure 32). The values of the M_n evaluated by SEC were generally lower than those obtained by NMR. This is due to the large difference in the hydrodynamic volumes of the fluorinated copolymers and the polymer standards used for calibration.

The FA homopolymer pFA was synthesised in similar conditions, with EBIB ATRP initiator and trifluorotoluene as solvent instead of anisole.

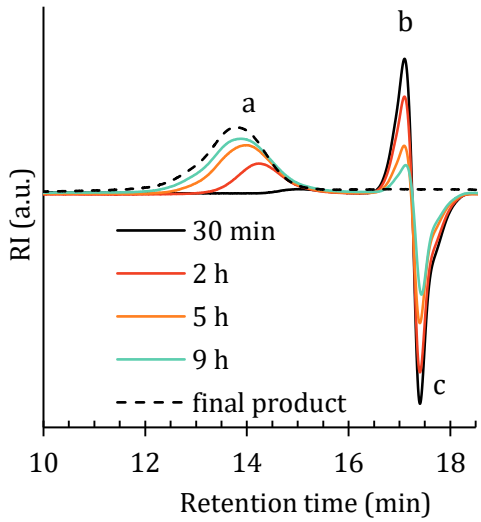

Figure 32: Evolution of SEC traces during the copolymerisation. Peak assignment: a = copolymer, b = PEGMA, c= FA.

An amphiphilic terpolymer containing PEGMA, FA and 2-cyano-2-[4-vinyl(1,1'-biphenyl)-4'-yl]vinyljulolidine (JCBF) was synthesised in the same conditions of the PEGMAx-*co*-FAy series (Scheme 6) and it was named PEGMAx-*co*-FAy-*co*-JCBFz, where x,y,z are the mole percentage content of the respective repeating

units. JCBF is a polymerisable fluorophore of the class of fluorescent molecular rotors.[49] Its fluorescence emission is strongly dependent on the local environment, especially in strong confinement conditions. Thus, it was covalently bonded to the copolymer to monitor the self-assembly behaviour in solutions via fluorescence emission spectroscopy.

The copolymers characteristics are summarised in Table 1. The chemical composition of the copolymers was evaluated from the integrated area of the ^{1}H NMR characteristic signals (4.4 ppm for $COOCH_2$ of the two repeating units, 3.3 ppm OCH_3 for PEGMA and 2.5 ppm CH_2CF_2 for FA). Aromatic protons in the initiator EBPA (7.2–7.4 ppm in acetone-d_6), when present, allowed the evaluation of the number average degree of polymerisation. ^{19}F NMR spectra of the purified copolymers confirmed the inclusion of fluorinated units in the copolymer. JCBF content was determined from UV absorption spectra of copolymer solutions in chloroform, with a calibration curve obtained from $5{\cdot}10^{-7}$–$5{\cdot}10^{-5}$ M chloroform solutions of the fluorescent monomer JCBF. The molar extinction coefficient variation from monomer to polymer was assumed to be negligible.

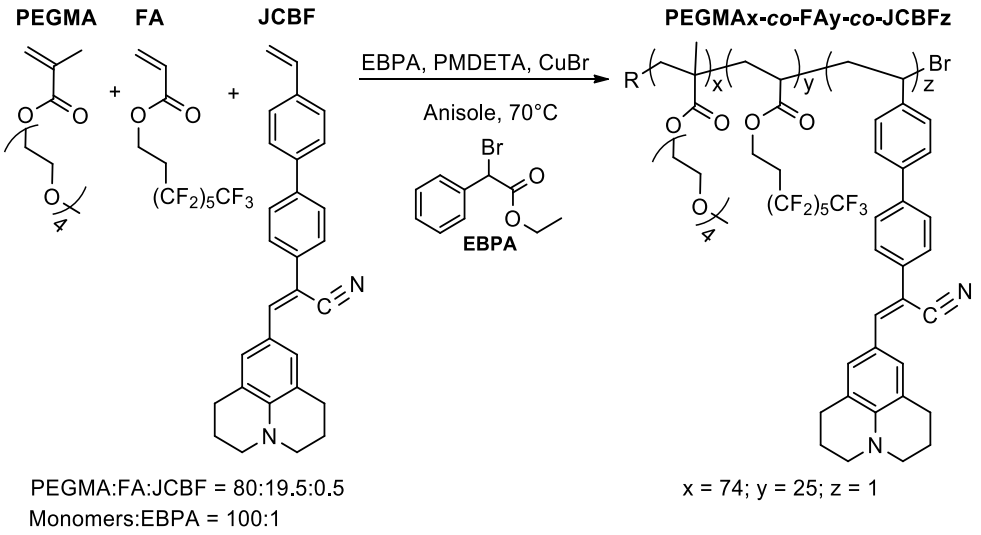

Scheme 6: Synthesis of amphiphilic/fluorous fluorescent random terpolymer via ATRP.

Table 1: Physical-chemical properties of amphiphilic/fluorous random copolymers.

Polymer	M_n[a] (g/mol)	M_n[b] (g/mol)	M_w/M_n[b]	*PEGMA*[c] (%mol)	*JCBF*[d] (%mol)
PEGMA90-co-FA10	--	33000	1.89	90	--
PEGMA77-co-FA23	34000	13700	1.35	77	--
PEGMA69-co-FA31	--	29000	1.43	69	--
PEGMA29-co-FA71	--	16000	1.23	29	--
pFA		7200	1.04	--	--
PEGMA74-co-FA25-co-JCBF1	19700	6900	1.25	74	1

a Number average molecular weight, by ^{1}H NMR, determined in copolymers containing the EBPA initiator.
b Number average molecular weight and dispersity by SEC with $CHCl_3$.
c Molar percentage in the copolymer.
d Molar percentage in the copolymer, determined by UV.

2.1.1.2 PEGMAx-*b*-FA/MAFy block copolymers

One of the great advantages of reversible-deactivation radical polymerisations is the possibility to easily achieve block copolymer architecture, in two reactive steps: homopolymerisation of a given monomer, then subsequent chain extension with a second monomer. Different routes were explored to obtain amphiphilic fluorinated block copolymers, to be compared with amphiphilic random copolymers. First, the synthesis of the hydrophilic macroinitiators pPEGMAa-i was studied. Then, chain extension with hydrophobic/lipophobic perfluorinated (meth)acrylates was accomplished, to provide the amphiphilic character.

PEGMA monomer was selected for the synthesis of macroinitiators. First, atom transfer radical polymerisation (ATRP) was used, and, carefully optimising the reaction conditions, active macroinitiators with different polymerisation degrees were successfully obtained. In any case, EBPA:PMDETA:CuBr catalytic system (1:1:1 in molar ratio) in anisole was used (Scheme 7). EBPA initiator was selected due to the inherent advantage of an easy determination of polymerisation degrees by ^{1}H NMR, exploiting the signal of aromatic protons at 7.2-7.4 ppm. Monomer/initiator ratio, monomer concentration and temperature were varied.

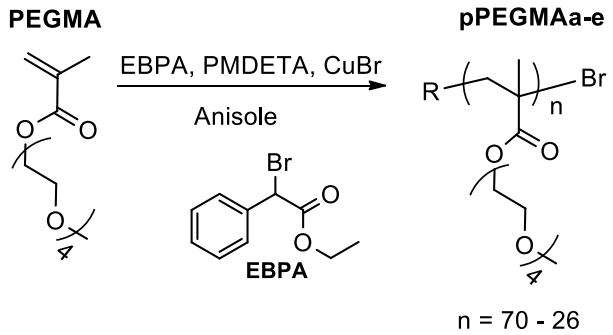

Scheme 7: ATRP synthesis of pPEGMAa-e macroinitiators.

In Table 2 were summarised some relevant reaction conditions from selected polymerisation attempts (named pPEGMAa-e), and physical-chemical characterisation of their final purified products. Polymerisation kinetics was followed by ^{1}H NMR and SEC. As an example, kinetic plot and average degree of polymerisation vs conversion plot were reported in Figure 33, along with SEC analysis of sampled reaction mixture.

Table 2: Reaction conditions for the ATRP of PEGMA, and physical-chemical characterisation of the product pPEGMAa-e.

	pPEGMAa	***pPEGMAb***	***pPEGMAc***	***pPEGMAd***	***pPEGMAe***
[PEGMA] (g/ml)	0.5	0.5	0.5	1.5	1.5
M/I[a]	50	60	60	80	80
T (°C)	80	70	70	70	70
Time (min)	240	180	30	30	180
Final conv.[b] *(%)*	95	95	60	nd[d]	nd[d]
Degree of pol.[b]	58	56	35	26	70
M_n *NMR*[b]	17400	16800	10500	7800	21000
M_n *SEC*[c]	6800	7700	6700	5600	5100
M_w/M_n[c]	1.37	1.45	1.26	1.13	1.17

a Monomer/initiator molar ratio
b Conversion, degree of polymerisation and number average molecular weight, by ^{1}H NMR in acetone-d_6.
c Number average molecular weight and dispersity by SEC with $CHCl_3$.
d Not determined.

PEGMA homopolymerisation proceeded fast, with almost complete conversion (≈ 95%) after 3 hours at 70°C, suggesting no need to further increase the reaction temperature, as in pPEGMAa attempt. Unfortunately, high dispersity values (entry pPEGMAa and pPEGMAb in Table 2), demonstrated poor control over transfer and termination reactions, at high conversion. Stopping the reaction at lower conversion allowed a reduction of dispersity (1.26 for pPEGMAc).

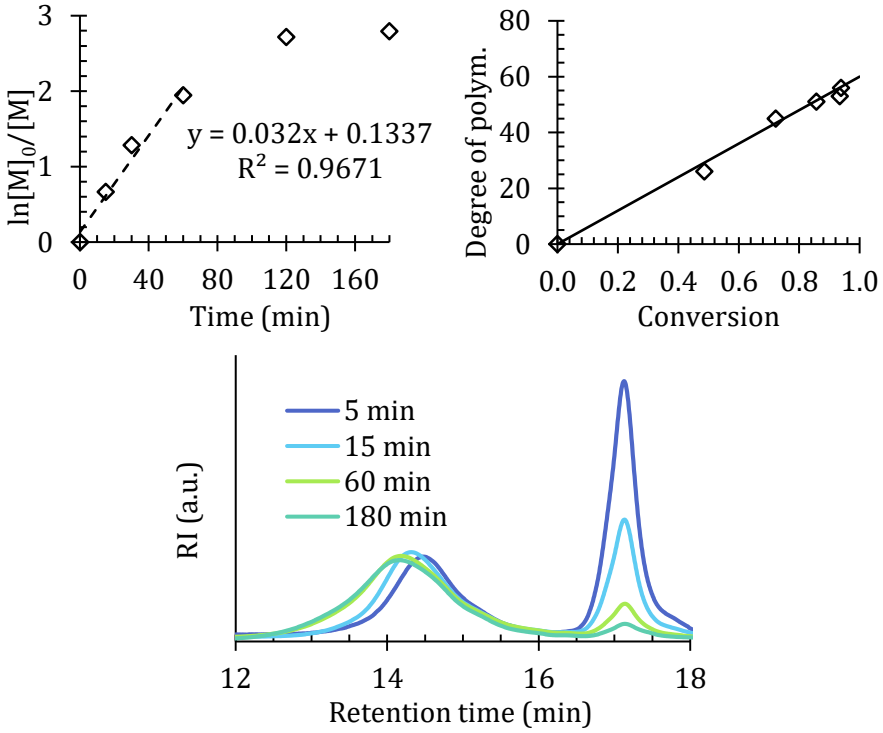

Figure 33: Kinetics plot (left) and degree of polymerisation vs conversion (right) for pPEGMAb homopolymerisation. Evolution of SEC traces during pPEGMAb polymerisation (bottom).

Monomer dilution in reaction media was found to be a key parameter to maintain low dispersity for longer reaction time. Consequently, the best reaction conditions of this screening were those in entry pPEGMAd and pPEGMAe of Table 2, showing the most promising candidates for subsequent chain extension, that represents the ultimate proof of chain-end activity as an ATRP macroinitiator.

pPEGMAc and pPEGMAd were employed in ATRP polymerisation of FA monomer to obtain AB type amphiphilic block copolymers (Scheme 8). They will be noted in the following discussion as PEGMAx-*b*-FAy, where x and y represent the mole percentage of PEGMA and FA repeating units respectively.

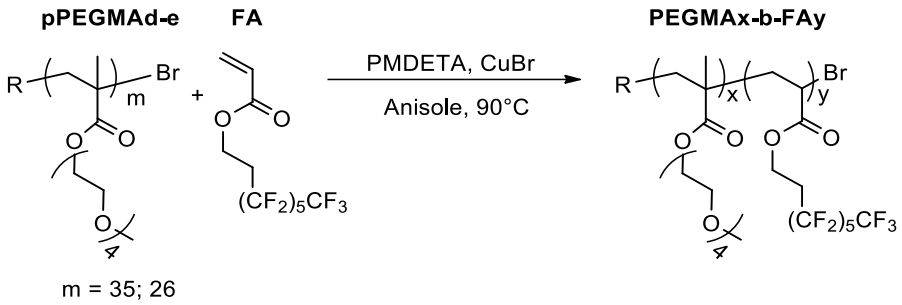

Scheme 8: ATRP synthesis of block copolymers PEGMAx-*b*-FAy.

In principle, just acting on the monomer/macroinitiator ratio it should be possible to modulate the degree of polymerisation of the second block, obtaining macromolecules with different hydrophilic/hydrophobic balance. Polymerisation reaction were initiated by the Br terminal in pPEGMAa-e polymers. pPEGMAa-e:PMDETA:CuBr catalytic system (1:1:1 molar ratio) in anisole was used.

In Figure 34, SEC analyses confirmed the insertion of the second block, with the shifting of copolymer peak toward higher molecular weight, with respect to the macroinitiators. No evidence of unreacted pPEGMAd, or new homopolymer formation were detected. This is a clear evidence of good chain-end fidelity in the previous PEGMA homopolymerisation. A second evidence of copolymerisation was from ^{1}H and ^{19}F NMR (Figure 35) spectroscopy, that showed the additional signals of the acrylate protons and the side chain fluorine.

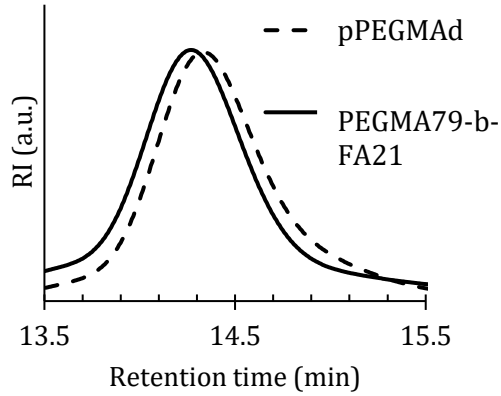

Figure 34: Comparison of SEC traces between pPEGMAd macroinitiator and its chain-extended block copolymer PEGMA79-*b*-FA21.

In Table 3 were summarised relevant reaction conditions for chain extension, and physical-chemical characterisation of their final purified products. Unfortunately, despite the different molar ratio between PEGMA repeating units and FA monomer in the feed, the final copolymer always showed a similar FA molar content (≈ 20%) at the end of the reaction.

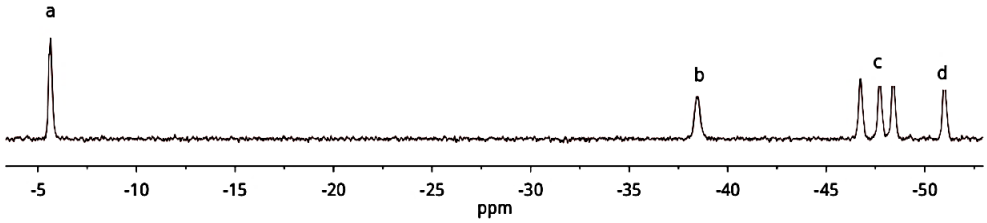

Figure 35: ^{19}F NMR of copolymer PEGMA79-*b*-FA21. a: CF_3, b: CF_2CH_2, c: CF_2, d: $C\underline{F_2}CF_3$.

Table 3: Reaction conditions for the ATRP of the FA block, and physical-chemical characterisation of the product PEGMAx-*b*-FAy.

	PEGMA79-b-FA21	***PEGMA80-b-FA20***	***PEGMA77-b-MAF23***
Macroinitiator	pPEGMAd	pPEGMAc	pPEGMAe
PEGMA:FA(MAF) feed[a]	70:30	80:20	80:20
M/I[b]	11	9	18
Solvent	Anisole	Anisole	Trifluoroethanol
T (°C)	90	90	40
Time (h)	15	15	24
Degree of pol.[c]	7	9	21
M_n *NMR*[d]	10700	14200	30100
M_n *SEC*[d]	6200	7400	11200
M_w/M_n[d]	1.14	1.30	1.23
Yield (%)	59	63	62

a Molar ratio of PEGMA repeating units and FA monomer in the feed.
b Monomer/initiator molar ratio.
c Degree of polymerisation of the second block and number average molecular weight, by ^{1}H NMR in acetone-d_6.
d Number average molecular weight and dispersity by SEC in $CHCl_3$.

A third chain extension was carried out on macroinitiator pPEGMAe, aiming higher molecular weight (Scheme 9). Considering the difficulties in increasing the length of the second block, a fluorinated solvent (trifluoroethanol, TFE) was selected for the polymerisation, in order to increase the affinity of the reaction medium with the fluorinated monomer. Moreover, perfluorohexylethyl methacrylate (MAF) was used in place of the acrylate (FA) to favour the initiation of the polymerisation.

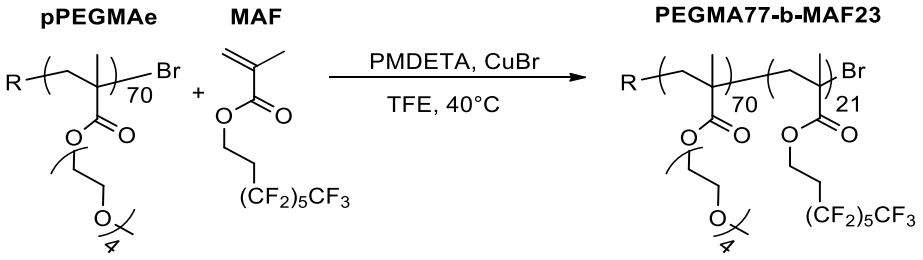

Scheme 9: ATRP synthesis of block copolymer PEGMA77-*b*-MAF23.

In this chain extension, an average degree of polymerisation of 21 for the second block was evaluated by ^{1}H NMR, from the integrated areas of the ^{1}H NMR characteristic signals (4.4 ppm for $COOCH_2$ of the two repeating units, 3.3 ppm OCH_3 for PEGMA and 2.5 CH_2CF_2 for FA). Successful chain extension was confirmed with ^{19}F NMR and SEC. SEC showed the shifting of copolymer peak toward higher molecular weight, with respect to its own macroinitiator. No evidences of unreacted pPEGMAe, or new homopolymer formation were detected. It worth noting that with trifluoroethanol solvent a significantly lower temperature (40°C instead of 70-90°C) could be used.

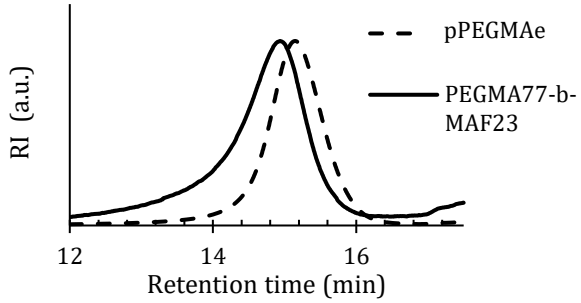

Figure 36: Comparison of SEC traces between pPEGMAe macroinitiator and its chain-extended block copolymer PEGMA77-*b*-MAF23.

2.1.1.3 pPEGMA homopolymer synthesis via Cu(0)-RDRP

A different PEGMA homopolymerisation route was explored, based on the copper(0) mediated reversible-deactivation radical polymerisation. Cu(0)-RDRP offers the advantage of being active at room or lower temperatures, in polar solvents like water, representing a mild and greener alternative to classic ATRP polymerisation.

The reaction (Scheme 10) was carried out with *in situ* generated Cu(0) particles,[77] coming from the rapid disproportion of CuBr in water in presence of a ligand able to stabilise Cu(II), such as PMDETA (initiator:CuBr:PMDETA 1:0.8:0.4 molar ratio). CuBr was allowed to disproportionate for 15 minutes in water at room temperature under nitrogen, resulting in a blue solution with fine Cu(0) particulate. In parallel, the water solution of monomer and initiator was

previously degassed by vigorous nitrogen bubbling, then injected in the first Schlenk tube, containing the catalytic system. Final monomer concentration was fixed to 0.36 g/ml and $[M]_0$:$[I]_0$ was 40 for all selected examples. Polymerisation was carried out at 0°C.

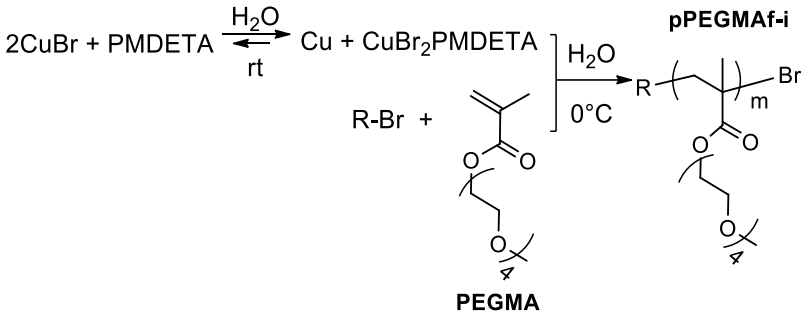

Scheme 10: Cu(0)-RDRP of PEGMA.

Three different bromine-terminated initiators (R-Br, Scheme 11) were investigated: EBPA, EBIBOH and TEGBIB, which were differentiated by an increasing hydrophilic character. While the first two are commercially available, the third was synthesised according to a literature procedure.[89]

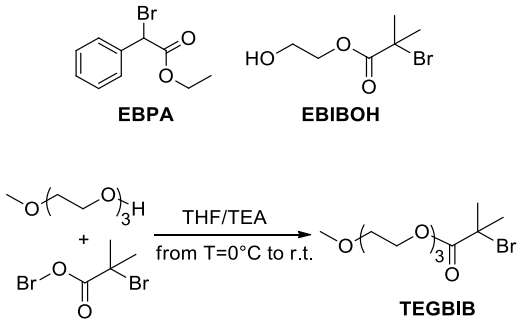

Scheme 11: Initiators used in Cu(0)-RDRP. EBPA and EBIBOH are commercially available. TEGBIB was synthesised from α-bromoisobutyryl bromide and triethyleneglycol monomethylether.

The reaction was in every case very fast, resulting in almost quantitative yield. The polymers were analysed by SEC chromatography (Table 4) resulting in high average number molecular weight M_n, with respect to the $M_{n\,target}$ = 12000 g/mol. Moreover, large values of M_w/M_n were obtained (2.3 – 1.8). A little beneficial

effect of the hydrophilicity of the initiator was revealed, with narrower dispersity for TEGBIB initiated polymerisations.

Table 4: Reaction condition for the Cu(0)-RDRP of PEGMA, and phsical-chemical characterisation of the products pPEGMAf-i.

	pPEGMAf	***pPEGMAg***	***pPEGMAh***	***pPEGMAi***
Initiator	EBPA	EBIBOH	TEGBIB	TEGBIB
Time	30	30	30	10
M_n *SEC*[a] *(g/mol)*	70200	61700	62700	30400
M_w/M_n[a]	2.3	2.1	2.0	1.8

a Number average molecular weight and dispersity by SEC in $CHCl_3$.

These results indicated that a poor control was maintained during the polymerisation in these conditions. The incidence of termination reactions and transfer reactions was substantial, thus affecting the growth of the active chains and providing a product with ill-defined macromolecular structure. In particular, chain end fidelity, crucial for chain-extension was compromised. To verify this, several chain-extension reactions were performed, with FA and MAF, in classical ATRP conditions. Cu(0)-RDRP reactions were also considered in 2,2,2-trifluoroetanol[90] and water. Chain-extension in water was tried with the aim to take advantage of the polymerisation induced self-assembly (PISA) effect.[79,82] Unfortunately, the insertion of a second block of fluorinated units was never observed in ^1H or ^{19}F NMR spectra or in SEC chromatograms.

The possibility to perform block copolymer synthesis in green solvent like water, with reduced content of heavy metal catalyst, at room temperature is fascinating. The production of concentrated dispersion of nanostructured polymeric aggregates, directly during the polymerisation, offered by PISA system is equally attractive. For these reasons, the optimisation of the polymerisation system to obtain a macroinitiator with quantitative conversions and high chain-end fidelity, in mild conditions, would represent a significant future development of this work. In the most optimistic scenario, such macroinitiator could be employed in a one-pot chain-extension, cutting the waste from intermediate purifications. If an amphiphilic system is addressed, a

PISA protocol could be realised with metal-mediated RDRP, expanding the field of this emerging polymer self-assembly technique.

2.1.1.4 PEGMAx-*co*-SiMAy random copolymers

A second set of amphiphilic random copolymers from hydrophilic poly(ethylene glycol) methyl ether methacrylate (PEGMA) and hydrophobic polydimethylsiloxane methacrylate (SiMA) was synthesised via atom transfer radical polymerisation (Scheme 12). The monomer:initiator ratio was kept constant (100:1) and the PEGMA:SiMA molar ratio in the feed was varied.

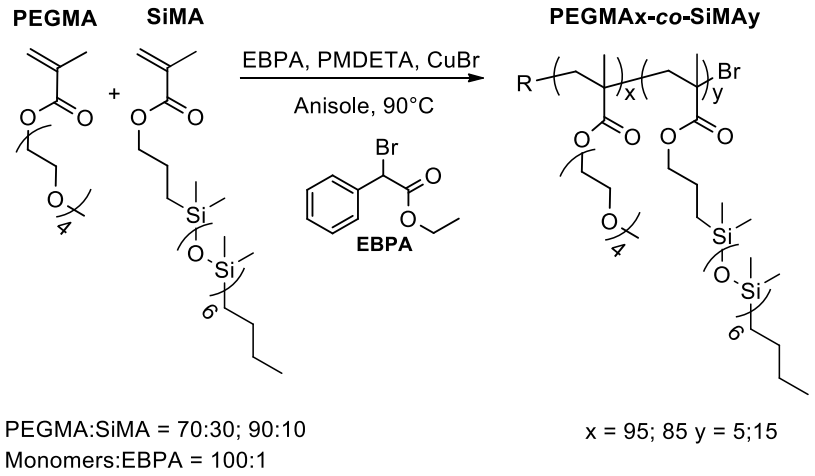

Scheme 12: Synthesis of amphiphilic/siloxane random copolymers via ATRP.

Two copolymerisations were carried out using EBPA:PMDETA:CuBr (1:1:1 molar ratio) catalytic system in anisole solution at 90°C for 24 hours.

Comonomer molar ratio was changed in the feed to obtain copolymers with different hydrophilic/phobic ratio. In every case PEGMA was the major component to obtain water-soluble copolymers.

The resulting copolymers were named PEGMAx-*co*-SiMAy, where x and y are the mole percentage content of the respective repeating units.

A third siloxane based copolymer was synthesised from a novel ATRP initiator containing a julolidine fluorescent molecular rotor moiety, named JBr (Scheme 13). Briefly, the initiator synthesis involved four reactive steps (Scheme 14). First, julolidine was formylated via Vilsmeier-Haack reaction. In parallel, 2-

hydroxyethyl α-bromoisobutyrate was prepared by esterification of α-bromoisobutiryl bromide with ethylene glycol, and then esterified with cyanoacetic acid to obtain (2-bromo-2-methylpropanoyloxyethyl) cyanoacetate. This was used in a Knoevenagel reaction with 9-formyljulolidine to obtain the final product 9-[2-(2-bromo-2-methylpropanoyloxyethyloxycarbonyl)-2-cyanovinyl]julolidine (JBr).

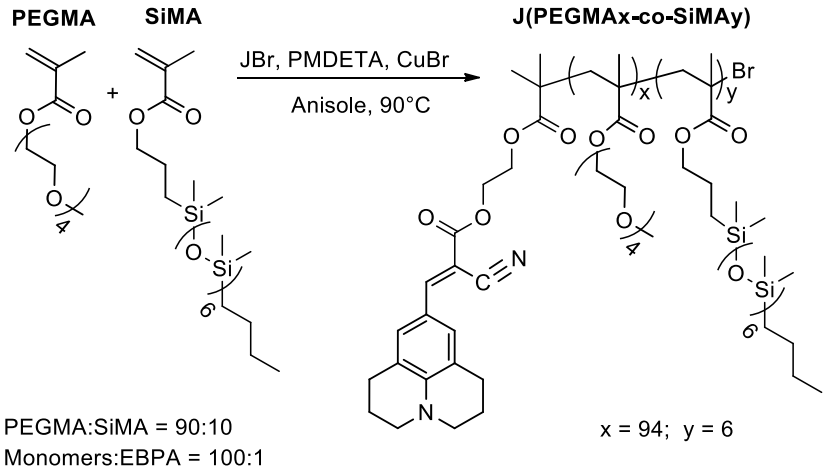

Scheme 13: Synthesis of amphiphilic/siloxane fluorescent random copolymer via ATRP.

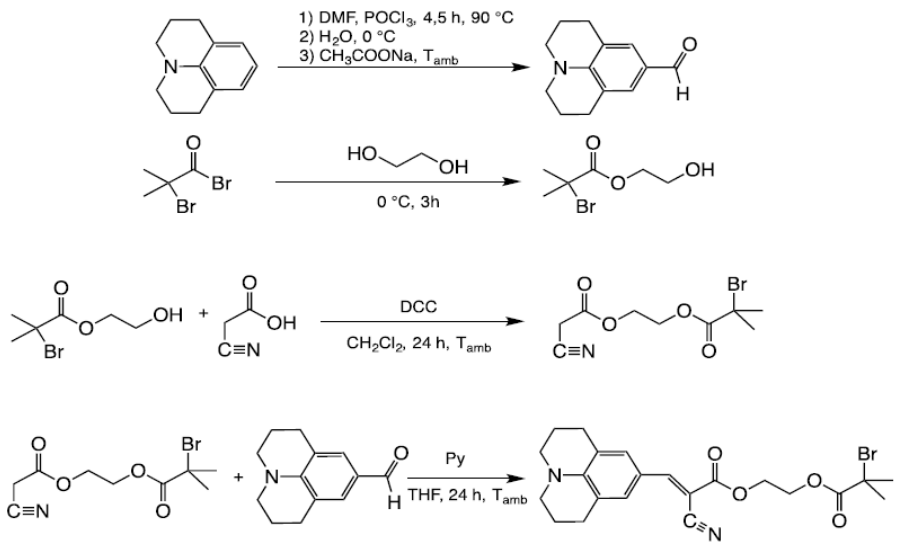

Scheme 14: Reaction scheme for the synthesis of the ATRP initiator JBr.

The julolidine-based initiator was used in the ATRP of PEGMA and SiMA giving a copolymer named J(PEGMAx-*co*-SiMAy) where J denote the presence of the julolidine terminal group. The ATRP reaction mechanism guaranteed the functionalisation of one terminal for macromolecular chain. Owing to the sensitivity of the fluorophore to micro-viscosity and local steric hindrance, the fluorescent terminal could be a useful probe for the single-chain folding and self-assembly of such an amphiphilic copolymer in selective solvents.

Physical-chemical properties of amphiphilic siloxane based random copolymers are reported in Table 5. Actual copolymerisation was confirmed in any case by SEC analysis, that showed monomodal molecular weight distributions with relatively low dispersity ($M_w/M_n < 1.6$). This was in fact affected by the fact that the starting materials themselves are oligomers with a polydisperisity around 1.2. It is worth noting that the absolute value of number molecular weight from SEC analysis could be different from the real value due to the large chemical and structural difference between the samples and the PMMA standards used for calibration. The much broader molecular weight distribution of the copolymer J(PEGMA94-*co*-SiMA6) SEC required consideration. The broadening of molecular weight distribution indicated a loss of control on secondary reactions, such as irreversible termination and chain transfer. The H· abstraction in the α position with respect to the aromatic ring in the julolidine residue would lead to the formation of a radical highly stabilised by resonance. That in turn would cause a higher incidence of chain transfer reactions between the julolidine moiety and the growing chains, leading to a less defined macromolecular structure.

Table 5: Physical-chemical properties of amphiphilic/siloxane random copolymers.

Copolymer	***M_n[a] (g/mol)***	***M_w/M_n[a]***	***PEGMA[b] (%mol)***	***J[c] (%mol)***
PEGMA95-co-SiMA5	2900	1.6	95	--
PEGMA85-co-SiMA15	3700	1.5	85	--
J(PEGMA94-co-SiMA6)	33200	2.1	96	1.1

a Number average molecular weight and dispersity by SEC with $CHCl_3$.
b Molar percentage in the copolymer.
c Molar percentage in the copolymer, determined by UV.

Chemical composition of siloxane based copolymers was determined by ^{1}H NMR spectra, from the integral area of some characteristic signals in repeating unit side chain: 0.5 ppm for Si-$(CH_3)_2$ in polydimethylsiloxane and 3.5 ppm for OCH_3 terminal in poly(ethylene glycol). Julolidine residue content was determined by UV absorption spectra of copolymer solutions in chloroform, with a calibration curve obtained from $5\cdot10^{-7}$–$5\cdot10^{-5}$ M chloroform solutions of the fluorescent initiator. The molar extinction coefficient variation from monomer to polymer was assumed to be negligible.

2.1.2 Thermal properties

Thermal characterisation of synthesised amphiphilic copolymers, was performed with differential scanning calorimetry (DSC). In particular, DSC curves displayed different glass transitions for the analysed materials, that are not expected to form any crystalline phase. Glass transition temperatures (T_g) were identified as the inflection point of the thermogram region corresponding to the transition, in the second heating ramp of the cycle. For every glass transition, the specific heat variation (ΔC_p) was also measured.

2.1.2.1 PEGMAx-*co*-FAy

Amphiphilic fluorinated random copolymers, their fluorescent analogue and corresponding homopolymers, when examined between -80°C and 110°C (scanning at 20°C/min) showed a single T_g (Table 6).

All investigated copolymers are completely amorphous, with glass transition temperature below room temperature, in between the glass transition temperatures of the corresponding homopolymers. To a first approximation, Fox empirical equation describes the variation of T_g in a random copolymer or homogenous blend, as function of weight fraction (w) and homopolymer T_g,s, following the equation:

$$\frac{1}{T_g} = \frac{w_1}{T_{g1}} + \frac{w_2}{T_{g2}} \qquad \text{Eq. 4}$$

Table 6: Thermal properties of amphiphilic/fluorinated copolymers.

Copolymer	T_g (°C)	ΔC_p (J/gK)
PEGMA90-co-FA10	-52	0.56
PEGMA77-co-FA23	-53	0.67
PEGMA69-co-FA31	-47	0.57
PEGMA29-co-FA71	-26	0.56
PEGMA80-b-FA20	-50	0.67
PEGMA74-co-FA25-co-JCBF1	-52	0.58
pPEGMAb	-54	0.71
pFA	-8	0.19

Experimental values of T_gs and their linear regression were compared with the curve predicted by Fox equation in Figure 37. The plot showed only a moderate agreement of experimental and predicted values. Up to 30% in weight of FA the copolymers exhibited a glass transition temperature similar to that of pPEGMAb homopolymer. The deviation could be ascribed to the poor miscibility of the two components, characterised by an high hydrophilic/hydrophobic contrast.

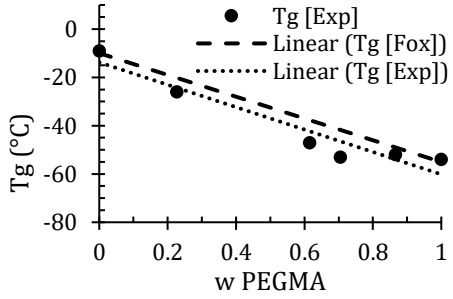

Figure 37: Experimental glass transition temperatures T_g for amphiphilic/fluorinated random copolymers and the predicted trend expected from Fox equation.

2.1.2.2 PEGMAx-*co*-SiMAy

PEGMA95-*co*-SiMA5 and J(PEGMA94-*co*-SiMA6), examined between -80°C and 110°C (scanning at 20°C/min), displayed two glass transition temperatures that are compared with those of the corresponding homopolymers in Table 7.

Table 7: Thermal properties of amphiphilic/siloxane copolymers.

Copolymer	T_{g1} [a] (°C)	T_{g2} [b] (°C)	ΔC_{p1} [a] (J/gK)	ΔC_{p2} [b] (J/gK)
PEGMA95-co-SiMA5	-125	-55	0.41	0.39
J(PEGMA94-co-SiMA6)	-126	-58	0.56	0.38
pPEGMAb	--	-54	--	0.71
pSiMA[c]	-107	--	0.95	--

a Relative to polydimethylsiloxane SiMA component.
b Relative to poly(ethylene glycol) PEGMA component.
c Homopolymer synthesised by conventional free radical polymerisation.

All amphiphilic siloxane based random copolymers showed a similar thermal behaviour, independent of the ATRP initiator used for the synthesis. DSC traces (Figure 38) clearly showed two distinct glass transitions, both well under room temperature. One at lower temperature (T_{g1} = -125°C) related to the pSiMA thermal behaviour, the other at higher temperature (T_{g2} = -55°C) similar to the analogue pPEGMAb homopolymer.

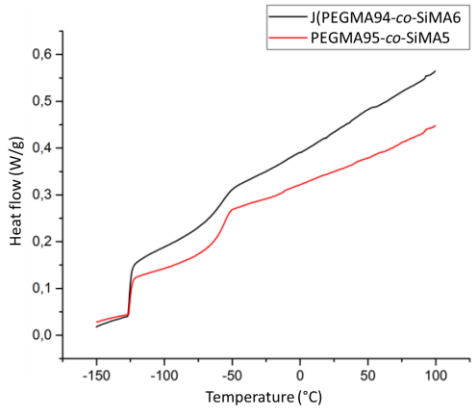

Figure 38: DSC second heating curves for amphiphilic/siloxane random copolymers.

These results are somewhat surprising for random copolymers, but clearly pointed out that, in bulk, oxyethylene and siloxane side chains were able to self-assembly in well separated microdomains. Each domain obeys to the thermal transitions of the corresponding homopolymers, as it's often seen in block copolymers.

2.1.3 NMR relaxometry study of PEGMAx-*co*-FAy

In order to obtain information on the dynamic properties of the PEGMAx-*co*-FAy copolymers, which could be related to their aggregation and assembling behaviour, NMR relaxometry techniques were applied to the samples reported in Table 8. In particular, the mobility of both main- and side-chains was investigated as a function of the PEGMA/FA ratio, mainly exploiting the measurement of ^{1}H and ^{19}F spin-spin relaxation times T_2. These monotonically increase with increasing degree of mobility of the molecular fragment to which the nuclei belong.

Table 8: Molar composition (mol%) of the PEGMAx-*co*-FAy copolymers studied by means of NMR relaxometry.

Sample	***PEGMA (mol%)***	***FA (mol%)***
pPEGMAb	100	0
PEGMA90-co-FA10	90	10
PEGMA69-co-FA31	69	31
PEGMA29-co-FA71	29	71
pFA	0	100

All the experiments were carried out under low-resolution conditions, at a low magnetic field corresponding to ^{1}H and ^{19}F Larmor frequencies of 20.8 and 19.6 MHz, respectively. Under these conditions the spectral resolution is substantially absent and all the analyses are performed in the time rather than in the frequency domain.

In order to achieve a detailed picture of the dynamics of the systems under investigation, T_2's were measured combining solid echo and CPMG (Carr-Purcell-Meiboom-Gill) experiments. The analysis of ^{1}H or ^{19}F FID (Free Induction Decay), recorded on-resonance by means of the solid echo technique, allows regions of the sample with different degree of mobility to be identified and quantified. In particular, through the solid echo pulse sequence signals of components with very short T_2 ($\sim$ 10-20 μs), usually arising from rigid domains and affected by strong homonuclear dipolar couplings, are correctly acquired,

and contribute to the FID together with the signals from more mobile domains (T_2 on the order of tens or hundreds of μs). The recorded FID can then be fitted with a linear combination of functions (f_i), chosen among exponential, Gaussian, Pake, Weibullian or Abragamian functions, each characterised by a distinct T_2 relaxation time (T_{2i}) and a weight (w_i). T_{2i} is related to the degree of mobility, while w_i approximately corresponds to the fractional population of ^{1}H (or ^{19}F) nuclei in the domain represented by the *i*th function.[91,92] However, the analysis of the "solid echo FID" does not provide a correct determination of the intrinsic T_2 values of very mobile components (T_2 > 100 μs), since their slowly decaying signals can be also affected by external conditions such as resonance offset and fluctuations and inhomogeneity of the external magnetic field. An accurate measurement of the T_2 values of the mobile components was achieved by fitting the relaxation curves recorded using the dedicated CPMG[93] experiment. It is worth noticing that CPMG curves contain contributions from mobile components only, while signals from rigid domains with short T_2 are completely lost.

2.1.3.1 ^{19}F T_2 results

Measurements of ^{19}F T_2 provided information on the mobility of the fluorinated FA side chains.

^{19}F solid echo FID's were acquired on all the investigated samples. In all cases no rigid component with very short T_2 was detected and the ^{19}F FID's (here not reported) were characterised by a very long decay, indicating that FA side chains experience a high degree of mobility.

For this reason, ^{19}F T_2's were determined by means of CPMG experiments. The CPMG relaxation curve of sample PEGMA29-*co*-FA71, together with the corresponding best-fitting function, is reported as an example in Figure 39, while the best-fitting parameters obtained for all the samples are reported in Table 9. For all the samples, the experimental CPMG relaxation curves were fitted to a linear combination of two exponential functions, exp_a and exp_b:

$$^{19}F\ CPMG\ Fit.Func. = w_a exp_a + w_b exp_b = w_a e^{-t/T_{2a}} + w_b e^{-t/T_{2b}} \qquad \text{Eq. 5}$$

where exp_a is characterised by shorter T_2 values, ranging from 570 to 1600 μs, and exp_b by longer T_2 values, ranging from 1800 to 5400 μs. The longer-T_2 component, exp_b, can be ascribed to the ends of the fluorinated chains, i.e. the CF_3 and the nearest CF_2, which can probably experience a higher degree of mobility, while the shorter-T_2 component, exp_a, likely arises from the other CF_2 groups, having a more restricted mobility. The values of the weights, w_a and w_b, of the two exponential functions, support this interpretation.

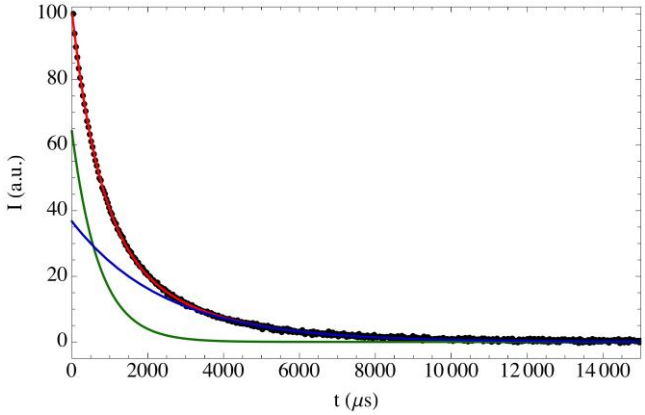

Figure 39: Fitting of the experimental ^{19}F CPMG relaxation curve of sample PEGMA29-*co*-FA71. The experimental data (•), the best-fitting function (–), and the two exponential components, exp_a (–) and exp_b (–), are shown.

Table 9: Best-fitting parameters obtained from the fitting of the experimental ^{19}F CPMG relaxation curves to a linear combination of two exponential functions, exp_a and exp_b. For each sample, the values of ^{19}F T_2 relaxation times (T_{2a} and T_{2b}) and of the weights of the functions in the linear combination (w_a and w_b) are reported. The error on the values of T_2 and w was always estimated to be ≤ 10 %.

Sample	***exp$_a$***		***exp$_b$***	
	T_{2a} (μs)	***w_a (%)***	***T_{2b}(μs)***	***w_b(%)***
PEGMA90-co-FA10	1600	60	5400	40
PEGMA69-co-FA31	980	63	3400	37
PEGMA29-co-FA71	720	63	2400	37
pFA	570	67	1800	33

T_2 values of both exponential components are found to be quite long for all the investigated samples, indicating a high degree of mobility of the fluorinated side chains. However, a progressive shortening of the T_2 values, accompanied by a slight increase in w_a, was observed by decreasing the PEGMA/FA ratio (Table 9). These results clearly indicate that the mobility of the FA side chains progressively decreases by increasing the relative amount of the FA block in the copolymer. This can be explained with the establishment of a correspondingly increasing degree of assembling of the fluorinated side chains.

2.1.3.2 ^{1}H T_2 results

^{1}H solid echo FID's were recorded and analysed for all the samples under investigation. In Figure 40a the experimental ^{1}H FID of PEGMA29-*co*-FA71 and the corresponding best-fitting function are shown, while in Table 10 the best-fitting parameters obtained for all the samples are reported. In all cases the ^{1}H FID's were well reproduced with a linear combination of one exponential and two Gaussian functions:

$$^1H\ FID\ Fit.Func. = w_{gau,a}\ gau_a + w_{gau,b}\ gau_b + w_{exp} exp$$
$$= w_{gau,a}\ e^{-(t/T_{2gau,a})^2} + w_{gau,b}\ e^{-(t/T_{2gau,b})^2} + w_{exp}\ e^{-t/T_{2exp}} \qquad \text{Eq. 6}$$

The Gaussian function gau_a is characterised by a very short T_2 value of 19 μs, typical of solid-like very rigid components, and can be mainly ascribed to ^{1}H nuclei in the main chain of the copolymer. On the other hand, the functions gau_b and *exp* are characterised by longer T_2 values of about 85 μs and in the range 260-1800 μs, respectively, and can be mainly assigned to protons in the side chains, experiencing intermediate (gau_b) and high (*exp*) degrees of mobility. This assignment is in good agreement with the fact that for all the investigated samples the weight of gau_a (w_a) approximately corresponds to the fractional populations of protons in the main chain (%H_{MC}), as reported in Table 10.

Table 10: Best-fitting parameters obtained from the fitting of the experimental ^{1}H solid echo FID's to a linear combination of one exponential (*exp*) and two Gaussian (gau_a and gau_b) functions. For each sample, the values of ^{1}H T_2 relaxation times ($T_{2gau,a}$, $T_{2gau,b}$, T_{2exp}) and of the weights of the functions in the linear combination ($w_{gau,a}$, $w_{gau,b}$, w_{exp}) are reported. The error on the values of T_2 and *w* was always estimated to be ≤ 10 %.

Sample	gau_a		gau_b		*exp*		
	$T_{2gau,a}$ (μs)	$w_{gau,a}$ (%)	$T_{2gau,b}$ (μs)	$w_{gau,b}$ (%)	T_{2exp} (μs)	w_{exp} (%)	%H_{MC}
pPEGMAb	19	12	85	7	1800	81	18
PEGMA90-co-FA10	19	15	85	9	1100	76	19
PEGMA69-co-FA31	19	18	85	11	809	71	21
PEGMA29-co-FA71	19	25	85	21	605	54	28
pFA	19	48	85	34	260	18	43

A more accurate description of the ^{1}H T_2 relaxation behaviour of the mobile PEGMA and FA side chains was achieved by performing ^{1}H CPMG experiments. The ^{1}H CPMG relaxation curve recorded for sample PEGMA29-*co*-FA71 is reported, as an example, in Figure 40b, together with its best-fitting function.

The best-fitting parameters obtained for all the samples are reported in Table 11. In all cases the ^{1}H CPMG curves were fitted to a linear combination of three exponential functions

$$^1\text{H } CPMG\ Fit.Func. = w'_a exp'_a + w'_b exp'_b + w'_c exp'_c$$
$$= w'_a e^{-t/T'_{2a}} + w'_b e^{-t/T'_{2b}} + w'_c e^{-t/T'_{2c}} \quad \text{Eq. 7}$$

characterised by different T_2 values, and ascribable to PEGMA and FA side chains located in differently mobile environments. In particular, the degree of mobility increases in passing from exp'_a to exp'_b to exp'_c.

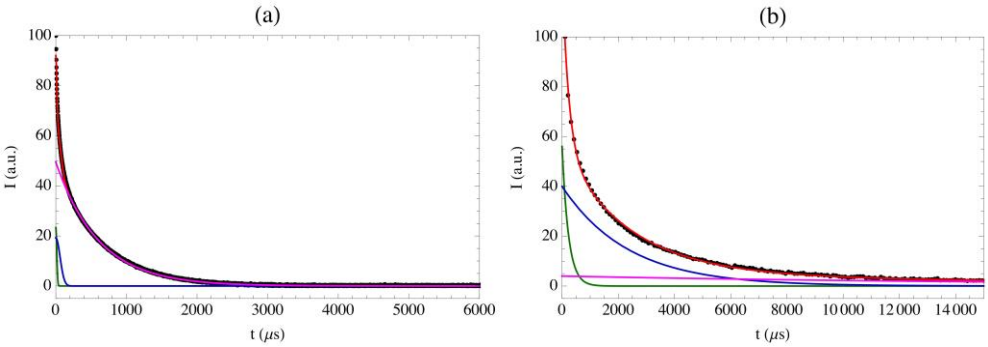

Figure 40: (a) Fitting of the experimental ^{1}H solid echo FID of PEGMA29-*co*-FA71. The experimental data (•), the best-fitting function (–), and the three components of the linear combination, gau_a (–), gau_b (–), and *exp* (–), are shown. (b) Fitting of the experimental ^{1}H CPMG relaxation curve of PEGMA29-*co*-FA71. The experimental data (•), the best-fitting function (–), and the three exponential functions exp'_a (–), exp'_b (–), and exp'_c (–), are shown.

Table 11: Best-fitting parameters obtained from the fitting of the experimental ^{1}H CPMG relaxation curves to a linear combination of three exponential functions (exp'_a, exp'_b, and exp'_c). For each sample, the values of ^{1}H T_2 relaxation times (T'_{2a}, T'_{2b}, and T'_{2c}) and of the weights of the functions in the linear combination (w'_a, w'_b, and w'_c) are reported. The values of *PWRA*, calculated as described in the text, are also reported. The error on the values of T_2 and *w* was always estimated to be ≤ 10 %.

Sample	***exp'$_a$***		***exp'$_b$***		***exp'$_c$***		***PWRA · 10^2 (μs^{-1})***
	T'_{2a} (μs)	***w'_a (%)***	***T'_{2b} (μs)***	***w'_b (%)***	***T'_{2c} (μs)***	***w'_c (%)***	
pPEGMAb	560	36	5700	49	21400	15	0.1
PEGMA90-co-FA10	316	34	3400	49	11900	17	0.1
PEGMA69-co-FA31	214	37	2300	42	7700	21	0.2
PEGMA29-co-FA71	230	56	2400	40	17400	4	0.3
pFA	53	64	270	33	11000	3	1.3

It can be noticed that the values of T_2 generally decrease by decreasing the PEGMA/FA ratio (with the exception of T'_{2c}, for which the trend is not very regular), while the weight of the shortest-T_2 component, w'_a, strongly increases. In Table 4 the values of PWRA (Population Weighted Rate Average), calculated as

$$PWRA = \frac{1}{100}\left(\frac{w'_a}{T'_{2a}} + \frac{w'_b}{T'_{2b}} + \frac{w'_c}{T'_{2c}}\right) \quad \text{Eq. 8}$$

and representing a sort of average relaxation rate of a sample, are also reported. PWRA progressively increases by decreasing the PEGMA/FA ratio, confirming an average "shortening" of the ^{1}H CPMG relaxation curves. Similarly to what was observed for the sole fluorinated side groups from ^{19}F T_2 measurements, these results clearly indicate that the increase in the relative amount of FA blocks in the copolymer, and therefore the increase in the amount of fluorinated side chains, possibly interacting and assembling between each other, significantly affects the mobility of both FA and PEGMA side chains, which becomes more and more hindered.

2.1.4 Single-chain folding and self-assembly of amphiphilic copolymers in solution

2.1.4.1 Dynamic light scattering of PEGMAx-*co*-FAy solutions

DLS measurements of amphiphilic/fluorinated copolymer solutions were performed to directly monitor the ability to spontaneously assemble in nanostructures, varying by the solvent, concentration and temperature on PEGMAx-*co*-FAy series, and PEGMA74-*co*-FA25-*co*-JCBF1 polymer. For every sample, 5mg/ml (if not otherwise stated) solutions in water or other organic solvents were prepared, dissolving the solid polymer in 0.2 μm filtered solvents of the highest purity available. All the solutions were analysed at 25°C and at temperatures varied in steps of ≈5°C, in both heating and cooling cycles.

At room temperature clear solutions of PEGMAx-*co*-FAy copolymers in water showed bimodal intensity distributions of scatters, characterised by a

population with a small hydrodynamic diameter (D_h ≈ 4 - 8 nm) and population with a larger hydrodynamic diameter (D_h ≈ 170 - 300 nm) (Table 12).

In Figure 41 were reported intensity and volume size distributions for PEGMA77-*co*-FA23, as an example. The presence of the population of smaller scatters was consistent with the formation of folded macromolecular chains. The presence of larger scatters was ascribed to collective multichain aggregates which were difficult to dissolve at a molecular level just by mechanical stirring the solution. The volume distribution emphasised that the predominant form in solution is the folded unimer micelle, disregarding the misrepresentation in intensity distribution due to the dependence of intensity I to d^6, coming from Rayleigh scattering law:

$$I = I_0 \frac{(1+cos^2\theta)}{2R^2}\left(\frac{2\pi}{\lambda}\right)^4\left(\frac{n^2-1}{n^2+2}\right)^2\left(\frac{d}{2}\right)^6 \qquad \text{Eq. 9}$$

where R is the distance of the scatter, θ is the scattering angle, λ the wavelength, n the refractive index, and d is the diameter of the scattering particle. Thus, the contribution of collective aggregates was negligible in volume distribution, that better represents the respective contribution to multimodal scattering distributions.

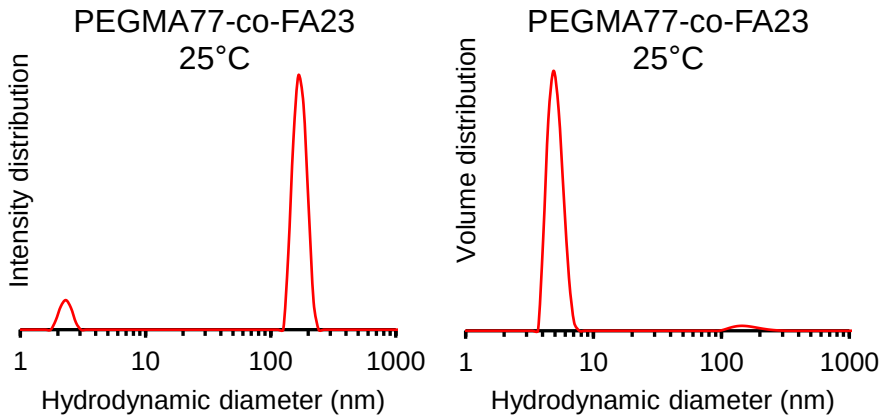

Figure 41: DLS intensity and volume size distributions for PEGMA77-*co*-FA23 (5 mg/ml) solution in water at room temperature.

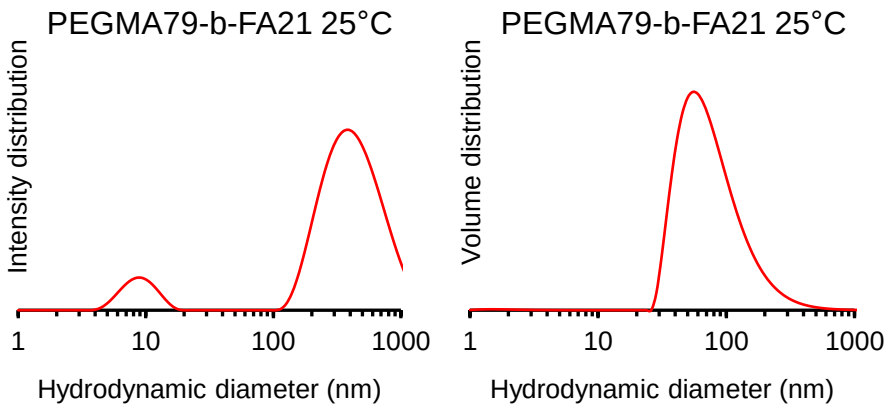

Figure 42: DLS intensity and volume size distributions for PEGMA79-*b*-FA21 (5 mg/ml) solution in water at room temperature.

The comparison of DLS intensity and volume size distribution between a random (Figure 41) and a block copolymer (Figure 42) with similar composition revealed that the block copolymer, in water, had the tendency to form bigger 'classical' multichain micellar aggregates. Thus, in selective solvents the block macromolecular architecture favoured intermolecular hydrophobic interaction, instead of intramolecular interaction which is crucial for the polymer single-chain folding.

Table 12: Average hydrodynamic diameters of aqueous solution of the amphiphilic/fluorinated copolymers, from DLS intensity size distributions at 5mg/ml.

Copolymer	D_h^{1a} ***(nm)***	D_h^{2b} ***(nm)***
PEGMA90-co-FA10	8±1	230±60
PEGMA77-co-FA23	4±1	170±7
PEGMA69-co-FA31	8±1	300±90
PEGMA77-b-MAF23	17±5	300±70
PEGMA79-b-FA21	6±3	430±70
PEGMA74-co-FA25-co-JCBF1	4±1	260±60

a Population of smaller scatters in the bimodal intensity distribution.
b Population of larger scatters in the bimodal intensity distribution.

To consider the effect of temperature on solution self-assembly, the case of PEGMA69-*co*-FA31 will be discussed in detail, as a representative for all the analogue amphiphilic/fluorous random copolymers of this work. DLS measurements at variable temperature proved that above a critical temperature (T_c = 49°C), the smaller scatters (8 nm, stable at room temperature) collapsed into larger aggregates of 500-1200 nm, with very narrow distributions (Figure 43) in both intensity and volume size distribution. DLS measurements, while cooling down the samples, confirmed that this phenomenon is reversible with no hysteresis (Figure 45). These two different states could be easily distinguished by naked eyes (Figure 44), for the solutions at room temperature were perfectly clear, while above T_c they appeared cloudy, due to the larger scatters.

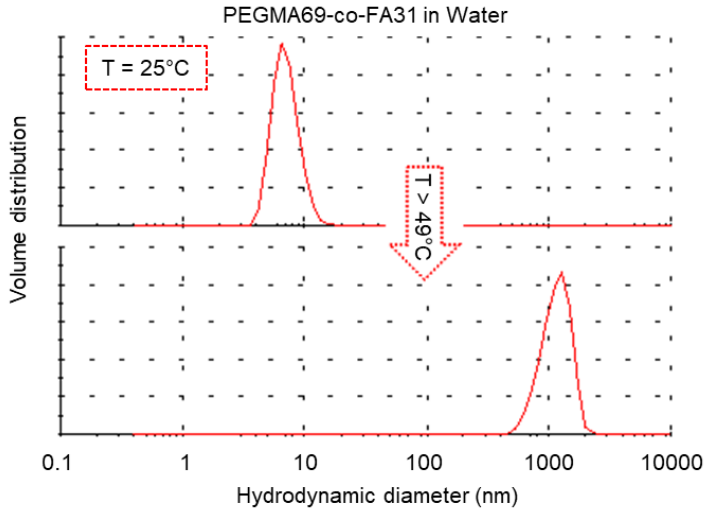

Figure 43: DLS volume size distributions for PEGMA69-*co*-FA31 solution (5 mg/ml) in water at room temperature (above) and at $T > T_c$ (bottom).

Figure 44: Photographs of a clear solution (T=25°C) of amphiphilic/fluorous random copolymer (left) and the corresponding cloudy dispersion at T>T_c (right).

Figure 45 showed that the T_c was weakly dependent on copolymer concentration for solutions between 5 and 0.5 mg/ml (going from 49.1°C to 47.9°C respectively). Below the respective T_c values, size distribution was stably centred at ~8 nm regardless of concentration, with increasing temperature. This D_h value was consistent with that of the unimer micelle of folded polymer chains. Above T_c the copolymer could self-reorganise in larger particles, as water dispersion, with an average D_h value that in these conditions depended on the copolymer concentration. Values were in the micrometric range between 2-5 mg/ml concentrations, and decreased to ~0.5 μm at 0.5 mg/ml (Figure 45). Solution with concentration lower than 0.5 mg/ml were not analysed at DLS, because of their poor scattering intensities.

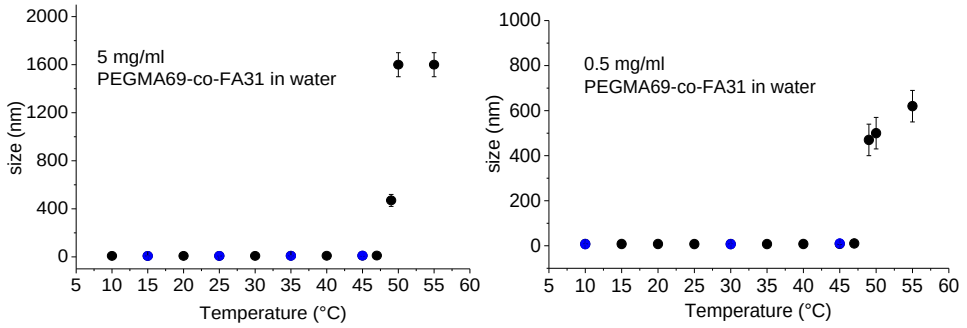

Figure 45: Hydrodynamic diameter as a function of temperature, measured by DLS at 5 mg/ml (left) and 0.5 mg/ml (right) of PEGMA69-*co*-FA31 in water during heating (•) and cooling (•).

While this temperature driven self-assembly was maintained in all the series of PEGMAx-*co*-FAy, a dependence of T_c value on the copolymer composition, at a fixed concentration, emerged. First, it is worth remarking the inherently thermoresponsive nature of PEGMA homopolymer. It shows a phase diagram with a lower critical solution temperature (LCST) in water, as function of the length of the oxyethylene side chain in the repeating unit. For PEGMA with M_n = 300 g/mol LCST values in the range 66 - 76°C were reported.[94,95] The amphiphilic/fluorinated random copolymers of this work showed a similar thermoresponsive behaviour, although with increasing hydrophobic character the T_c value in water could be regularly tuned and lowered down to 49°C for PEGMA69-*co*-FA31 (see Table 13).

Table 13: Critical Temperature (LCST) for amphiphilic/fluorinated random copolymers in water and average hydrodynamic diameter of the aggregated particles.

Copolymer	***T_c [a] (°C)***	***D_h [b] (nm)***
pPEGMA[c]	*66*	*nd*
PEGMA90-co-FA10	59	1500±200
PEGMA77-co-FA23	57	390±20
PEGMA69-co-FA31	49	1600±100
PEGMA77-b-MAF23	60	1300±400
PEGMA74-co-FA25-co-JCBF1	55	400±40

a Critical temperature recorded in DLS experiment at 5 mg/ml.
b Average hydrodynamic diameter above T_c measured by DLS at 5 mg/ml.
c Literature value from ref.[95]

The same considerations were extended to the self-assembly of PEGMA74-*co*-FA25-*co*-JCBF1 water solutions. Incorporation of the fluorescent moiety did not inhibit the chain folding or the temperature responsive aggregation behaviour. DLS measurements revealed bimodal intensity size distribution of scatters at room temperature (Table 12), and the reversible thermoresponsive aggregation was shown in Figure 46, with a T_c of 55°C at 5mg/ml copolymer concentration. In Figure 46 were reported volume size distributions of 5 mg/ml solution in water, before and after the transition triggered by temperature.

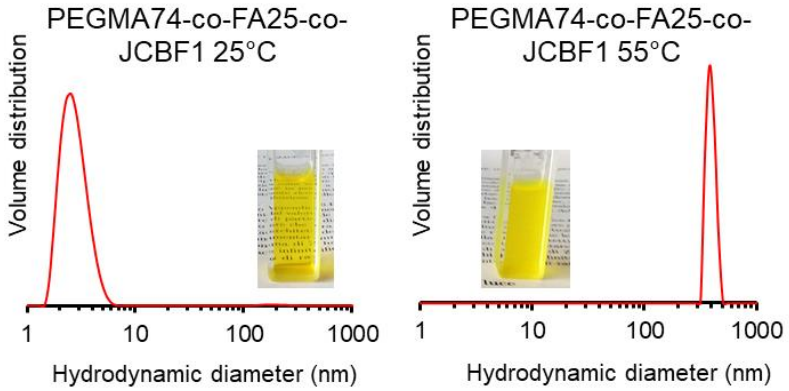

Figure 46: DLS volume size distributions for PEGMA74-*co*-FA25-*co*-JCBF1 5 mg/ml solution in water at room temperature (left) and at $T>T_c$ (right). In the insets are reported photographs of the clean solution at room temperature and the turbid dispersion at $T>T_c$.

DLS measurements of acetone solutions of PEGMA69-*co*-FA31 and PEGMA90-*co*-FA10 displayed analogous bimodal distribution of scatters at room temperature (D_h^1 = 8-10 nm and D_h^2 = 150-200 nm), stable up to 50°C. DLS measurements of trifluorotoluene (TFT) solutions revealed a bimodal distribution of scatters at 25°C (D_h^1 = 7-9 nm and D_h^2 = 100 nm), while between 30°C and 90°C the bigger aggregates were reduced in size and gradually disappeared. In both organic solvents the LCST-like behaviour observed in water is absent.

The aqueous solvent seems crucial to trigger the self-assembling of PEGMAx-*co*-FAy in folded unimer micelles and the temperature driven aggregation in a thermophilic superstructure. This may open the possibility to design novel intriguing drug delivery carriers taking advantage of such peculiar phenomenon in physiological conditions. However, more detailed information is needed to understand how the temperature influences the structural arrangement of the macromolecule when existing as single non-interacting nanoobjects dissolved in aqueous solutions, and while they interact in water-dispersed assembled superstructures above T_c.

2.1.4.2 Small Angle Neutron Scattering

To further understand the self-assembly process, elastic neutrons scattering was used to investigate size, shape and spatial arrangement of PEGMAx-*co*-FAy polymers on length scales between 0.25-300 nm.

Small angle neutron scattering (SANS) experiments were carried out by using the high flux beam line SANS2D at the ISIS facility (Oxford, UK), where preliminary ISIS Xpress service beamtime was allocated (March 2017) to demonstrate sample suitability. This allowed to confirm the DLS findings on amphiphilic/fluorous copolymer single-chain folding, thus detailed structural information, inaccessible by DLS experiments, only were provided through SANS analysis.

In place of water, deuterated water, D_2O was used to provide the necessary contrast. PEGMA69-*co*-FA31 and PEGMA90-*co*-FA10 samples were selected and dissolved at 5 mg/ml, and SANS measurements were performed below and above T_c (at 55 and 65°C, respectively.)

The results are shown in Figure 47. The Guinier analysis of the low-Q region of the scattering law at 25 °C provides values of the radius of gyration, consistent with the DLS results, of 3.4 ± 0.2 and 3.7 ± 0.2 nm for PEGMA69-*co*-FA31 and PEGMA90-*co*-FA10, respectively. For the PEGMA69-*co*-FA31 the mid-Q part of the form factor reveals a monodisperse polymer coil with a slightly ellipsoidal shape characterised by a minor, a, and major, b, radii of 2.2 and 4.7 nm, (a:b ratio of about 1:2) respectively. In the same conditions, the PEGMA90-*co*-FA10 sample is equally monodisperse showing a quite elongated ellipsoidal shape with an a:b axis ratio of 1:5 (a=1.0 and b= 4.9 nm).

Above the transition temperatures, i.e. at 55°C for PEGMA69-*co*-FA31 and 65 °C for PEGMA90-*co*-FA10, the dramatic change of the scattering profiles highlights the occurrence of an aggregation process in agreement with the DLS findings. Precise evaluation of the aggregates size was not available with the instrument configuration. The scattering profiles in the mid and high-Q regions, i.e. from 0.03 to 0.2 $Å^{-1}$ indicated that also the shape of individual chains composing the aggregates is preserved.

To complete the study of the temperature driven self-assembly process of these copolymers a proposal was submitted and accepted, with experiments

scheduled at the beginning of 2018 at Larmor instrument (ISIS facility, Oxford, UK). The aim is to extend the characterisation with more detailed study of the surface morphology and distribution of hydrophilic and perfluorinated moieties, and their response to temperature changes. Roughness and structural relative arrangements of the hydrophilic and hydrophobic component could be assessed by selectively matching one of the components with mixtures of D_2O/H_2O that offer different scattering contrast.

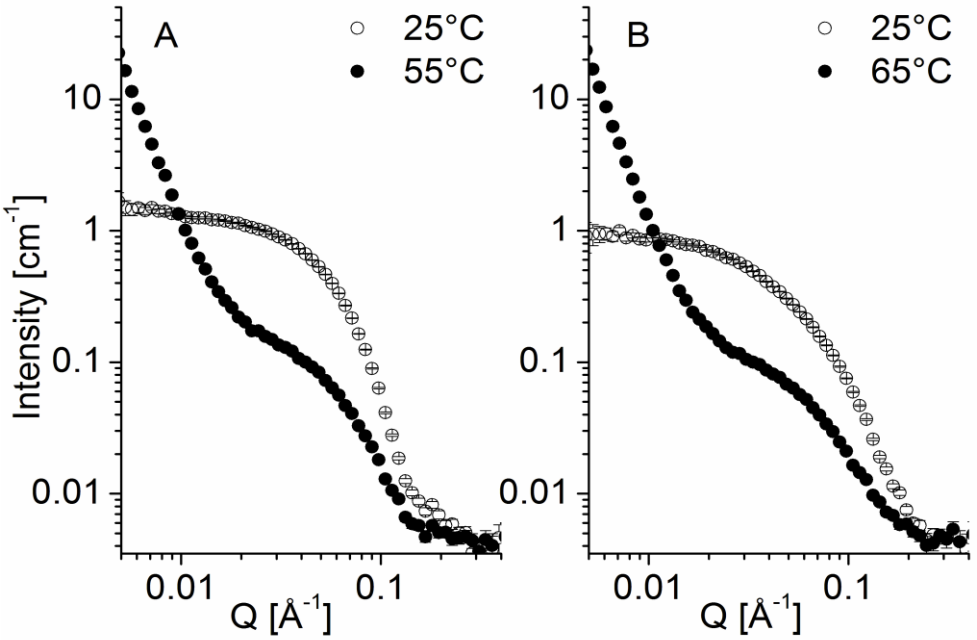

Figure 47: SANS spectra of copolymer solutions in D_2O (5 mg/mL) below and above the transition temperatures: (A) PEGMA69-*co*-FA31 and (B) PEGMA90-*co*-FA10. Errors, always smaller than the used symbols, are visible in the empty circles.

2.1.4.3 Modelling of the single-chain folding of PEGMAx-*co*-FAy

Molecular dynamic (MD) simulation were carried out to evaluate folding trajectories of amphiphilic fluorinated random copolymers, and support the single-chain folding model proposed in this work with conformational details.

Copolymer PEGMA77-*co*-FA23, that exhibited single-chain folded unimer micelles at room temperature with a D_h = 4±1 nm was selected as reference. Hydrophilic PEGMA and hydrophobic/lipophobic FA represented the two building units, HYD and LIP respectively, used to build up the sequences in the simulations.

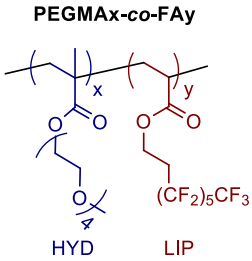

Figure 48: Building units of an amphiphilic fluorinated random copolymer. Hydrophilic PEGMA unit (HYD) and hydrophobic/lipophobic FA unit (LIP).

PEGMA77-*co*-FA23 was characterised by ^{1}H NMR to display 104 repeating units, consisting of 80 PEGMA and 24 FA repeating units. Therefore, four 104-mer sequences were generated by randomly selecting the unit with probability 80(HYD)/24(LIP). Notice that the actual HYD/LIP ratio was not necessarily equal to 80:24 in each sequence. The polymer starting structure was built up by adding building blocks one at a time, each time relaxing the structure.

A block ordered sequence was generated by creating four blocks of six LIP units equally spaced by HYD units. A hydrophilic-only polymer was also built with 104 HYD units following the same procedure as for the block copolymer.

In any simulation the initial structure was put into a rectangular box of water solvent molecules. Two structures were also solvated in $CHCl_3$. The dimensions of the box were chosen so that the edges of the box were at a minimum distance of 20Å from the polymer atoms. The solvated system was heated up to 300K for 100 ps, followed by a 200 ns of production run of the MD simulation. Computational details were reported in experimental paragraph.

The final structures for all the MD simulations in water were reported in Figure 49, where numbered items referred to random sequences, EQB to the block ordered sequence and HYD to the all hydrophilic PEGMA homopolymer. On one hand, all simulations reached a much more compact structure than the outstretched random initial structure. On the other hand, a large variety of

structures was formed. Random copolymer simulations resulted in a final structure characterised by a rod shape. In the remaining simulations, the final structure was more disk-shaped.

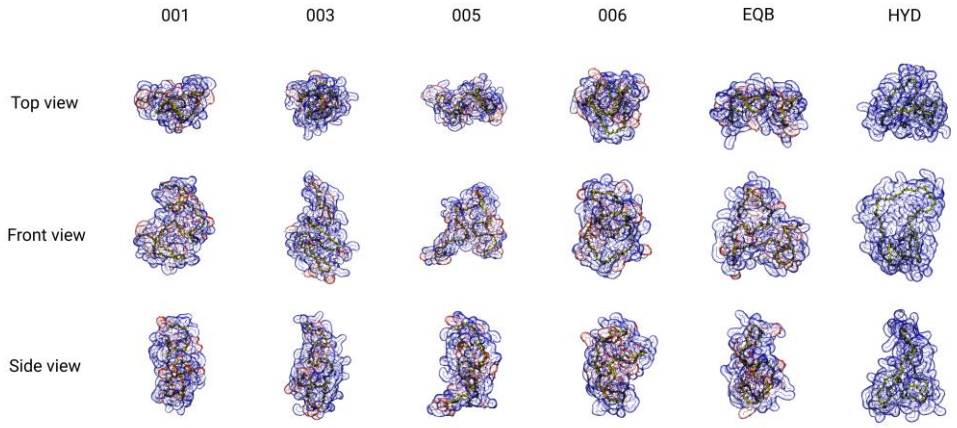

Figure 49: Final structures for the simulations in water. Structures 001 002 005 006 refer to the four random copolymers, EQB refers to the block ordered copolymer, and HYD is the all-HYD polymer. The yellow trace represents the carbon backbone; red and blue colours refer to LIP and HYD units, respectively.

The final structures from simulations for the random copolymer solvated in $CHCl_3$ were shown in Figure 50. Compared to the same structures in water, these simulations reached much more open structures, where the side chains remained exposed to the solvent, and fewer contacts were formed among units. The radius of gyration R_g along each simulation was reported in Figure 51. For all simulations in water, R_g decreased in time, meaning that the polymer was adopting a more compact shape. On the contrary, in $CHCl_3$, R_g oscillated around the initial value, decreasing only slightly in simulation 006. This means that in $CHCl_3$ the polymer does not fold, rather it adopts various random open conformations. Although the reduction of R_g along all simulations in water was present, the time evolution was different in each dynamics, due to the different polymer sequence and starting conformation. However, all simulation reached a final value of R_g around 20–25 Å.

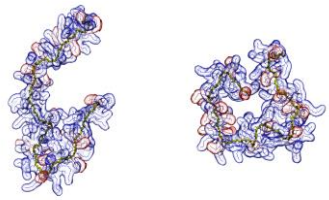

Figure 50: Final structures for the simulations in $CHCl_3$. The yellow trace represents the carbon backbone; red and blue colours refer to LIP and HYD units, respectively.

Different parameters were analysed along the folding trajectories. The gyration tensor (G) was extracted, defined as:

$$\boldsymbol{G}_{ij} = \frac{1}{N}\sum_{n=1}^{N} \boldsymbol{r}_{n,i}\boldsymbol{r}_{n,j} \qquad i,j = x,y,z \qquad \text{Eq. 10}$$

where i and j are two cartesian components, the sum runs over all the heavy atoms of the polymer, and $\mathbf{r}_n$ is the position of the n-th atom with respect to the geometric centre of the polymer. Note that the positions here were not mass-weighted. In order to describe the dimensions of the polymer, we use the radius of gyration, defined as $R_g = \sqrt{tr(\boldsymbol{G})}$.

Since the radius of gyration only gives an idea of the compactness of the macromolecule, it was useful to define additional shape descriptors from the principal gyration moments, i.e. the eigenvalues of the gyration tensor $G_X \leq G_Y \leq G_Z$, associated to the principal axes X, Y, and Z.

The asphericity A_s and acylindricity A_c are defined as:

$$A_s = G_Z - \frac{1}{2}(G_X + G_Y) \qquad \text{Eq. 11}$$

$$A_c = G_Y - G_X \qquad \text{Eq. 12}$$

These quantities are always non negative, and are both zero if the polymer has spherical symmetry. Moreover, A_c is zero if the polymer has a symmetry axis. These two descriptors can thus be used to classify the shape of the polymer, giving information complementary to R_g.

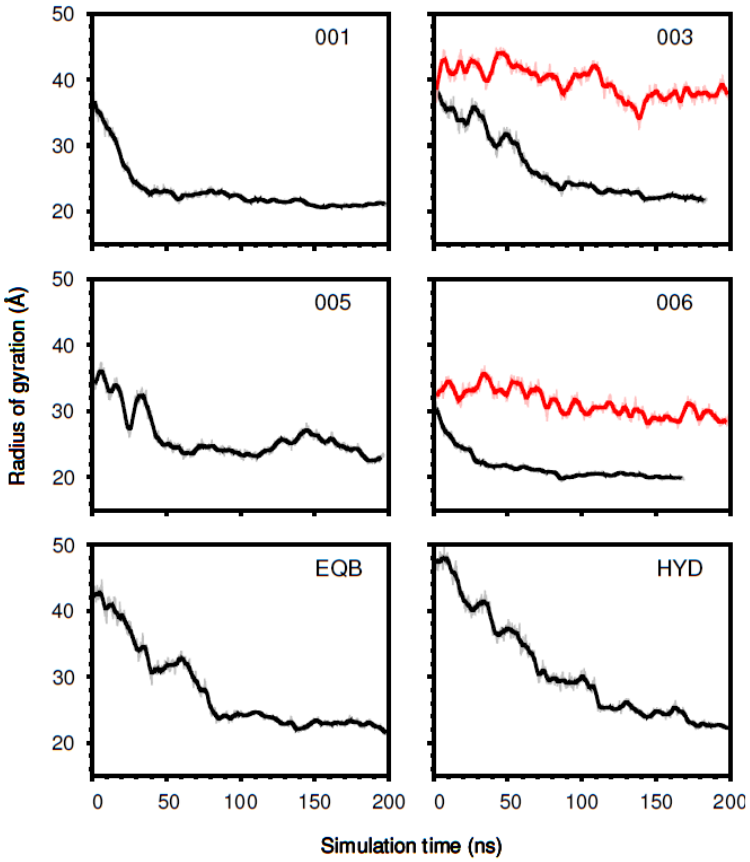

Figure 51: Radius of gyration calculated on heavy atoms along the various simulations. Black lines represent simulations in water, red lines represent simulations in $CHCl_3$. All data are smoothed with a moving average over 200 frames.

The analysis of the shape descriptors was reported in Figure 52. Similarly to what was observed in R_g analysis, for all simulation in water, the chain arrangement became more symmetric with respect to the three coordinate axes (asphericity < 4 nm^2). On the contrary, for the $CHCl_3$ simulations, the asphericity oscillates around the initial value meaning that the polymer maintains a conformation similar to the initial structure.

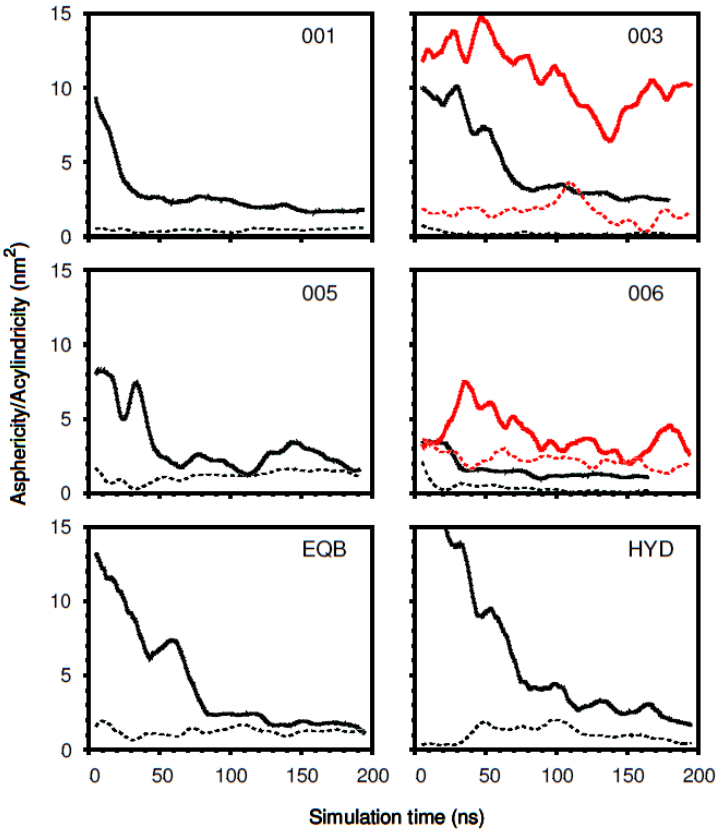

Figure 52: Shape descriptors asphericity (solid lines) and acylindricity (dashed lines). Black lines represent simulations in water, red lines represent simulations in $CHCl_3$. All data are smoothed with a moving average over 200 frames.

In order to assess the role of hydrophobic interactions, the solvent-accessible surface area (SASA)[96] of the polymer was computed using the SURF program.[97] The SASA was partitioned into contributions from HYD and LIP units ($SASA_{HYD}$ and $SASA_{LIP}$). The average contribution of one HYD or LIP unit to the total SASA was calculated as:

$$C_{HYD/LIP}\% = \frac{SASA_{HYD/LIP}}{n_{HYD/LIP}\, SASA_{Tot}} 100 \qquad \text{Eq. 13}$$

where n_{HYD} and n_{LIP} are the number of HYD and LIP residues, respectively. If the different units are equally exposed to the solvent, $C_{HYD} \simeq C_{LIP}$. On the contrary, $C_{LIP} < C_{HYD}$ means that, on average, LIP units are less exposed to the solvent.

The total solvent-accessible surface area was shown in Figure 53. A decrease in SASA indicated that the polymer structure becomes more compact, exposing less of its surface to the solvent, as a consequence of folding. For all water simulations SASA decreased in time, whereas for the two $CHCl_3$ simulations no significant changes were observed. These findings are in line with the results obtained from geometrical parameters.

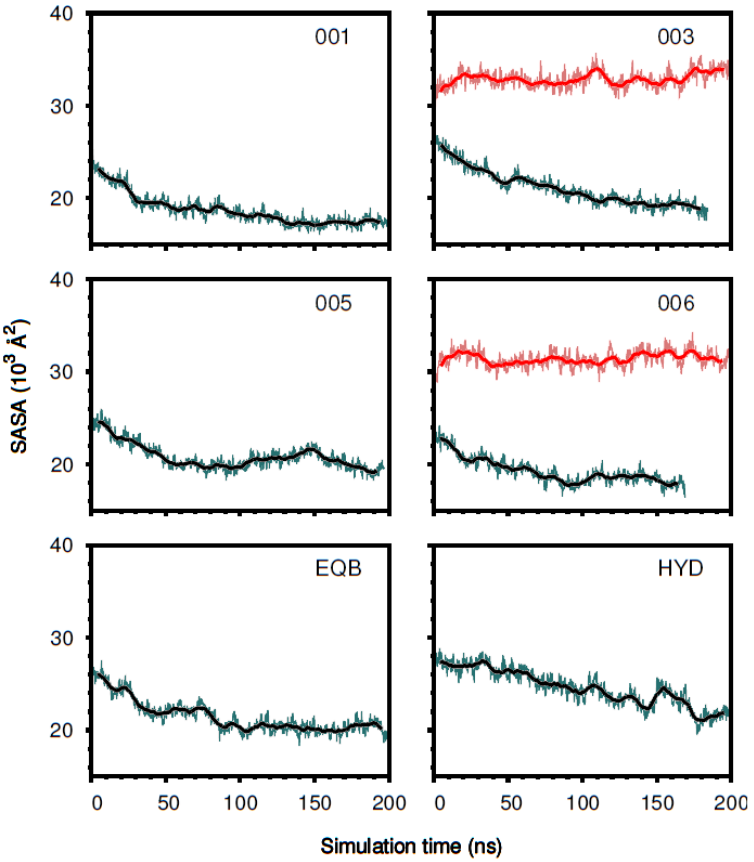

Figure 53: Solvent-accessible surface area along the various simulations. Black lines represent simulations in water, red lines represent simulations in $CHCl_3$. All data are smoothed with a moving average over 200 frames. Thin lines represent the original non-averaged values.

In order to understand whether the two unit types were equally exposed to solvent, the SASA contribution analysis ($C_{HYD/LIP}$%) as a function of time were

reported in Figure 54. In all simulations the LIP contribution was always smaller than the HYD contribution because LIP units were shorter than HYD units, containing less atoms, and thus contributed less to the total surface. However, the HYD and LIP contributions were not constant along the trajectories simulated in water, rather they slightly changed with an appreciable decrease in the LIP contribution. This observation suggested that LIP units became more buried in the internal region of the polymer, as it folded along the trajectory. Interestingly, in the two $CHCl_3$ simulations SASA contribution of HYD and LIP units did not change, indicating that both units were equally exposed to the solvent for all the trajectory.

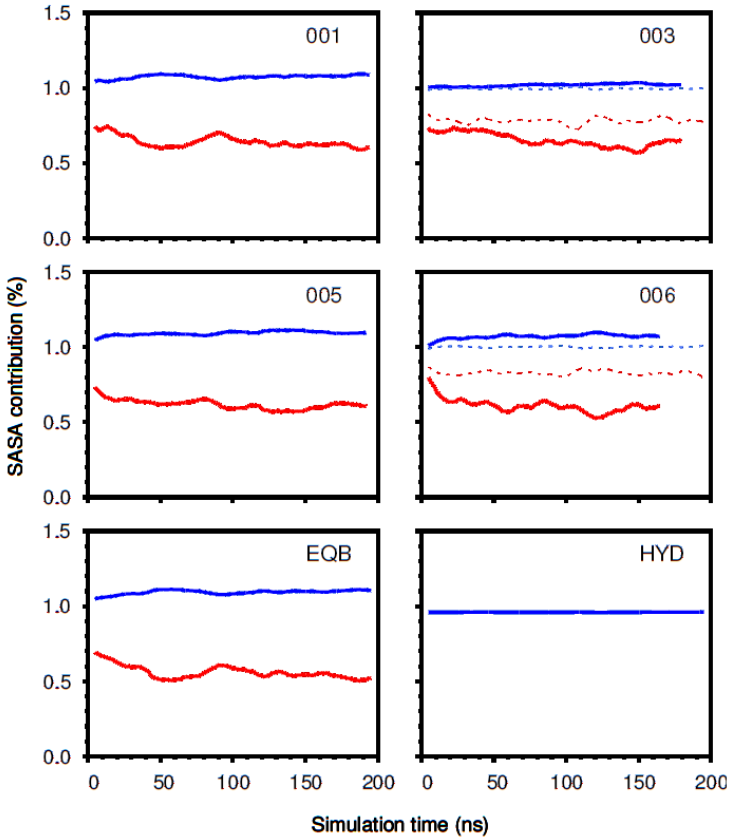

Figure 54: Average contribution (%) to the SASA for each HYD unit (blue lines) and for each LIP unit (red lines). Solid lines represent simulations in water, dashed lines refer to simulations in $CHCl_3$.

2.1.4.4 Dynamic light scattering of PEGMAx-*co*-SiMAy solutions

Dynamic light scattering experiments of amphiphilic poly(ethylene glycol) and siloxane methacrylate based random copolymers were carried out to evaluate their ability to spontaneously single-chain fold in a suitable solvent, like water, forming unimer micelles driven by the association of hydrophobic siloxane side chains.

At room temperature, 5 mg/ml water solution of PEGMA85-*co*-SiMA15 and PEGMA95-*co*-SiMA5 copolymers showed bimodal intensity size distribution of scatters, characterised by a lower hydrodynamic diameter (D_h^1) of ≈ 8 nm (Table 14). This result is consistent with the formation of folded macromolecular chains. Traces of aggregates of larger size (D_h^2 210 – 290 nm) were detected. These could be ascribed to multi-chain aggregation, and in case of polymer PEGMA95-*co*-SiMA5 this latter population of collective aggregates was significant even in volume size distributions (Figure 55), that better represent the relative amount of different populations in a multimodal size distribution. In the same way, J(PEGMA94-*co*-SiMA6) showed a bimodal intensity size distribution of D_h^1 ≈ 10 nm unimer and D_h^2 ≈ 580 nm collective aggregates, suggesting that self-assembly in unimer micelles was not depressed by the cyanovinyl julolidine residue. The second population of multichain aggregates, in this case, was negligible in volume size distributions. Thus, even in amphiphilic siloxane based random copolymers the intramolecular hydrophobic interactions were favoured over supramolecular aggregation. However, the coexistence of the two forms was possible for PEGMA95-*co*-SiMA5.

Table 14: Average hydrodynamic diameters of aqueous solution of the amphiphilic/siloxane copolymers, from DLS intensity size distributions at 5 mg/ml.

Copolymer	***D_h^{1a} (nm)***	***D_h^{2b} (nm)***
PEGMA95-co-SiMA5	8±3	210±20
PEGMA85-co-SiMA15	8±3	290±40
J(PEGMA96-co-SiMA6)	10±3	580±90

a Population of smaller scatters in the bimodal intensity distribution.
b Population of larger scatters in the bimodal intensity distribution.

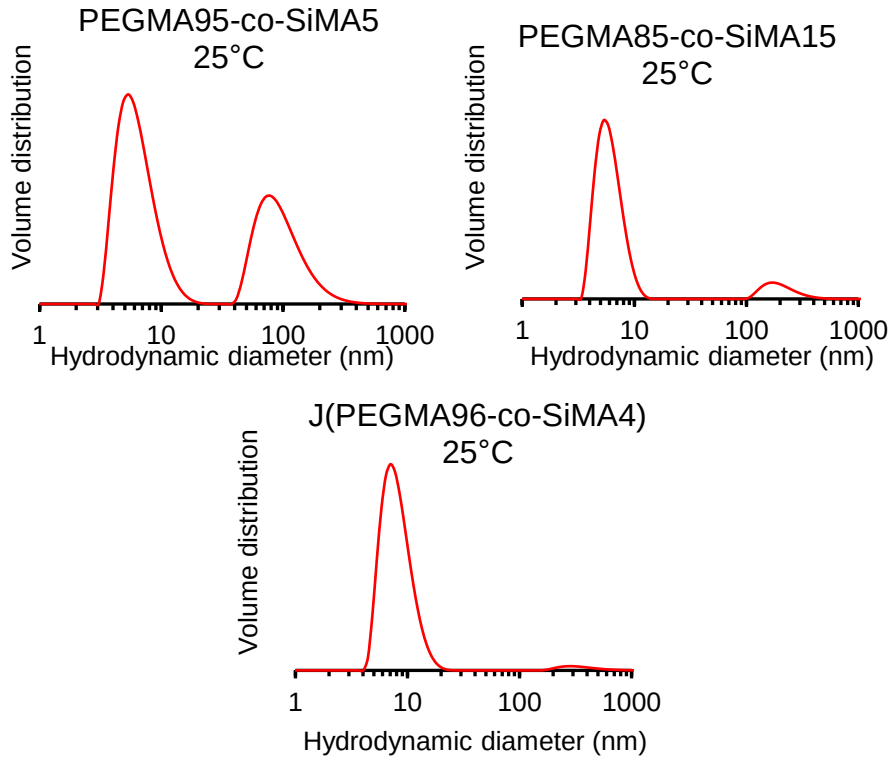

Figure 55: DLS volume size distributions for PEGMAx-*co*-SiMAy and J(PEGMA94-*co*-SiMA6) 5 mg/ml solutions in water at room temperature.

All amphiphilic siloxane based copolymers proved to be thermoresponsive in water. DLS measurements at variable temperature proved that above a critical temperature (T_c), the smaller scatters (8-10 nm, stable at room temperature) collapsed in larger micrometric aggregates (Table 15), with monomodal narrow intensity size and volume distributions (Figure 56). DLS measurements, while cooling down the samples, confirmed that this phenomenon is reversible with almost no temperature hysteresis. These two different states could be easily distinguished by naked eyes (Figure 57), for the solutions at room temperature were perfectly clear, while above T_c they appeared cloudy, due to the larger scatters.

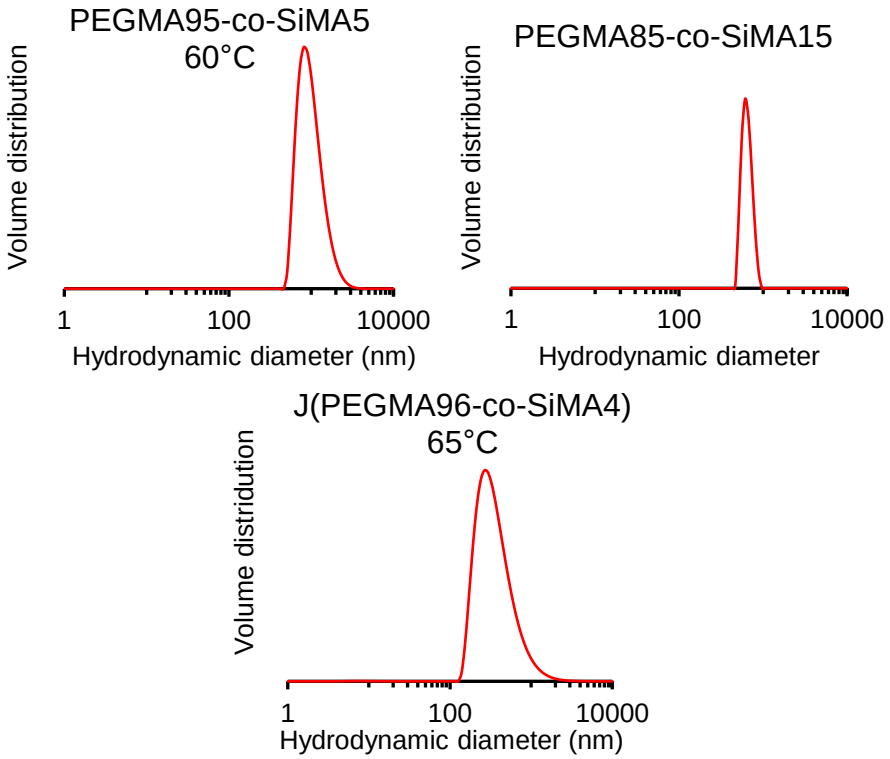

Figure 56: DLS volume size distributions for PEGMAx-*co*-SiMAy and J(PEGMA94-*co*-SiMA6) 5 mg/ml solutions in water at $T>T_c$.

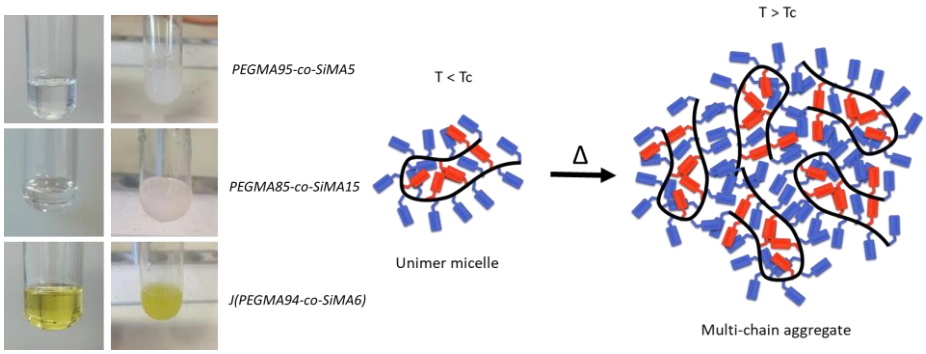

Figure 57: Photograph of clear solutions (T=25°C) of amphiphilic/siloxane random copolymers (left) and corresponding cloudy dispersions at $T>T_c$ (right), with a schematic representation of the aggregation phenomenon hypothesised.

Interestingly, as already observed in experiments on amphiphilic/fluorinated random copolymers, PEGMAx-*co*-SiMAy copolymers showed a similar thermoresponsive behaviour with a T_c value influenced by copolymer composition. Starting from the reference value of LCST of PEGMA homopolymer and increasing the hydrophobic character of the copolymer, the T_c value decreased down to 49 °C in copolymer with 15% mol SiMA (Table 15).

Table 15: Critical Temperature (LCST) for amphiphilic/siloxane random copolymers in water.

Copolymer	T_c [a] (°C)	D_h [b] (nm)
pPEGMA[c]	*66*	*nd*
PEGMA95-co-SiMA5	54	1400±60
PEGMA85-co-SiMA15	50	700±30
J(PEGMA94-co-SiMA6)	60	700±30

a Critical temperature recorded in DLS experiment.
b Average hydrodynamic diameter above T_c measured by DLS at 5 mg/ml.
c Literature value from ref.[95]

DLS measurement at room temperature of solutions of amphiphilic/siloxane random copolymers PEGMAx-*co*-SiMAy (5 mg/ml) solution in organic solvents (chloroform, tetrahydrofuran and acetone) exhibited negligible light scattering intensities, and no self-assembled nanostructures were detected. Copolymer J(PEGMA96-*co*-SiMA4) showed a certain tendency to self-assemble in $CHCl_3$, and multimodal distributions of irregular particles were detected. J(PEGMA96-*co*-SiMA4), other than PEGMAx-*co*-SiMAy copolymers, was characterised by a higher molecular weight, a broader molecular weight distribution and a less defined macromolecular structure. This could lead to the different self-assembly behaviour in chloroform, that is a solvent less affine to PEG than THF, where in fact no self-assembly was detected.

2.1.5 Absorption/emission spectroscopic properties

In the following paragraphs, absorption and emission spectroscopic properties coming from fluorescent dyes (covalently bonded to the copolymers or reversibly, physically interacting with the copolymers) were investigated. This allowed to better understand the single-chain folding process and self-assembly of copolymers of this work, as well as their actual promising potential as building block for more complex functional materials.

2.1.5.1 PEGMA74-*co*-FA25-*co*-JCBF1

In depth characterisation of JCBF fluorescent monomer was recently published.[49] Briefly, UV-vis absorption of JCBF in chloroform showed a characteristic absorption band at 410 nm, common to cyanovinyl julolidine derivatives, and a second absorption at about 290 nm, from $\pi \rightarrow \pi^*$ electronic transition in biphenyl moiety. Lambert-Beer law was followed, with ε = 21500 $M^{-1}cm^{-1}$. Emission fluorescence maximum is centred at 500 nm (λ_{exc} = 410 nm). Fluorescence quantum yield in chloroform ($\Phi = 2.5 \times 10^{-3}$) was negligible, according to the FMR assumption that the molecular internal rotation of the molecule, in low viscosity media, allows the TICT state to dissipate energy non radiatively. JCBF methanol/glycerol solutions with increasing viscosity, ensued the typical FMR Förster-Hoffmann behaviour, with a high viscosity sensitivity parameter (x = 0.56). Thus, the hindered rotation promoted the emission from the LE and, consistently increased the quantum yield.

UV-vis absorption spectra in chloroform solution of PEGMA74-*co*-FA25-*co*-JCBF1 (Figure 58) presented the same feature of the free fluorescent monomer. Absorbance maximum is at 405 nm (ε = 22300 $M^{-1}cm^{-1}$, from linear fitting with R^2 = 0.9996)

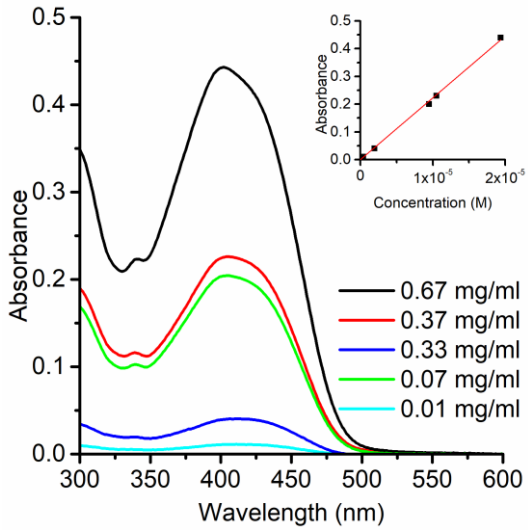

Figure 58: UV-vis absorption spectra of PEGMA74-*co*-FA25-*co*-JCBF1 in chloroform at various polymer concentrations. In the inset: Lambert-Beer plot (molar concentration referred to repeating units JCBF).

Emission spectra in chloroform solutions of PEGMA74-*co*-FA25-*co*-JCBF1 copolymer showed a weak emission at 500 nm, when λ_{exc} = 405 nm and calculated quantum yield $\Phi = 4.27 \times 10^{-3}$, slightly increased with respect to the monomeric form of the dye, probably due to the steric hindrance of the macromolecular chain covalently bonded to the FMR.

Fluorescence emission spectra in water, chloroform and hexafluorobenzene (HFB) were compared (Figure 59 e Table 16). Being the single-chain folding and self-assembly driven by the affinity of solvent with different components of amphiphilic copolymers, a different response of the fluorescent probe was expected.

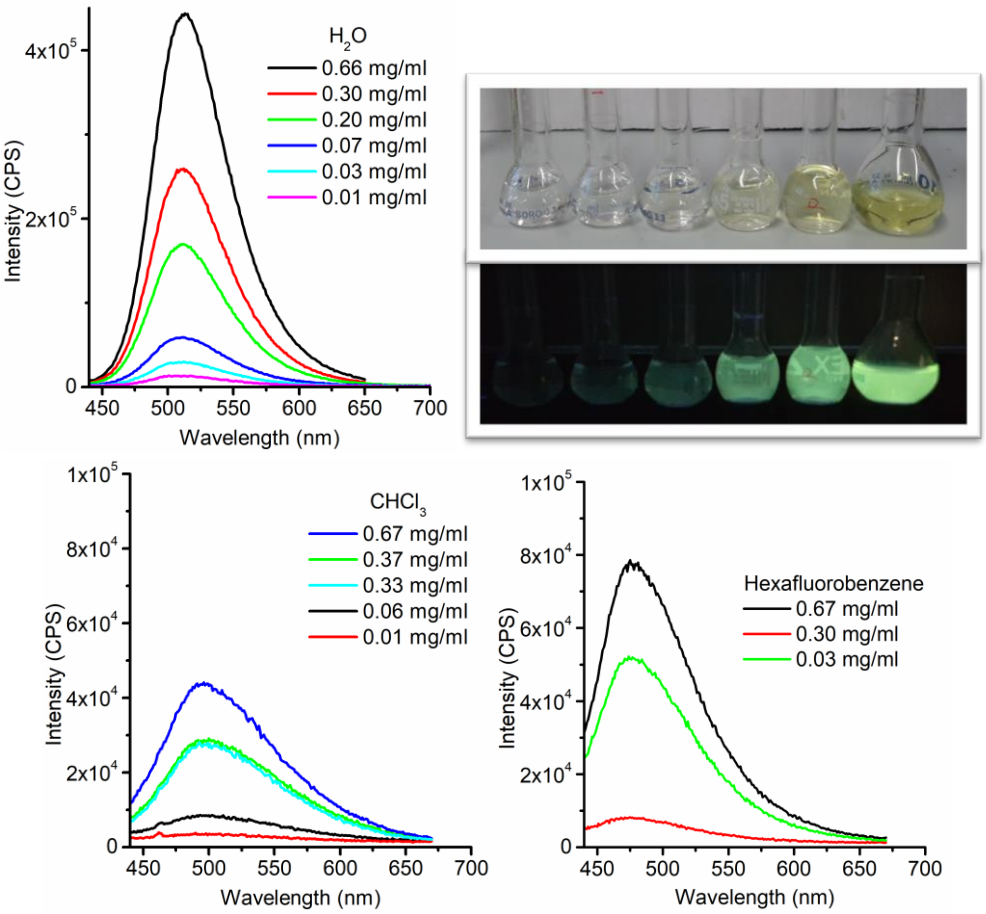

Figure 59: Fluorescence emission spectra of PEGMA74-*co*-FA25-*co*-JCBF1 in water, chloroform and hexafluorobenzene at different concentrations. Photographs show water solutions under natural light (above) and 354 nm UV lamp (bottom).

Fluorescence emission intensities, and the respective quantum yields, in water were one order of magnitude higher than in chloroform. This result was coherent with the hypothesis of the formation, in water, of single-chain folded unimer micelles, to minimise the contact of the extremely hydrophobic fluorinated moieties with water. In these nanostructures, the FRM was probably segregated in hydrophobic compartments, with hindered mobility and consequently augmented fluorescence emission. Similar to chloroform, hexafluorobenzene was a good solvent for both amphiphilic components of the copolymer, and intensity emission and fluorescence quantum yield five times

lower than in water, consistent with the unfolded state of the copolymer. Higher viscosity (1.2 $mPas^{-1}$) of hexafluorobenzene with respect to chloroform (0.5 $mPas^{-1}$) was responsible for the different emission in these two non-selective solvents.

Table 16: Physical-chemical properties of analysed solutions; intensity emission maximum (λ_{exc} = 405 nm, λ_{em} = 500 nm) and calculated fluorescence quantum yields.

Solvent	***Viscosity[a] (mPa s)***	***Copolymer[b] (g/l)***	***JCBF[c] (M)***	***Em. max. (nm)***	***Φ[d]***
$CHCl_3$	0.5	0.67	$1.94x10^{-5}$	44000	$4.27x10^{-3}$
		0.33	$9.49 x10^{-6}$	28000	$4.49x10^{-3}$
		0.06	$1.94 x10^{-6}$	8600	$5.62x10^{-3}$
HFB	1.2	0.67	$1.92 x10^{-5}$	78600	$7.40x10^{-3}$
		0.30	$8.72x10^{-6}$	52200	$8.12x10^{-3}$
		0.03	$8.72 x10^{-7}$	8200	$8.80x10^{-3}$
Water	1.0	0.66	$1.93 x10^{-5}$	443600	$4.00x10^{-2}$
		0.30	$8.72 x10^{-6}$	259000	$4.60x10^{-2}$
		0.03	$8.72 x10^{-7}$	29200	$4.72x10^{-2}$

a Solvent viscosity at 20°C.
b PEGMA74-*co*-FA25-*co*-JCBF1 copolymer concentration in solution.
c JCBF absolute molar concentration in solution.
d See Experimental paragraph for calculation details.

Then, the influence of temperature on amphiphilic fluorinated random copolymers self-assembly in water solution was considered. A 0.5 mg/ml solution of PEGMA74-*co*-FA25-*co*-JCBF1 in water was repeatedly analysed, varying the temperature from 25°C to 65°C. Fluorescence emission spectra were recorded every 5°C step during heating and cooling in this interval.

In Figure 60 it was clear that fluorescence emission decreased at higher temperatures. With increasing temperature, the solution viscosity was expected to decrease, whereas collisional quenching of fluorescence intensify was foreseen to both concurring in fluorescence emission decrease.

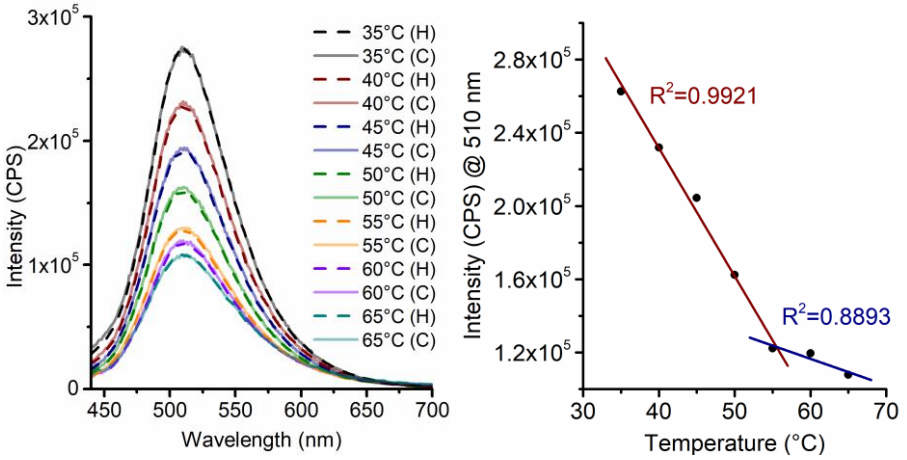

Figure 60: Fluorescence emission spectra of PEGMA74-*co*-FA25-*co*-JCBF1 in water (0.5 mg/ml) as function of temperature during heating (H) and cooling (C)(left). Intensity maximum variation (at 510 nm) as function of temperature (right).

The trend was not linear in temperature, and above 55°C showed an abrupt change in slope (Figure 60, right). DLS experiments previously suggested that above this transition temperature the unimer micelles collapsed in larger multi-chain aggregates. Larger multi-chain aggregates, were formed since hydrogen bonds between water and hydrophilic oxyethylene side chains were broken. Thus, hypothetically, the FMRs were segregated in bigger, less solvated structures and the effect of solvent viscosity was affecting less the fluorophore mobility. In the same way, the probability of collisional quenching was reduced even at high temperature, thanks to the good shielding provided by the large aggregates. In the end, the fluorescence emission displayed only a little drop between 55 and 65°C.

Fluorescence emission was completely recovered on cooling down the sample, as demonstrated by perfect superimposition of fluorescence spectra in Figure 60. Thus, a reversible transition from unimer micelles to multi-chain aggregates took place.

2.1.5.2 PEGMAx-*co*-FAy with ethidium bromide

Ethidium bromide (EtBr, Figure 61) is a fluorescent dye and common intercalating agent for nucleic acids. It is widely used in molecular biology, for example in gel electrophoresis. EtBr significantly enhances its fluorescence emission when it is intercalated in DNA double helices.

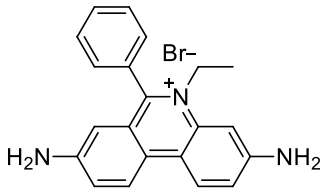

Figure 61: Chemical structure of ethidium bromide (EtBr).

On the contrary, free EtBr molecules in water solution can dissipate excitation energy via non-radiative pathways, quenched by polar mobile solvent molecules. These interactions with the solvent are inhibited when EtBr is confined within DNA chains, so that relaxation is only possible through photon emission.

Experiments of fluorescence emission spectroscopy of solutions of PEGMA77-*co*-FA23 with ethidium bromide were conducted. If the self-assembled nanostructures from amphiphilic/fluorous copolymers were able to interact and host a molecule of EtBr, it would be possible to detect an increase in fluorescence emission of EtBr. The effect of temperature would also be considered.

In Table 17 were reported the details relative to the solutions analysed. The reference solution, containing EtBr only, (λ_{exc} = 520 nm, corresponding to the maximum absorbance of EtBr) at 25°C was compared to the emission spectra of copolymer solutions (Figure 62). An increase in the fluorescence emission at 607 nm was observed. Probably, EtBr was successfully enclosed in the unimer micelles formed by the folded copolymer chains. In this way, the interaction with solvent molecules was shielded, and fluorescence emission was significantly enhanced.

Table 17: Aqueous solutions of amphiphilic/fluorous random copolymer and EtBr, and their critical transition temperatures.

Solution	*PEGMA77-co-FA23 (mg/ml)*	*EtBr(mg/ml)*	T_c (°C)
Reference	--	0.03	--
Sol 1	0.10	0.03	74
Sol 2	0.20	0.03	66
Sol 3	0.30	0.03	60
Sol 4	0.63	0.03	55
Sol 5	2.34	0.03	53
Sol 6	3.13	0.03	52
Sol 7	5.01	0.03	52
Sol 8	10.02	0.03	51
Sol 9	20.04	0.03	52
Sol 10	32.85	0.03	51

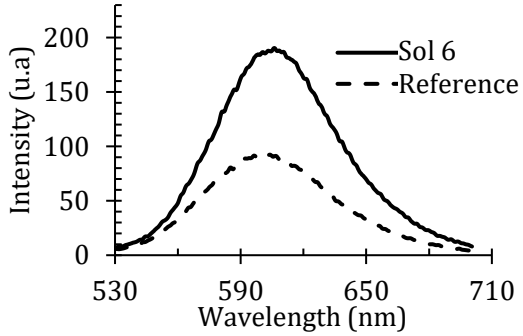

Figure 62: Fluorescence emission spectra in water of a reference solution of EtBr 0.03 mg/ml and a PEGMA77-co-FA23 3.13 mg/ml solution containing 0.03 mg/ml EtBr (solution 6).

Considering the inherent thermoresponsive character of amphiphilic/fluorous copolymers in water, the temperature dependence of the fluorescence emission of the copolymer-EtBr system was examined.

As an example, for solution 6, fluorescence intensity at 607 nm significantly decreased going from room temperature to 65°C (Figure 63, left). On the other hand, an increase in scattering (at 530 nm) due to aggregates forming at higher temperatures was evident. These two opposite trends showed a discontinuity at 52°C (Figure 63, right). Above 52°C single-chain folded macromolecules started to aggregate, because hydrogen bonds between water and hydrophilic

oxyethylene side chains were broken, consistent with the observations at DLS. Collapsed multichain aggregates released EtBr as showed by its emission reduction.

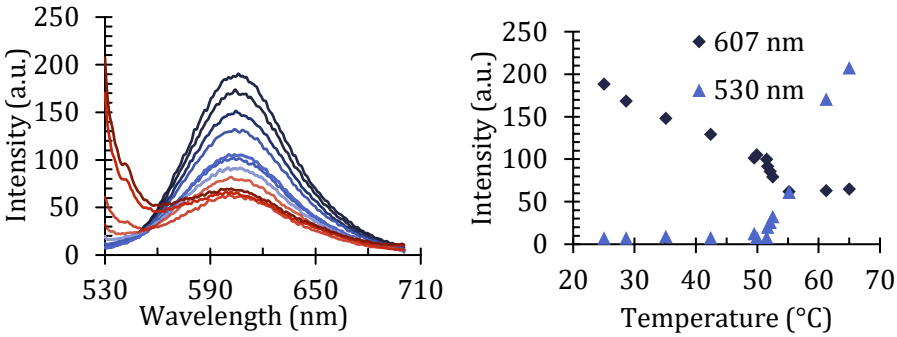

Figure 63: Fluorescence emission spectra in water (left) of a PEGMA77-*co*-FA23 3.13 mg/ml solution containing 0.03 mg/ml EtBr at different temperatures from 25°C to 65°C (from blue to red, respectively). Fluorescence emission intensity maxima at 607 nm and scattering intensity at 530 nm (right) vs temperature.

Solutions with different concentrations of PEGMA77-*co*-FA23 exhibited similar behaviour, but with different transition temperatures (Table 17 and Figure 64). This result showed that, for diluted solutions, the aggregation of unimer micelles into larger aggregates and the release of EtBr was triggered at higher temperatures (74 – 55 °C). Above 2.34 mg/ml copolymer concentration, the multichain aggregation and EtBr release was triggered at 53 – 51°C, up to significantly higher copolymer concentration (32.85 mg/ml). This result is consistent with observations made in DLS paragraph (2.1.4.1) for PEGMA69-*co*-FA31 water solution. In the concentration range of 0.5 – 5 mg/ml used for DLS the transition temperatures were sufficiently near the expected plateau region, thus the recorded variation was about 1°C only.

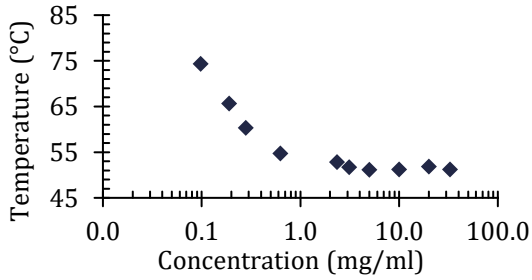

Figure 64: Critical temperature T_c vs PEGMA77-*co*-FA23 concentration.

2.1.5.3 UV-absorption and fluorescence emission of JBr

Optical properties of julolidine based fluorescent molecular rotor JBr were first evaluated in chloroform solution. UV-vis absorption spectrum and fluorescence emission spectrum are compared in Figure 65, left. The absorption band showed an absorbance maximum at 454 nm while the emission had a maximum intensity at 489 nm. This resulted in a Stokes shift of 35 nm, similar to other cyanovinyl julolidine compounds.[47] The absorbance vs. molar concentration plot follow the Lambert-Beer law giving a molar extinction coefficient $\varepsilon = 52700$ $M^{-1}cm^{-1}$. This result was obtained from the linear regression of the absorbance vs. molar concentration plot (R^2=0.997) for six solutions with known concentration between $5x10^{-7}$M and $1x10^{-5}$M (Figure 65, right).

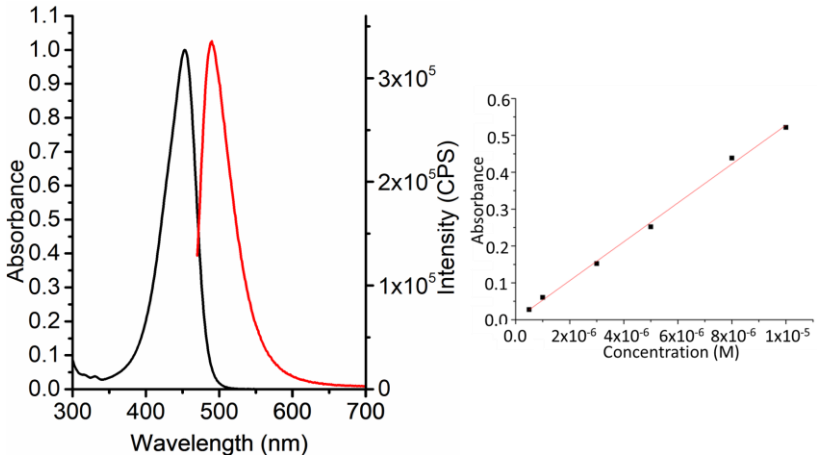

Figure 65: UV-vis absorption spectrum (red) and emission spectrum (black) (λ_{exc} = 454 nm; JBr $3x10^{-5}$M in $CHCl_3$). UV absorbance maxima vs concentration of JBr (right).

Several methanol/glycerol mixtures with a constant concentration in JBr ($1x10^{-5}$ M) were analysed (Figure 66, Table 18). Methanol and glycerol have a large difference in viscosity (0.6 mPa s and 934 mPa s at 25°C respectively). By changing the volume fraction of glycerol in the mixture, it was possible to evaluate the ability of the JBr molecules to react to variations of viscosity of the environment, in a wide range. UV-vis absorption spectra and emission spectra showed a bathochromic shift of 15 nm and 10 nm respectively, with increasing

glycerol content in the solvent mixture. This phenomenon could be ascribed to the increase in the dielectric constant, from 33 for pure methanol to 41.4 for the most glycerol enriched mixture.

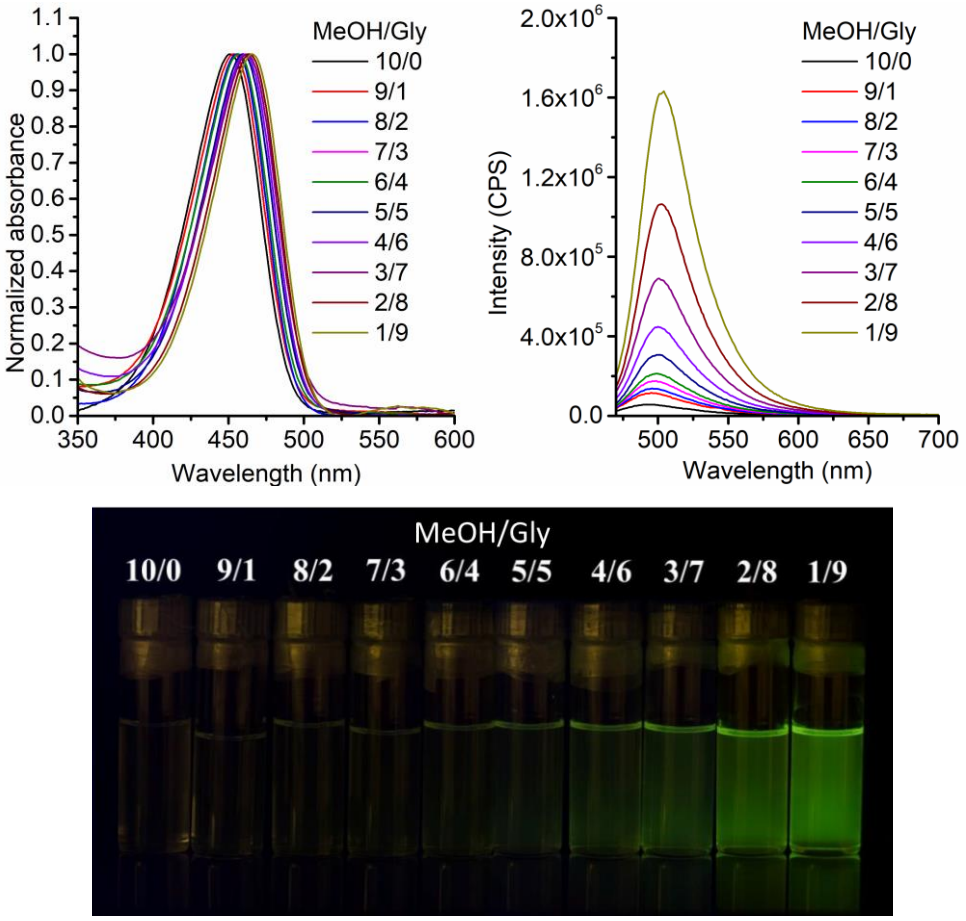

Figure 66: UV-vis absorption spectra of JBr 1x10^{-5}M in methanol/glycerol mixtures (left); fluorescence emission spectra (λ_{exc} = 454 nm) in methanol/glycerol mixtures (right); photograph of of JBr 1x10^{-5}M in methanol/glycerol mixtures irradiated with Dark Reader 46B transilluminator (bottom).

Fluorescence intensity, and consistently fluorescence quantum yields, increased with increasing viscosity of the solvent mixture, in agreement with previous data for julolidine derivatives.[47,48] For this class of aggregation induced emission (AIE) fluorophores, in viscous media, the formation of a twisted intramolecular

charge transfer (TICT) state is inhibited, and absorbed energy cannot be dissipated through non-radiative pathways. Thus, deexcitation from the locally excited state (LE) essentially happened via radiation emission, with increased quantum yields around one order of magnitude from 1.46×10^{-3} to 2.35×10^{-2} (Table 18).

Table 18: Physical-chemical characterisation and spectroscopic properties of JBr in methanol/glycerol mixtures.

MeOH/Gly (V/V)	***Abs. max. (nm)***	***Em. max. (nm)***	***Stokes shift (nm)***	***Refractive index[a]***	***Dielectric constant[b]***	***Viscosity[c] (mPa s)***	***Φ[d]***
100/1	451	492	41	1.3288	33.0	0.6	1.46×10^{-3}
90/10	453	495	42	1.3431	34.4	1.8	1.52×10^{-3}
80/20	455	496	41	1.3574	35.6	4.8	2.04×10^{-3}
70/30	457	497	40	1.3718	36.7	7.7	2.30×10^{-3}
60/40	457	498	41	1.3861	37.6	13.0	2.77×10^{-3}
50/50	460	499	39	1.4004	38.6	28.0	3.89×10^{-3}
40/60	461	500	39	1.4147	39.3	58.0	5.67×10^{-3}
30/70	462	501	39	1.4290	40.1	130.0	9.62×10^{-3}
20/80	464	502	38	1.4434	40.8	250.0	1.42×10^{-2}
10/90	466	503	37	1.4577	41.4	630.0	2.35×10^{-2}

a Calculated from Arago-Biot rule: $n_{mix} = f_{vol1} n_1 + f_{vol2} n_2$.
b Calculated from additive rule: $\varepsilon_{mix} = f_{vol1} \varepsilon_1 + f_{vol2} \varepsilon_2$.
c Calculated from Grumberg-Nissan rule: $\eta_{mix} = f_{vol1} \eta_1 + f_{vol2} \eta_2$.
d See Experimental paragraph for calculation details.

As expected, JBr solutions ensued the typical Förster-Hoffmann behaviour,[39] that relates the (double logarithmic) quantum yield Φ with viscosity η

$$\log(\phi) = C + x \log(\eta) \qquad \text{Eq. 2}$$

where C and x are constants. The x parameter, defined as the viscosity sensitivity of the FMR, was found to be 0.48, which is comparable to values reported for similar systems, thus making JBr suitable as environmental microviscosity probe.

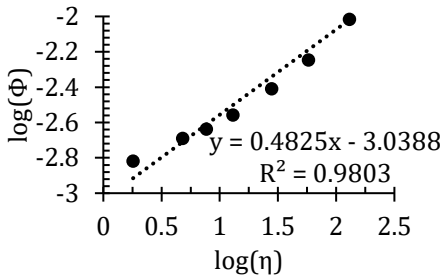

Figure 67: Förster-Hoffmann relationship of $1x10^{-5}$ M JBr solutions in methanol/glycerol mixtures with different glycerol volume contents.

2.1.5.4 J(PEGMAx-*co*-SiMAy)

Taking advantage of the fluorescent probe introduced in the PEGMAx-*co*-SiMAy system, by functionalisation of the ATRP initiator (JBr), self-assembly in water of the copolymer J(PEGMA94-*co*-SiMA6) was studied. Fluorescence emission spectroscopy provided an insight into the single-chain folding, as already developed for amphiphilic/fluorinated random copolymer PEGMA74-*co*-FA25-*co*-JCBF1.

The julolidine moiety acted like a fluorescent molecular rotor resulting in a high quantum yield of $2.35x10^{-2}$, while molecularly dissolved in an environment with 630.0 mPa s of viscosity. Once it was covalently inserted into the amphiphilic/siloxane copolymer, and allowed to self-assemble in water, fluorescence quantum yield increased even more, up to 3.60 $x10^{-2}$ for the copolymer solution containing 9.97 $x10^{-6}$ M julolidine residue.

In this case, the drastic reduction in rotor mobility was related to the particular single-chain folded nanostructure, adopted by the macromolecule in water. When the hydrophobic fluorophore, was confined in hydrophobic/siloxane compartments of unimer micelles, its molecular internal rotation was hampered, and relaxation from LE state occurred through photon emission.

In Figure 68 were compared fluorescence emission spectra of J(PEGMA94-*co*-SiMA6) in water, chloroform, tetrahydrofuran and acetone.

The highest intensity of fluorescence emission was obtained in water solutions, that being a highly selective solvent represented the ideal environment for single-chain folding and self-assembly. Other organic solvents showed a lower

emission, due to the better mobility of the FMR in the open, well-solvated conformation of the macromolecular chain in good solvents. In chloroform was observed an unexpectedly strong emission (Φ = 5.95x10^{-3}, still one order of magnitude lower than in water). This was related to the self-assembly tendency, noted by DLS in chloroform, for this particular copolymer, characterised by a higher molecular weight and broader molecular weight distribution than the other PEGMAx-*co*-SiMAy copolymers.

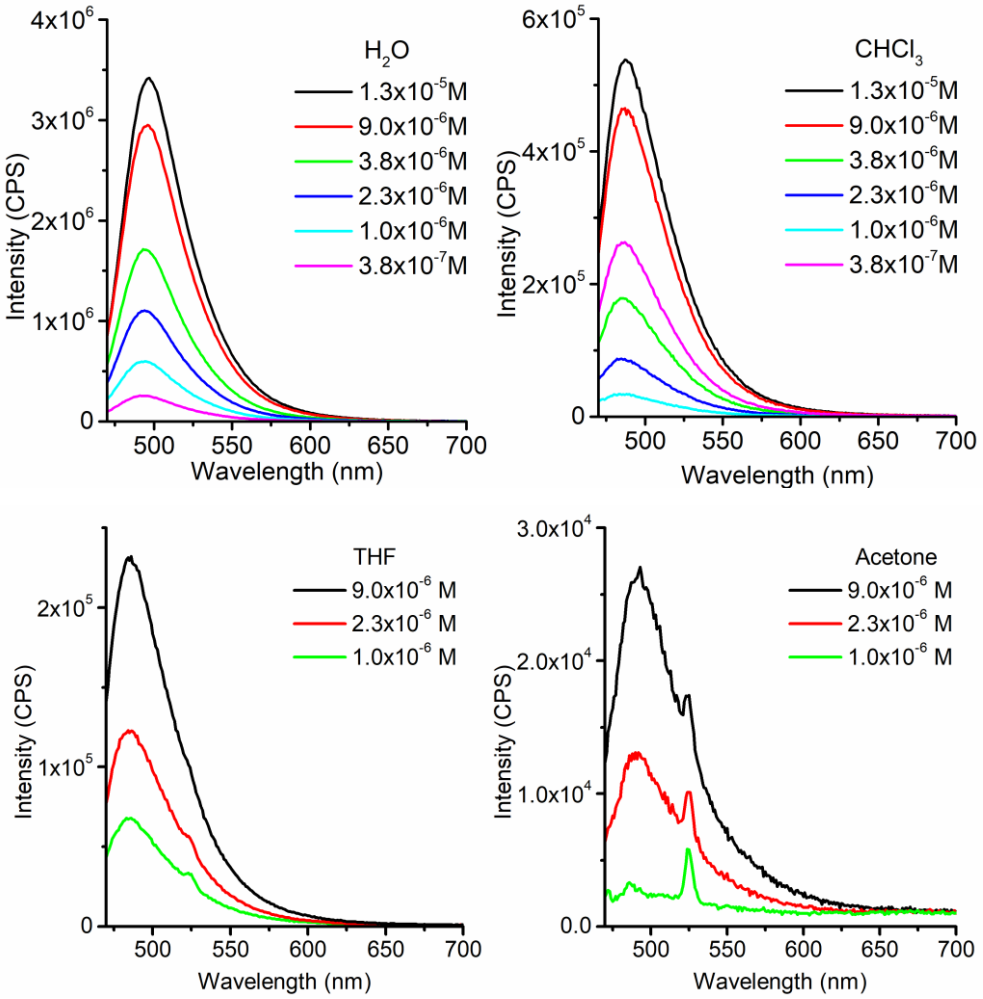

Figure 68: Fluorescence emission spectra (λ_{exc} = 454 nm) of J(PEGMA94-*co*-SiMA6) solutions at different molar concentrations of julolidine residue, in water, chloroform, tetrahydrofuran and acetone.

Fluorescence spectra of J(PEGMA94-co-SiMA6) solutions in water at different temperatures (Figure 69) confirmed the existence of a critical aggregation temperature of the system (T_c = 55°C), similar to the transition detected by dynamic light scattering experiments. Fluorescence intensity of the copolymer solution decreased linearly with temperature, due to the reduction of viscosity and higher mobility of the unimer micelle, until T_c was reached. Then, multichain micro-aggregates were formed and fluorescence emission intensity stabilised to an almost constant, much lower value. The transition was reversible in temperature.

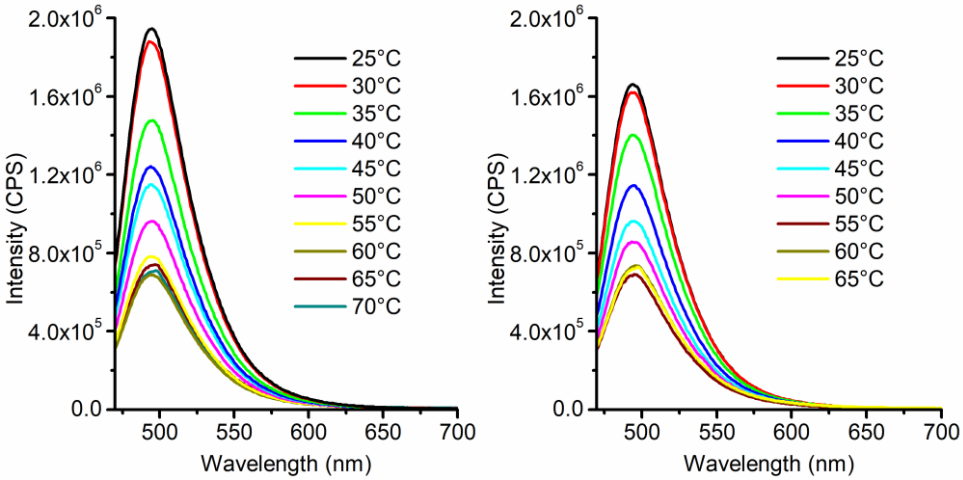

Figure 69: Fluorescence emission spectra (λ_{exc} = 454 nm) of J(PEGMA94-coSiMA6) solutions 1.7x10^{-5} M in julolidine residue, on heating (H, left) and cooling (C,right). The legend reported the temperature in °C.

2.1.6 Surface properties

2.1.6.1 Wettability and surface free energy

Water contact angles θ_w and *n*-hexadecane contact angles θ_h were measured in static conditions, to evaluate hydrophobicity (θ_w > 90°) and lipophobicity (θ_h > 60°) of film surfaces of amphiphilic/fluorinated copolymers.

Chloroform solution of 3% wt/vol copolymer were spin-coated to obtain homogenous thin films (thickness lower than 500 nm). Films were allowed to dry overnight at room temperature, before testing.

As expected, copolymers containing a high content of hydrophilic poly(ethylene glycol) were actually easily dispersible in water. Consequently, water contact angles of their films were not stable after the deposition of the droplets, and decayed to a minimum value of about 16° in less than a minute (as in the examples of Figure 70). In these conditions, it was not possible to calculate an exact value of surface tension, that could be estimated around 70 mN/m, similar to water surface tension, resulting in almost complete wettability.

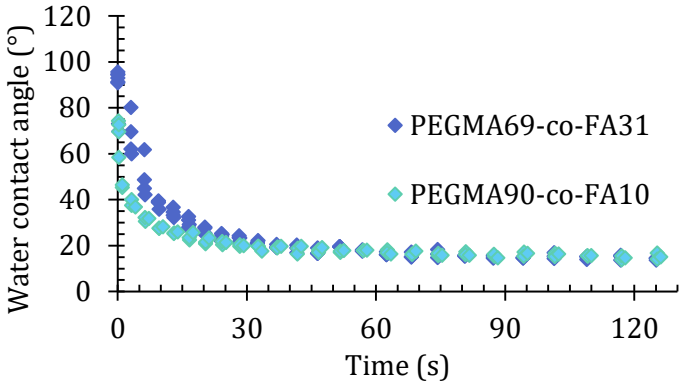

Figure 70: Water contact angle on PEGMAx-*co*-FAy films after deposition of the droplet.

Then, copolymer films were subjected to a thermal treatment of 12 hours at 120°C. The thermal annealing should favour segregation and migration of perfluorinated chains to the polymer-air interface, due to the chemical incompatibility with the bulk.

Despite water-solubility of copolymers, water contact angle of annealed films was stable during measurement, suggesting the effective migration of fluorinated moieties to the outermost surface of the film. In Table 19 are reported values of water contact angle after 15 seconds, as a function of copolymer composition. Surfaces are moderately hydrophobic with $\theta_w \geq 90°$ even for the copolymer with only 10% mol FA. Differently, only FA content of 31% mol provided a little lipophobicity (θ_h = 72°). PEGMA77-*co*-FA23 and PEGMA80-*b*-FA20, having a similar PEGMA content, displayed a similar water contact angle; n-hexadecane contact angle was about 20° higher in block

copolymer, demonstrating the stronger tendency for phase separation for this macromolecular architecture. In any case, these results were explained only thanks to efficient surface reorganisation, after thermal treatment. More details will be given in following paragraph, regarding chemical surface analysis.

Measurements of liquid-solid contact angles of polymer films are commonly used to evaluate solid surface tension (γ_{sv}). Many different approaches have been developed to correlate θ and γ_{sv}, but all of them are based on still debated assumptions and none of them is universally accepted.[98] Accordingly, we followed two alternative approaches to calculate the solid surface tension, reported in Table 20, from experimental θ values.

Table 19: Static contact angle values for the calculation of surface tension of amphiphilic fluorinated copolymers, measured with water, *n*-hexadecane, *n*-dodecane, *n*-decane, *n*-octane, *n*-heptane.

Film	θ_w (°)	θ_h (°)	θ_{C12} (°)	θ_{C10} (°)	θ_{C8} (°)	θ_{C7} (°)
pPEGMAc	13 ± 2	0	--	--	--	--
PEGMA90-co-FA10	89.6 ± 0.7	47.3 ± 0.7	43.5 ± 0.5	39.9 ± 0.3	33.5 ± 0.5	29.7 ± 1
PEGMA77-co-FA23	95.0 ± 1.1	43.8 ± 0.7	41.0 ± 0.5	32.3 ± 0.4	24.9 ± 1.4	17.8 ± 2.0
PEGMA69-co-FA31	103.5 ± 0.5	72.3 ± 0.8	58.3 ± 0.7	56.1 ± 0.7	39.4 ± 0.8	38.9 ± 0.9
PEGMA80-b-FA20	91 ± 2	63 ± 1	--	--	--	--

Table 20: Comparison of surface tension values calculated with different methods, for amphiphilic fluorinated copolymers.

Film	γ_{sv}^{OWK} (mN/m)	γ_{sv}^{d} (mN/m)	γ_{sv}^{p} (mN/m)	γ_{sv}^{EqN} (mN/m)
pPEGMAc	73.2	46.3	26.9	--
PEGMA90-co-FA10	24.5	19.4	5.1	19.2
PEGMA77-co-FA23	23.3	20.5	2.9	20.2
PEGMA69-co-FA31	14.5	11.7	2.8	15.4
PEGMA80-b-FA20	20.9	14.6	6.3	--

Additive method of Owens, Wendt and Kaeble (OWK) was applied to calculate the surface free energy, and its polar and dispersive components from θ_w and θ_h from the following equation:

$$\gamma_{lv}(1 + cos\theta) = 2\left[(\gamma_{sv}^{p}\gamma_{lv}^{p})^{1/2} + (\gamma_{sv}^{d}\gamma_{lv}^{d})^{1/2}\right] \quad \text{Eq. 14}$$

Moreover, *n*-heptane, *n*-octane, *n*-decane and *n*-dodecane were used with water as interrogating liquids on selected samples to evaluate the surface free energy with Neumann equation of state:

$$cos\theta = 2\sqrt{\frac{\gamma_{sv}}{\gamma_{lv}}}e^{-\beta(\gamma_{lv}-\gamma_{sv})^2} - 1 \quad \text{Eq. 15}$$

More calculation details were reported in experimental paragraph.

The values of solid surface energy obtained with the two methods were in good agreement, and showed the same decreasing trend, with increasing FA content. γ_{sv}^{OWK} were generally lower than the respective values evaluated with the equation of state γ_{sv}^{EqN}. This effect seems to be inherent in the system and derives from the difficulty in correlating contact angle values with vastly different surface tensions of the wetting liquids (Figure 71). Parameter β has a minimal impact in fit result, and was maintained constant, as suggested in the literature.[99]

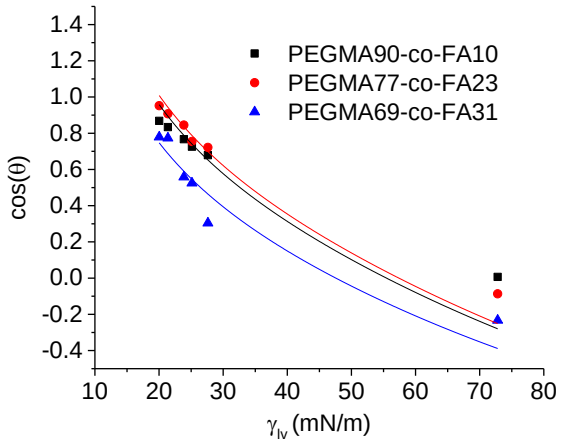

Figure 71: Cos(θ) values vs surface tension of interrogating liquid, fitted with Neumann equation of state.

In any case, the values of γ_{sv} for amphiphilic fluorinated copolymers, were consistent with a low surface energy of the polymer film, being lower than 25 mN/m. Block copolymer PEGMA80-*b*-FA20 showed γ_{sv} values lower than random copolymer with similar composition (PEGMA77-*co*-FA23), suggesting that in the latter the fluorine segregation was less effective than in the former copolymers, where the neat separation of the chemically incompatible components blocks enhanced migration of the fluorinated moieties towards the outer surface. By contrast, random distribution of fluorinated side chains provided a comparatively weak driving force to segregation and surface migration.

2.1.6.2 Surface chemistry analysis

X-ray photoelectron spectroscopy (XPS) experiments were performed on copolymers films, to gain information about the surface chemical composition. Indeed, XPS spectra give semi-quantitative data relative to molar atomic composition, and functional group populating the outermost layer of the sample. In XPS experiments the surface is irradiated with a source of soft x-rays (energy < 1200-1500 eV) that stimulate the photoemission of primary electrons from inner electron shells (K and L). These electrons have different binding energies, characteristic of every chemical element, thus allowing the quantification the atomic composition of the sampled volume. Binding energy is affected by the local chemical surroundings of a given atom. For carbon, it is possible to distinguish different contributions from atoms involved in different chemical bonds, such as C-C, C-O or C-F. Photoemission leaves an electron vacancy in internal electron shells, that is recovered by an external electron, associated with the emission of secondary Auger electron or x-ray fluorescence emission.

3% (wt/vol) copolymer chloroform solutions were spin-coated on clean glass slides, then films were annealed at 120°C overnight in vacuum oven. Spectra were recorded at three different photoemission angles φ of 70, 45 and 20°, resulting in an increasing sampling depth between 3 and 10 nm (for C(1s)). As an example, spectra of PEGMA69-co-FA31 were displayed in Figure 72. In all survey spectra, peaks due to C(1s) around 290 eV, O(1s) ≈ 536 eV, F(1s) ≈ 693 eV and F(2s) ≈ 40 eV were obvious. Experimental atomic composition,

calculated for every φ, were compared in Table 21 with the stoichiometric values.

In all cases, molar contents of C, O and F atoms varied with φ, demonstrating the formation of a gradient in composition in the direction perpendicular to film surface. In detail, C and O molar percentages decreased at deeper sampling depth. Distinctly, F content increased in superficial layers, and was significantly higher than the expected stochiometric value, in all the 3 – 10 nm range. Thus, film surfaces were highly enriched in fluorine, due to the phase segregation and migration of perfluorinated side chains to the polymer-air interface. This migration was more efficient in block copolymer PEGMA77-*b*-MAF23 (44.7% of F at 70°), compared with the random copolymer PEGMA77-*co*-FA23 (34.9% of F at 70°) with equivalent composition, suggesting a contribution of macromolecular architecture on phase segregation. Introducing a low amount of FMR repeating units in the copolymer PEGMA74-*co*-FA25-*co*-JCBF1 showed only a little decrease in fluorine at the surface (28.6% at 70°).

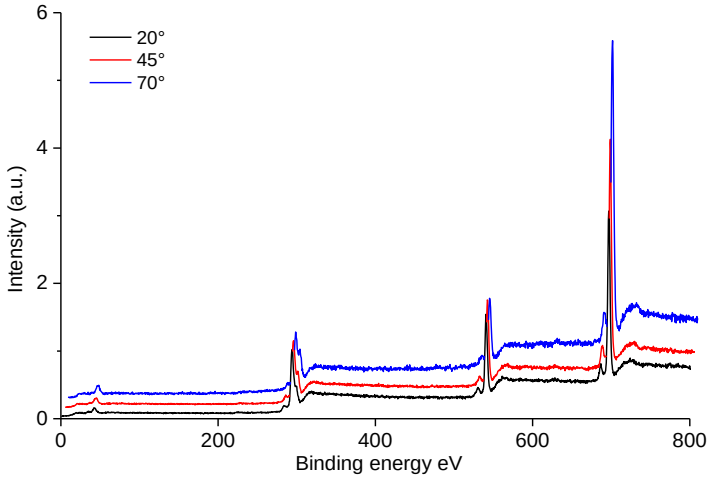

Figure 72: XPS survey spectra of PEGMA69-*co*-FA31 film at different photoemission angles.

Table 21: XPS chemical composition of copolymer PEGMAx-*co*-FAy films.

Film	***φ (°)***	***C (%)***	***O (%)***	***F (%)***
PEGMA90-co-FA10	70	48.8	19.5	31.7
	45	55.4	24.7	19.9
	20	57.2	26.2	16.6
	stoich.	62	32	6
PEGMA77-co-FA23	70	48.1	17.0	34.9
	45	53.4	23.1	23.5
	20	57.9	24.2	17.9
	stoich.	61	26	13
PEGMA69-co-FA31	70	44.9	12.9	42.2
	45	47.5	18.6	33.9
	20	51.2	20.2	28.6
	stoich.	57	26	17
PEGMA77-b-MAF23	70	43.5	11.8	44.7
	45	50.2	18.8	31.0
	20	54.8	22.0	23.2
	stoich.	61	26	13
PEGMA74-co-FA25-co-JCBF1	70	52.4	19.0	28.6
	45	58.3	23.5	18.2
	20	59.6	25.2	15.2
	stoich.	61	25	14

C(1s) signal resulted structured in different overlapping components in high resolution spectra. The deconvolution of the peak allowed the calculation of molar percentage of different group of atoms containing carbon. At 292.1 and 294.6 eV were positioned the signals of CF_2 and CF_3 respectively, from perfluorinated side chains. Peaks at 289.2, 286.6 and 285.0 eV derived from the transition assigned to carbon in C(=O), C-O-C and C-C, respectively (Figure 73).

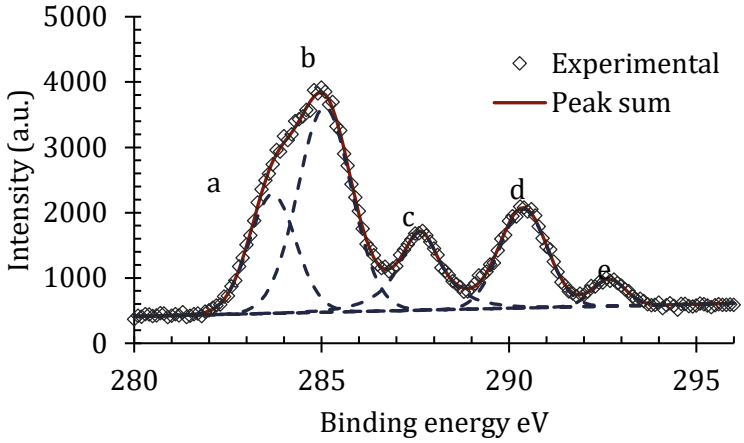

Figure 73: Deconvolution of signal C(1s) for film PEGMA69-*co*-FA31 (φ = 70°). Peak assignment a: C-C; b: C-O-C; c: C(=O); d: CF_2; e: CF_3.

In Table 22 were reported the stoichiometric composition and the experimental composition of these groups at φ = 70°. This analysis confirmed that the film surface was highly enriched in CF_2 and CF_3, whose content were significantly higher than the expected stoichiometric values. The gradient composition was also confirmed. Perfluorinated carbon group content increase at lower sampling depth, while oxygen containing group preferably occupied the deeper layers of the film, as shown in Figure 74.

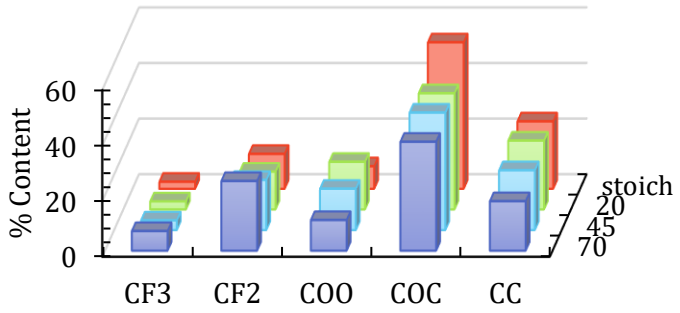

Figure 74: Comparison of deconvolution result of spectra for copolymer PEGM69-*co*-FA31 at different angles (sampling depth).

Table 22: Deconvolution of the C(1s) signal in high resolution XPS spectra for copolymer PEGMAx-*co*-FAy. Peak assignation a: C-C; b: C-O-C; c: C(=O); d: CF_2; e: CF_3.

Film	*φ (°)*	*a (%)*	*b (%)*	*c (%)*	*d (%)*	*e (%)*
PEGMA90-co-FA10	70	25	42	17	13	3
	stoich.	23	64	8	4	1
PEGMA77-co-FA23	70	18	52	9	15	6
	stoich.	20	63	7	8	2
PEGMA69-co-FA31	70	18	39	11	25	7
	stoich.	24	52	8	13	3
PEGMA77-b-MAF23	70	15	44	7	26	8
	stoich.	20	63	7	8	2
PEGMA74-co-FA25-co-JCBF1	70	24	53	7	13	3
	stoich.	20	62	7	9	2

2.2 Conclusion

Amphiphilic random copolymers, with an adequate primary structure, thus with the ability to intramolecularly fold in unimer nanostructures, represent promising candidates in many potential applications, e.g. in catalysis as artificial enzymes, in nanomedicine as vectors for contrast agents and drug delivery carriers, in nanotechnology at large. In particular, single-chain folding polymers can promote the developments of novel nanotechnology of soft materials, with a new, simplified approach on bottom-up process design. Other intrinsic advantages are improved atom economy and reduction of the size easily available, with respect to present nanotechnologies that in polymer field rely on intermolecular collective aggregates. Moreover, the non-covalent stabilisation of folded polymers results in reversible, responsive nanomaterials, that may display interesting functions, triggered by external stimuli (e.g. light, heat, pH).

Amphiphilic copolymers of this work, displayed a complex, multimodal self-assembly behaviour, that is driven mainly by the hydrophobic interactions in water solution taking place between the perfluorinated side chains in PEGMA-FA copolymer system and the siloxane side chains in the PEGMA-SiMA

copolymer system. Random copolymers, in particular, better fitted the requirement for the formation of intramolecular folded unimer micelles both in perfluorinated and siloxane based copolymers. To the best of our knowledge, PEGMAx-*co*-SiMAy or analogue polymers have never been proposed in the literature as single-chain folding systems. Thus, their study was initiated here with some proof-of-concept experiments and represent an interesting development of this work and a significant contribution to the field.

The versatility of ATRP technique was fundamental to obtain the copolymers with a wide range of hydrophilic/hydrophobic balances, necessary for the detailed study of the self-assembly in solution and solid state. Cu(0)-mediated RDRP was explored for the synthesis of amphiphilic block copolymers. This technique would offer the advantage to lead to block copolymers in green solvent like water, with reduced content of heavy metal catalyst, at room temperature. Moreover, performing the reaction in water would enable the production of concentrated dispersions of nanostructured polymeric aggregates, directly during the polymerisation thanks to the polymerisation-induced self-assembly effect. Unfortunately for the proposed system, a careful optimisation of the polymerisation conditions, to achieve such ambitious goal, is still needed, and represents another possible future development of this research. An alternative to Cu(0)-mediated RDRP to develop a greener synthetic route is represented by ARGET-ATRP. Taking advantage of a reducing agent to regenerate the activating species, it allows to reduce the metal catalyst content, to tolerate the presence of air, and to use polar solvents like water or ethanol. For these reasons ARGET-ATRP should be considered for the extension of the present study.

Fluorescent probes were extensively used to monitor the self-assembly behaviour of amphiphilic copolymers. Interestingly, the covalent functionalisation of the copolymer proposed in this work does not hamper the self-assembly. Accordingly, these functional polymers were investigated with the primary intent to follow the folding and aggregation process by fluorescence emission spectroscopy. Indeed, they could find a useful application in vapochromic polymeric films, or in bioconjugates with intrinsic fluorescence that could be exploited to reveal their bioavailability in cells and tissues.

The temperature driven aggregation of unimer micelles in larger multi-chain structures was of special interest to us and prompted more studies. All polymers

exhibited a critical transition temperature, that could be regularly lowered by increasing the hydrophobic unit content in the polymer itself. The loading and release of ethidium bromide was shown as a model of the controlled release of a molecule of interest, hosted in the folded unimer micelle, as a response to a temperature variation. This phenomenon would be more appealing if the transition occurred at a physiological temperature. Our findings suggest that it should be possible to reach lower transition temperatures, by further increasing the molar fraction of hydrophobic side chains. The use of a shorter poly(ethylene glycol) methacrylate could be an alternative route to pursue this objective in the continuation of this study.

The elucidation of exact nature of single-chain folded macromolecules, obtained by isotropic hydrophobic interaction of side chains randomly distributed along a macromolecule, in terms of morphology, conformation and dynamics, is challenging. Computational simulations provided a model of the folding for amphiphilic/fluorinated random copolymers of this work in water. Experimentally, small angle neutron scattering experiments in D_2O provided greater detail on the unimer micelle morphology, and further analysis of the thermophilic aggregates are already scheduled at Larmor instrument at ISIS facility. The ellipsoidal shape of some of the unimer micelles found in this work is at variance with a much quoted depiction of their spherical shape. Thus, a variety of nanoassemblies seems to be possible for self-folding copolymers and would be worth investigating.

The potential of amphiphilic copolymer self-assembly is not limited to the solution realm. NMR relaxometry study of amphiphilic/fluorinated random copolymers, owing to the concomitant presence of both ^{1}H and ^{19}F nuclei, demonstrated an increasing degree of assembling of the fluorinated side chains that became less mobile, with increasing content of perfluorinated units. Correspondingly, the mobility of PEGMA side chains was equally affected, and became more and more hindered, with the increasing content of associated fluorinated side chains.

The self-assembly of perfluorinated side chains at the surface of polymeric films was also considered. Thermally annealed thin films, despite the water solubility of bulk material, showed moderate hydrophobicity and lipophobicity in sessile drop contact angle measurements in static conditions. Surface wettability was greatly influenced by migration of the perfluorinated side chains driven to the

film surface by their lower surface tension. This was confirmed by surface chemistry analysis obtained through angle resolved X-ray photoemission spectroscopy. This analysis evidenced that the film surfaces were highly enriched in hydrophobic/lipophobic perfluorinated side chains, resulting from their phase segregation and migration to the polymer-air interface during thermal treatment, directed by the chemical incompatibility with the hydrophilic oxyethylene side chains.

2.3 Experimental

2.3.1 Materials

Anisole (Sigma Aldrich) was vacuum distilled over sodium. Copper bromide (CuBr, Sigma Aldrich) was extracted with glacial acetic acid then washed with diethyl ether, dried and stored under nitrogen. N,N,N′,N′′,N′′-Pentamethyldiethylenetriamine (PMDETA, Sigma Aldrich), and ethyl α-bromophenylacetate (EBPA, Sigma Aldrich) were freshly distilled before use. Perfluorohexylethyl (meth)acrylates (FA and MAF, Fluoryx Inc.), monomethacryloxypropyl terminated polydimethylsiloxane (SiMA, M_n = 680 g/mol, Fluorochem) and poly(ethylene glycol) methyl ether methacrylate (PEGMA, M_n = 300 g/mol, Sigma Aldrich) were filtered through basic alumina to remove inhibitors. Ethidium bromide (Sigma Aldrich), trifluoroethanol (Sigma Aldrich), hexafluorobenzene (Alfa Aesar) were used as received. Common laboratory solvents and other reagents (Sigma Aldrich) were used as received.

2-cyano-2-[4-vinyl(1,1'-biphenyl)-4'-yl]vinyljulolidine (JCBF) was kindly provided by prof. Pucci[49]. 9-[2-(2-bromo-2-methylpropanoyloxyethyloxycarbonyl)-2-cyanovinyl]julolidine (JBr) was previously synthesised in our laboratory.

2.3.2 Characterisation

Nuclear magnetic resonance (NMR)

^{1}H NMR and ^{19}F NMR solution spectra were recorded with a Bruker Avance DRX 400 spectrometer.

All the NMR relaxometry measurements were performed at the ^{1}H and ^{19}F Larmor frequencies of 20.8 and 19.6 MHz, respectively, using a Niumag permanent magnet interfaced with a Stelar PCNMR console. The experiments were carried out at the temperature of 24 °C, which was controlled within ± 0.1 °C with a Stelar VTC90 variable temperature controller. The 90° pulse durations were 3 and 3.2 μs for ^{1}H and ^{19}F, respectively. ^{1}H solid echo FID's were recorded using an echo delay of 14 μs and accumulating 200-600 transients. ^{1}H CPMG experiments were carried out acquiring 400-600 scans with an echo time of 15 μs for homopolymer pFA and 50 μs for all the other samples. For all the ^{1}H experiments a recycle delay (*rd*) of 1 s between two consecutive scans was used, with the exception of sample pFA, for which a longer *rd* of 3 μs was necessary to allow ^{1}H longitudinal magnetisation to be completely recovered. ^{19}F solid echo FID's were recorded with an echo delay of 12 μs, while for CPMG experiments an echo time of 15 μs was used. In both cases 600 transients were acquired with an rd of 1 s. The analysis of the experimental solid echo FID and CPMG relaxation curves was performed using a non-linear least squares fitting procedure implemented in the Mathematica environment.

Size exclusion chromatography (SEC)

The number and weight average molecular weights were determined by size exclusion chromatography (SEC) with a Jasco PU-2089Plus liquid chromatograph equipped with two PL gel 5 μm mixed-D columns, a Jasco RI-2031Plus refractive index detector and a Jasco UV-2077Plus UV/vis detector. Poly(methyl methacrylate) standards (from 1160 g/mol to 124300 g/mol) were used for calibration.

Thermal analysis: differential scanning calorimetry (DSC).

Analyses were performed with a Mettler DSC-30 and a Mettler DSC 922e instruments. The glass transition temperature was taken as the inflection temperature in the second heating cycle.

Dynamic light scattering (DLS)

DLS measurements of polymer solutions were taken with a Beckman Coulter Delsa Nano C particle analyser (detection angle = 166.22°). Intensity, volume and number distribution were obtained from the signal autocorrelation function through CONTIN analysis in the instrument software. Samples were prepared in filtered solvent (0.2 μm CA or PTFE filters) to reduce external contamination.

Small angle neutron scattering

SANS experiments were carried out by using the high flux beam line SANS2D at the ISIS facility, Oxford, UK. Elastic Neutrons scattering was used to investigate size, shape and spatial arrangement of polymers on length scales between 0.25-300 nm using the 2 m guide sections with variable collimation apertures, two moveable 1 m^2 detectors and almost 77,000 pixels, using Hellma quartz cells with capacity of 0.5 cm^3. The incident beam wavelength range of 2.2 Å (with the 1 m^2 detector offset sideways and vertically by 150 mm) was used resulting in an effective Q range of ~0.005-0.7 $Å^{-1}$. The measurements gave the absolute scattering cross section I(Q) (cm^{-1}) as a function of momentum transfer Q ($Å^{-1}$). The absolute intensities (±5%) of the calibrated signal were corrected for sample transmission and cell and solvent backgrounds. For aqueous solvent, pure deuterated water, D_2O (scattering length density $\rho_{D2O} = 6.330 \cdot 10^{10}$ cm^{-2}) was used to provide the necessary contrast. Temperature of the sample environment was controlled at ± 0.1 °C. The experiments were performed at 25.0 ± 0.1°C, 55.0 ± 0.1° or 65.0 ± 0.1°C on D_2O dissolved samples at 2 and 5 mg/ml concentration in 2 mm Hellma quartz cells, each one positioned in the thermally controlled sample holder rack (able to slide automatically by means of a proper software macro). For data analysis the FISH interactive fitting program available at SANS2D was used.

Molecular dynamic (MD) simulations

Molecular dynamic simulation of amphiphilic fluorinated copolymer single-chain folding was modelled from a polymer that was designed from two building units, HYD (PEGMA) and LIP (FA), containing the hydrophilic and hydrophobic side chain respectively. The polymer was capped at both ends with a methyl group. Bonding and Van der Waals parameters for all atoms were taken from the General Amber Force Field (GAFF),[100] while partial charges were derived following the standard RESP procedure.[101] Each unit was capped with methyl

groups and the structure was optimised at the B3LYP/6-31G(d) level of theory starting from an outstretched conformation of the side chain. Charges were derived by fitting the HF/6-31G(d) electrostatic potential with the two-stage RESP procedure using AmberTools. The sum of charges of both capping methyls was constrained to zero. Water solvent was modelled as TIP3P,[102] whereas parameters for $CHCl_3$ solvent were taken from the literature.[103]

Four 104-mer sequences were generated by randomly selecting the unit with probability 80(HYD)/24(LIP). Notice that the actual HYD/LIP ratio was not necessarily equal to 80:24 in each sequence. The polymer starting structure was built by adding building blocks one at a time, each time relaxing the structure.

A block ordered sequence was generated by creating four blocks of six LIP units equally spaced by HYD units. The starting structure was built as described above. In order to destroy the high symmetry of the system we ran a 2 ns MD simulation at high temperature (600K) to obtain a random initial structure. A hydrophilic-only polymer was also built with 104 HYD units following the same procedure as for the block copolymer.

Every simulation was performed as follow. The initial structure was put into a rectangular box of water solvent molecules. Two structures were also solvated in $CHCl_3$. The dimensions of the box were chosen so that the edges of the box were at a minimum distance of 20Å from the polymer atoms. The solvated system was heated up to 300K for 100 ps, followed by a c.a. 200 ns of production run. All the MD simulations were performed in a NPT ensemble using a Langevin thermostat with a damping constant of 1 ps^{-1} and the isotropic Monte Carlo barostat as implemented in Amber14. The integration time step was set to 2 fs in combination with the SHAKE algorithm for hydrogen atoms.

Absorption/emission spectroscopy

UV-vis absorption spectra were recorded at room temperature on a Perkin-Elmer Lambda 650 spectrophotometer. An absorption calibration curve ($Abs = k \cdot conc$; where k = 21500 $M^{-1}cm^{-1}$, R^2 = 0.9997) obtained from $5 \cdot 10^{-7}$–$5 \cdot 10^{-5}$ M chloroform solutions of the fluorescent monomer allowed the determination of the chemical composition of terpolymer. The molar extinction coefficient variation from monomer to polymer was assumed to be negligible.

Fluorescence spectra were measured on a Horiba Jobin-Yvon Fluorolog-3 spectrofluorometer equipped with a 450 W xenon arc lamp, double-grating

excitation and single-grating emission monochromators. Fluorescence quantum yield Φ was determined using perylene in ethanol as standard,[104] as a result of the equation:

$$\Phi = \Phi_{st} \frac{\int_0^\infty I_{(\nu)} d\nu}{\int_0^\infty I_{st(\nu)} d\nu} \frac{(1-10^{-A_{st}})}{(1-10^{-A})} \frac{n^2}{n_{st}^2} \qquad \text{Eq. 16}$$

were $\int_0^\infty I_{(\nu)} d\nu$ is the area under the emission curve (in the 420 – 670 nm range); A is the absorbance at excitation wavelength; n is the refractive index; the st subscript means the value referring to perylene or fluorescein standard.

For ethidium bromide experiments a Perkin Elmer LS55 spectrofluorometer was used to record fluorescence spectra.

Static contact angle

Contact angle measurements were carried out using an FTA200 Camtel goniometer. Polymer films 200-300 nm thick were prepared by spin-coating a 3 wt % polymer solution on glass substrates. The rotation speed varied based on the polymer, but most of the samples were prepared with a speed of 5000 rpm. The samples, otherwise explicitly specified, were annealed in a vacuum oven at 120 °C for 12 hours and slowly cooled to room temperature. Wetting liquids were products of the highest purity available. Liquid surface tensions of all the wetting liquids used in contact angle measurements are collected in Table 23.

Table 23. Surface tension of the testing liquids

Liquid	γ_{lv}	γ_{lv}^d	γ_{lv}^p
Water	72.80	21.80	51.00
n-heptane	20.03	20.03	0.00
n-octane	21.38	21.38	0.00
n-decane	23.88	23.88	0.00
n-dodecane	25.13	25.13	0.00
n-hexadecane	27.62	27.62	0.00

In the Owens-Wendt-Kaelble[105,106] approach surface tension is composed of two contributions such as for γ_{sv}:

$$\gamma_{sv} = \gamma_{sv}^d + \gamma_{sv}^p \qquad \text{Eq. 17}$$

where γ_{sv}^{d} and γ_{sv}^{p} are the dispersive and the polar surface tension components, respectively. A geometric mean relationship is postulated and γ_{sl} can be calculated as:

$$\gamma_{sl} = \gamma_{sv} + \gamma_{lv} - 2(\gamma_{sv}^{p}\gamma_{lv}^{p})^{1/2} - 2(\gamma_{sv}^{d}\gamma_{lv}^{d})^{1/2} \quad \text{Eq. 18}$$

When a droplet of a wetting liquid makes contact with a solid surface the balance between the forces along the three phase boundaries is defined by the Young's equation:

$$\gamma_{lv}cos\theta = \gamma_{sv} - \gamma_{sl} \quad \text{Eq. 19}$$

where γ_{lv} is the surface tension of the wetting liquid in equilibrium with its vapor, θ is the contact angle, γ_{sv} is the surface tension of the solid and γ_{sl} the interfacial tension between the solid and the wetting liquid.

Combining the last two equations yields the relation:

$$\gamma_{lv}(1 + cos\theta) = 2\left[(\gamma_{sv}^{p}\gamma_{lv}^{p})^{1/2} + (\gamma_{sv}^{d}\gamma_{lv}^{d})^{1/2}\right] \quad \text{Eq. 20}$$

Accordingly, at least two contact angle values, like θ_w (water) and θ_h (hexadecane) are necessary to determine the surface tension γ_{sv} of the polymer surface from its two components, knowing the characteristic of the wetting liquid.

An approach based on an equation of state that could allow the calculation of solid surface tension has been developed by Kwok and Neumann[98,99]. They suggested the following equation:

$$cos\theta = 2\sqrt{\frac{\gamma_{sv}}{\gamma_{lv}}}e^{-\beta(\gamma_{lv}-\gamma_{sv})^2} - 1 \quad \text{Eq. 21}$$

In this case, from a series of contact angles of liquids with different γ_{lv}, γ_{sv} is fitted as a parameter. β is generally considered as a constant, and proposed value in the literature is 0.0001234 m^2/mN^2.

X-ray photoelectron spectroscopy (XPS)

XPS spectra were recorded by using a Perkin-Elmer PHI 5600 spectrometer with a standard Al–Ka source (1486.6 eV) operating at 350 W. The working pressure was less than 10^{-8} Pa. The spectrometer was calibrated by assuming the binding energy (BE) of the Au $4f_{7/2}$ line to be 84.0 eV with respect to the Fermi level.

Extended (survey) spectra were collected in the range 0 to 1350 eV (187.85 eV pass energy, 0.4 eV step, 0.05 s step^{-1}). Detailed spectra were recorded for the following regions: C (1s), O (1s), F (1s) (11.75 eV pass energy, 0.1 eV step, 0.1 eV s step^{-1}). The standard deviation (SD) in the BE values of the XPS line was 0.10 eV. The atomic percentage, after a Shirley type background subtraction,[107] was evaluated using the PHI sensitivity factors.[108] To consider charging problems, the C (1s) peak was considered at 285.0 eV and the peak BE differences were evaluated.

2.3.3 Synthesis

2.3.3.1 Synthesis of copolymers PEGMAx-*co*-FAy

The synthesis of PEGMA77-*co*-FA23 will be described. PEGMA (4.59 ml, 16.07 mmol), FA (3.842 g, 9.15 mmol), PMDETA (41.9 µl, 0.20 mmol), EBPA (35.2 µl, 0.20 mmol) and anisole (3.25 ml) were degassed in a schlenk tube with three freeze-pump-thaw cycles. Then CuBr (28.8 mg, 0.20 mmol) was added and three more freeze-pump-thaw cycles were performed before the polymerisation was started at 70 °C under nitrogen atmosphere. Periodically, aliquots of the reaction mixture were withdrawn for kinetics and molecular weight analysis. After 24 hours, the reaction was stopped by exposure to air and quenching to 0 °C. The crude product was filtered through basic alumina to remove catalyst and repeatedly precipitated from chloroform into *n*-hexane. Final yield 54%.

SEC ($CHCl_3$) M_n = 13700 g/mol M_w/M_n = 1.30.

^{1}H NMR [Acetone-d_6]: δ (ppm) = 7.2-7.4 (0.5H, arom), 4.0-4.6 (21,1 H, $COOCH_2$), 3.4-3.6 (162,1 H, OCH_2CH_2, CHCOO), 3.34 (24.3 H, OCH_3), 2.5 (4.8 H, CH_2CF_2), 0.7-2.3 (48 H, CH, CH_2, CH_3).

^{19}F NMR [Acetone-d_6, CF_3COOH]: δ (ppm) = -5.6 (3F, CF_3), -38.5 (2F, CF_2CH_2), -46 to -48 (6F, CF_2), -51 (2F, $C\underline{F_2}CF_3$).

In Table 24 were summarised reaction conditions for the synthesis of the other copolymers of the series PEGMAx-*co*-FAy. In case of PEGMA29-*co*-FA71 the polymer was precipitated in methanol.

Table 24: Reaction conditions for the synthesis of amphiphilic fluorinated random copolymers PEGMAx-*co*-FAy.

Copolymer	***PEGMA90-co-FA10***	***PEGMA69-co-FA31***	***PEGMA29-co-FA71***
PEGMA (mmol)	8.7	6.3	3.9
FA (mmol)	1.0	2.8	9.1
M/I	100	100	100
CuBr (mmol)	0.1	0.09	0.13
Initiator (mmol)	0.1 (EBIB)	0.09 (EBIB)	0.13 (EBIB)
PMDETA (mmol)	0.1	0.09	0.13
Solvent (ml)	6.0 (Anisole)	6.0 (Anisole)	2.5 (TFT)
T (°C)	90	90	90
Time (h)	24	24	24
Yield %	89	87	91

2.3.3.2 Synthesis of copolymer PEGMA74-*co*-FA25-*co*-JCBF1

PEGMA (0,706 ml, 2.47 mmol), FA (0,162 ml, 0,60 mmol), JCBF (6.20 mg, 0.015 mmol), PMDETA (6.45 µl, 0.03 mmol), EBPA (5.4 µl, 0.03 mmol) and anisole (0.5 ml) were degassed in a schlenk tube with three freeze-pump-thaw cycles. Then CuBr (4.4 mg, 0.03 mmol) was added and three more freeze-pump-thaw cycles were performed before the polymerisation was started at 70 °C under nitrogen atmosphere. After 24 hours, the reaction was stopped by exposure to air and quenching to 0 °C. The crude product was filtered through basic alumina to remove catalyst and repeatedly precipitated from chloroform into *n*-hexane. Final yield 53%.

SEC ($CHCl_3$) M_n = 6900 g/mol M_w/M_n = 1.25.

^{1}H NMR [Acetone-d_6]: δ (ppm) = 4.0-4.6 (2.7 H, $COOCH_2$), 3.4-3.6 (18 H, OCH_2CH_2, CHCOO), 3.34 (3 H, OCH3), 2.5 (2.5 H, CH_2CF_2), 0.7-2.3 (5.8 H, CH, CH_2, CH_3).

^{19}F NMR [Acetone-d_6, CF_3COOH]: δ (ppm) = -5.6 (3F, CF_3), -38.5 (2F, CF_2CH_2), -46 to -48 (6F, CF_2), -51 (2F, $C\underline{F_2}CF_3$).

2.3.3.3 Synthesis of copolymers PEGMAx-*co*-SiMAy.

The synthesis of PEGMA85-*co*-SiMA15 will be described. PEGMA (1.45 ml, 5.07mmol), SiMA (1.54 ml, 2.17 mmol), PMDETA (15.1 µl, 0.07 mmol), EBPA (12.7 µl, 0.07 mmol) and anisole (6 ml) were degassed in a schlenk tube with three freeze-pump-thaw cycles. Then CuBr (10.4 mg, 0.07 mmol) was added and three more freeze-pump-thaw cycles were performed before the polymerisation was started at 90 °C under nitrogen atmosphere. Periodically, aliquots of the reaction mixture were withdrawn for kinetics and molecular weight analysis. After 24 hours, the reaction was stopped by exposure to air and quenching to 0 °C. The crude product was filtered through basic alumina to remove catalyst and repeatedly precipitated from chloroform into *n*-hexane. Final yield 5%.

SEC ($CHCl_3$) M_n = 13700 g/mol M_w/M_n = 1.30.

^{1}H-NMR [$CDCl_3$]: δ (ppm) = 4.0-4.4 (2.35 H, $COOCH_2$), 3.2-3.9 (18 H, OCH_2), 3.3 (3H, OCH_3) 2.1-0.8 (7.46 H, $SiCH_2\underline{CH_2}CH_2$, $\underline{CH_2CH_3}$, $C\underline{H_2}CC\underline{H_3}$), 0.5 (0.70 H, $SiCH_2$), 0.1 (2.1 H, $SiCH_3$)

In Table 25 were summarised reaction condition for the synthesis of the other copolymers of the series PEGMAx-*co*-SiMAy, the describe procedure was followed.

Table 25: Reaction conditions for the synthesis of amphiphilic siloxane based random copolymers PEGMAx-*co*-SiMAy.

Copolymer	***PEGMA95-co-SiMA5***	***J(PEGMA94-co-SiMA6)***
PEGMA (mmol)	7.99	2.66
SiMA (mmol)	0.88	0.27
M/I	100	100
CuBr (mmol)	0.09	0.03
Initiator (mmol)	0.09 (EBPA)	0.03 (JBr)
PMDETA (mmol)	0.09	0.03
Anisole (ml)	6.0	2.0
T (°C)	90	90
Time (h)	24	24
Yield %	17	42

2.3.3.4 Synthesis of homopolymers pPEGMAa-e

The synthesis of pPEGMAb will be described. PEGMA (3.00 g, 10 mmol), PMDETA (28.9 mg, 0.16 mmol), EBPA (40.5 mg, 0.16 mmol) and anisole (1.5 ml) were degassed in a schlenk tube with three freeze-pump-thaw cycles. Then CuBr (23.9 mg, 0.16 mmol) was added and three more freeze-pump-thaw cycles were performed before the polymerisation was started at 70 °C under nitrogen atmosphere. After 3 hours the reaction was stopped by exposure to air and quenching to 0 °C. The reaction mixture was diluted with chloroform and filtered through basic alumina to remove catalyst, then it was repeatedly precipitated from chloroform into n-hexane.

SEC ($CHCl_3$) M_n = 7700 g/mol M_w/M_n = 1.45

1H NMR [Acetone-d_6]: δ (ppm) 7.2-7.4 (5 H, arom.), 3.9-4.4 (112 H, $COOCH_2$), 3.4-3.9 (896 H, OCH_2CH_2), 3.2-3.5(168 H, OCH_3), 0.8-2.2 (280 H, CH_2, CH_3)

2.3.3.5 Synthesis of homopolymer pFA

FA (3.00 g, 7.17 mmol), PMDETA (12.4 mg, 0.07 mmol), EBPA (17.4 mg, 0.07 mmol) and trifluorotoluene (1.5 ml) were degassed in a schlenk tube with three freeze-pump-thaw cycles. Then CuBr (10.3 mg, 0.07 mmol) was added and three more freeze-pump-thaw cycles were performed before the polymerisation was started at 90 °C under nitrogen atmosphere. After 24 hours the reaction was stopped by exposure to air and quenching to 0 °C. The crude product was repeatedly precipitated from chloroform into methanol.

SEC ($CHCl_3$) M_n = 7200 g/mol M_w/M_n = 1.04

^{1}H NMR [$CDCl_3$]: δ (ppm) = 4.0-4.6 (2 H, $COOCH_2$), 2.5 (2 H, CH_2CF_2), 0.7-2.3 (3 H, CH, CH_2).

^{19}F NMR [$CDCl_3$, CF_3COOH]: δ (ppm) = -5.6 (3F, CF_3), -38.5 (2F, CF_2CH_2), -46 to -48 (6F, CF_2), -51 (2F, $C\underline{F_2}CF_3$).

3 AMPHIPHILIC HYDROLYSABLE BLOCK COPOLYMERS FOR MARINE FOULING RELEASE COATINGS

In this chapter the designed amphiphilic hydrolysable copolymers will be presented, for the preparation of polymeric coatings with marine antifouling and fouling-release properties. The main aim of this design is to maintain the two critical features of amphiphilic fouling-release coatings: the bulk mechanical properties (i.e. the low elastic modulus) of PDMS-based coatings, favouring the fracture between the adhered biomass and the substrate, and features provided by the amphiphilic, nanostructuring, surface active copolymers, that weaken the interaction of bioadhesives and organisms with the substrate. In addition, a hydrolysable motif is combined in the design, borrowed from the chemistry of self-polishing erodible coatings.

Random and block (meth)acrylic copolymers bearing silylated ester groups as hydrolysable pendant groups are commonly reported as potential erodible polymers in acid, basic or seawater.[109–112] Erodible coatings are extensively studied for polymers devoted to therapeutic applications, where the leaching rate of drugs can be controlled by erosion of the carrier, and antifouling paints. In the antifouling paints area, self-polishing and controlled erosion coatings have been associated with linear thickness depletion with time, confined at the extreme outer surface of the paint. This is usually combined with the controlled release of biocidal molecules, dispersed in the hydrolysable binder, to sustain high efficacy over long time.

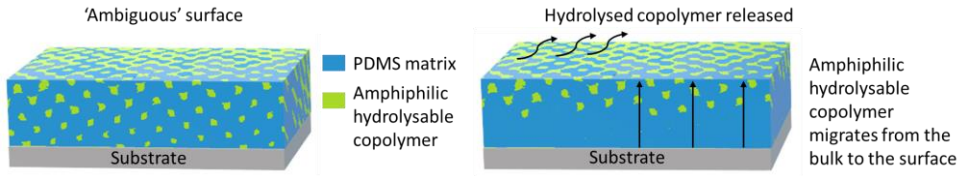

Figure 75: Schematic representation of surface renewal of polymeric coatings.

As reported in Figure 75, the copolymer additive could initially decorate the surface of the coatings, giving an ambiguous, water-responsive character to the surface, and possibly modulating the interactions with biofoulants. In time, labile silyl ester groups in contact with water could hydrolyse, thereby dynamically modifying the hydrophilic/hydrophobic balance of copolymer additive at the surface. Eventually, the hydrophilic character could prevail and the copolymer could be completely solubilised and removed from the surface. New, non-hydrolysed copolymer from the bulk of the film could diffuse within the matrix and migrate to the surface, renovating it. This should maintain the dynamic, water-responsive, ambiguous character of the coating for long immersion time, improving the efficacy without the use of any toxic biocide.

Polymers containing hydrolytically labile trialkylsilyl ester side groups were synthesised via RAFT polymerisation. Methacrylic monomers bearing tributylsilylated ester (TBSiMA) and triisopropylsilylated ester (TiPSiMA) have been selected, and their kinetics of homopolymerisation and copolymerisation with poly(ethylene glycol) methyl ether methacrylate (PEGMA M_n = 300 g/mol) were investigated by *in situ* ^{1}H NMR monitoring. Final amphiphilic hydrolysable copolymers to be used as additives in PDMS films were synthesised from a PDMS macromolecular RAFT chain-transfer agent, that could in addition act as a compatibiliser for the additive in the PDMS network. The hydrolysis reaction of the ester bond of the trialkylsilyl methacrylate group was monitored by a ^{1}H NMR study to compare the degradation profile.

Model coatings formulated with 10%wt of amphiphilic hydrolysable copolymer additive in a condensed PDMS matrix, deposited by solution casting were used to investigate the surface properties and to start the assessment of antifouling and fouling release properties against marine organisms in a static immersion campaign in natural seawater in field test trials.

3.1 Results and discussion

3.1.1 Polymer synthesis

3.1.1.1 *In situ* ^{1}H NMR monitoring of RAFT polymerisation

Several studies proposed the use of NMR spectroscopy to analyse directly the reaction medium of different polymerisation systems.[113,114,115] Carrying out the polymerisations within the cavity of the NMR spectrometer allows the reaction to be closely monitored. This gives extensive information on both the polymerisation kinetics and on the nature of the catalyst, with the advantage of exploiting only few milligrams of materials.

In this work, polymerisations were carried out in toluene-d_8 solution, in NMR tubes fitted with a Young's tap, to maintain an inert argon atmosphere, necessary for the radical reaction. A spectrum was taken over a prescribed short time period (generally ≈15 minutes) and conversion was measured by integration of monomer vinylic peaks with respect to initial spectrum. This resulted in conversion vs time and first order kinetics ($\ln([M]_0/[M])$ vs time) plots, with many more data points than from a sampled reaction, as is usually carried out. It also avoided the potential introduction of impurities and oxygen during sampling procedures, and any eventual sample treatments prior to analysis.

Reversible addition-fragmentation chain transfer (RAFT) polymerisation kinetics of trialkylsilyl methacrylates TBSiMA and TiPSiMA with PEGMA were studied (Scheme 15, top and bottom, respectively), starting in every case with 1.5 M total monomer concentration. 4-cyano-4-(dodecylsulfanylthiocarbonyl)sulfanylpentanoic acid (CDMP) was use as chain transfer agent (CTA), with AIBN as radical initiator in a CDMP:AIBN molar ratio 5:1. The molar fraction of comonomers was changed to explore a wide range of compositions (0%, 10%, 30%, 50%, 70% mol PEGMA). Only about 0.4 ml of reaction mixture were used in one experiment, and the reaction was usually observed overnight (for 12-15 hours).

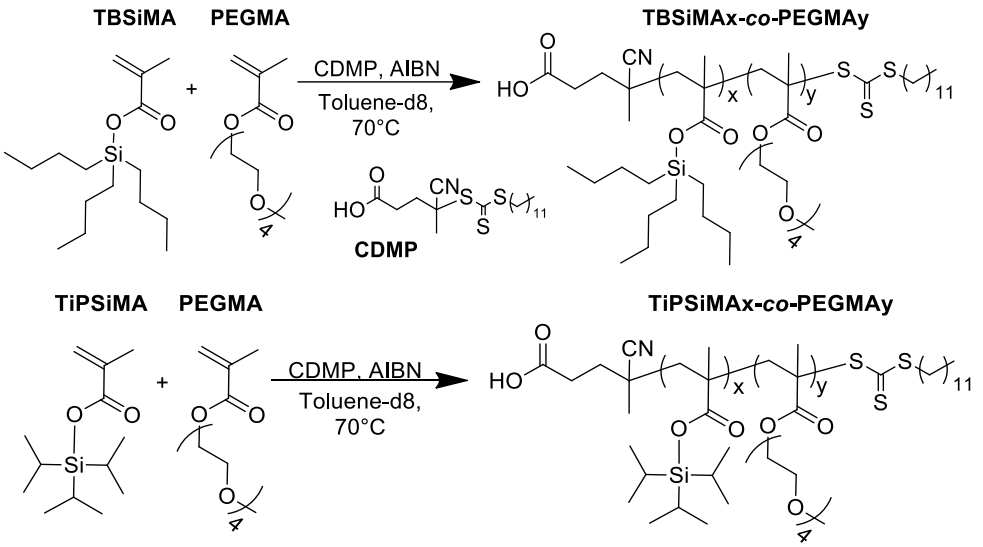

Scheme 15: Synthesis of amphiphilic trialkylsilyl methacrylate based random copolymers via RAFT polymerisation.

The copolymers of prepared in these RAFT (co)polymerisations were named as TBSiMAx-*co*-PEGMAy and TiPSiMAx-*co*-PEGMAy in which x and y refer to the mole percentage contents in the respective feed mixture.

In the case of TBSiMA homopolymerisation, monomer conversion and growing polymer chains were monitored using ^{1}H NMR spectroscopy. Selected spectra were reported in Figure 76. The vinyl signals from the monomers appeared at 5.3 and 6.1 ppm and decreased in intensity as they were consumed in the production of polymer. Accordingly, the C-CH_3 signal from monomer at 1.9 decreased. As the polymerisation proceeded, signals of the methacrylate backbone grew, around 1 ppm (for C-CH_3) superimposed with butyl side groups signals, and with a broad peak around 2.1 ppm (for CH_2 in the main chain).

Thus, conversion was calculated from the integration of vinylic proton at 6.1 ppm ($I_{6.1\ t=x}$) at different reaction time, as obtained from the following equation, and plotted in Figure 77:

$$Conv = 1 - \frac{I_{6.1\ t=x}}{I_{6.1\ t=0}} \qquad \text{Eq. 22}$$

Kinetics plot for TBSiMA homopolymerisation showed a linear trend, at least up to 10 hours of polymerisation, corresponding to 80% of conversion, confirming the good control on chain growth of the RAFT chain transfer agent used.

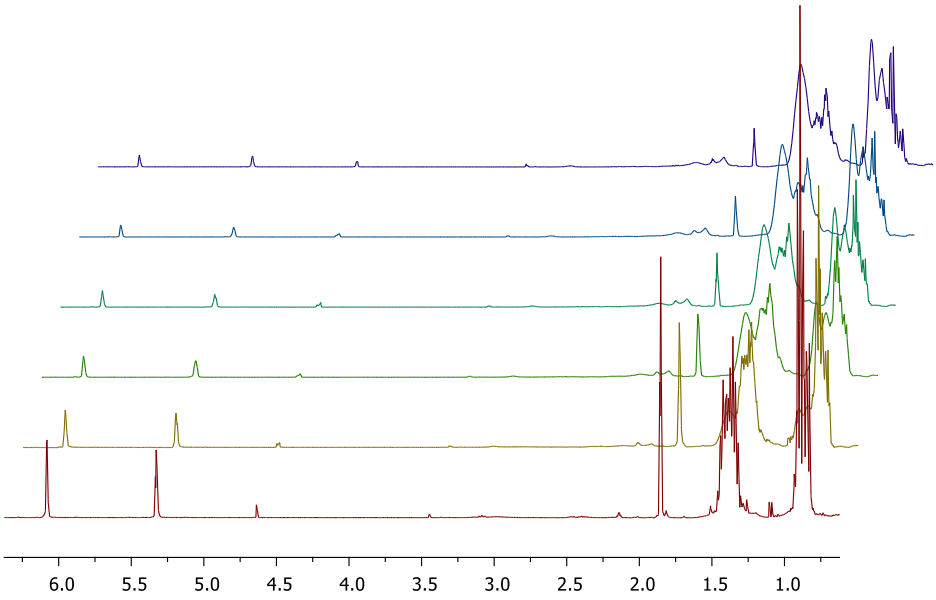

Figure 76: Selection of ^{1}H NMR spectra recorded during the homopolymerisation (at intervals of approximately 135 min from bottom to top) of TBSiMA with CDMP in toluene-d_8.

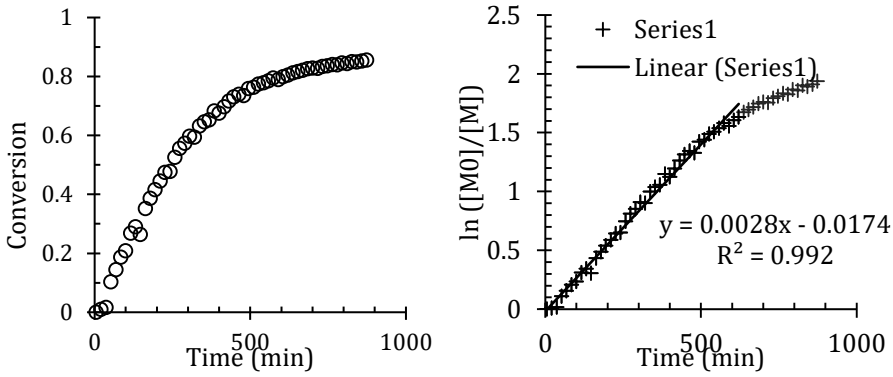

Figure 77: Conversion vs time (left) and kinetic plot (right) for TBSiMA *in situ* NMR monitored RAFT polymerisation with CDMP.

The integrated area of the broad signal arising at 2.1 ppm (corrected from a little contribution from t=0) allowed an estimation of number average molecular weight, calculated in the equation below, using the known molecular weight of the monomer MW_{mon} and the [monomer]:[CTA] = 35 molar ratio ($M_{n\ target}$ = 10000 g/mol).

$$Mn_{t=x} = MW_{mon}\frac{(I_{2.1\ t=x} - I_{2.1\ t=0})/2}{I_{6.1\ t=0}/35} \qquad \text{Eq. 23}$$

Experimental M_n values were compared in Figure 78 with the theoretical expected values, calculated for a well controlled RAFT reaction as a function of conversion p:

$$M_n = \frac{[Mon]_0\, MW_{mon}}{[CTA]_0}p + MW_{CTA} \qquad \text{Eq. 24}$$

where $[Mon]_0$ is the initial monomer concentration, MW_{mon} is the molecular weight of the monomer, p is the conversion, $[CTA]_0$ is the initial concentration of RAFT agent, and MW_{CTA} is the molecular weight of the RAFT agent.

Despite the unfortunate scattering of data points, a similar trend was observed for experimental and theoretical average molecular weights, with a more obvious deviation only at high conversions, when probably the incidence of termination reaction became more significant.

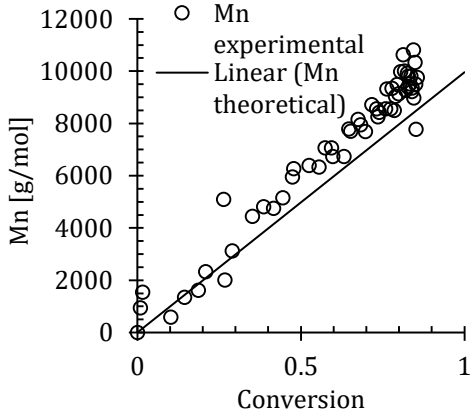

Figure 78: Number average molecular weight evolution vs conversion for TBSiMA *in situ* NMR monitored RAFT polymerisation with CDMP.

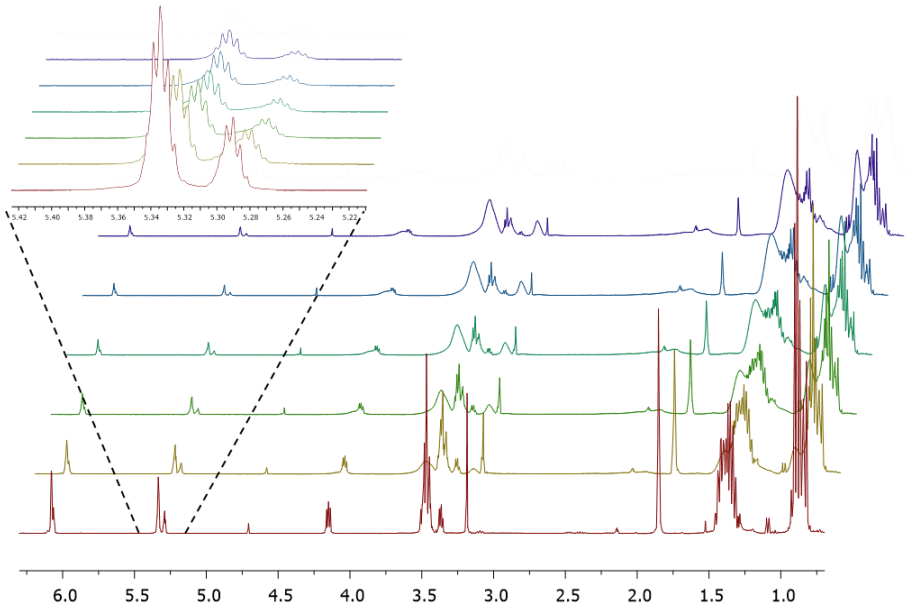

Figure 79: Selection of ^{1}H NMR spectra recorded during random copolymerisation (at intervals of approximately 135 min from bottom to top) of TBSiMA:PEGMA (70:30 molar ratio) with CDMP in toluene-d_8.

Analogous considerations and calculations were made for the *in situ* NMR monitored copolymerisation of TBSiMA and PEGMA. Similar reaction conditions were applied in these experiments, but different TBSiMA:PEGMA molar ratio were used (90:10, 70:30, 50:50, 30:70) for a $M_{n\ target}$ = 15000 g/mol. As representative example, the spectra of 70:30 reaction were shown in Figure 79. A differentiation of vinylic protons from TBSiMA and PEGMA at 5.34 and 5.29, respectively, offered the opportunity of detecting the depletion of the two monomeric species separately.

Kinetics plot for the two monomeric species, TBSiMA and PEGMA (Figure 80) showed a good control of the copolymerisation (up to 80% of conversion), and an almost simultaneous consumption of the two species, suggesting a random distribution of repeating units in the chain.

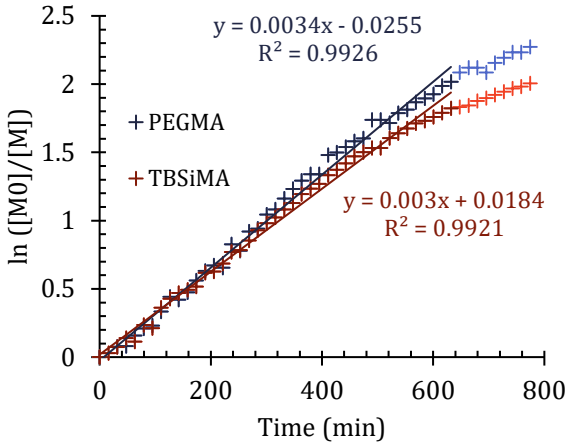

Figure 80: Kinetics plot for RAFT copolymerisation of the two monomers in TBSiMA:PEGMA 70:30 molar ratio reaction.

For polymerisation with a PEGMA content between 0 and 30% mol, at the end of the NMR experiment, it was possible to recover the product by precipitation of the reaction mixture in a large excess of methanol. Higher PEGMA contents made the copolymer soluble in methanol, but still difficult to precipitate in non-polar solvents such as n-hexane. TD-SEC analysis and accelerated hydrolysis experiments (see next paragraph) were carried out, when the amount of purified polymer was adequate.

The homopolymer was named pTBSiMA, and the copolymers TBSiMAx-*co*-PEGMAy where x and y represent the molar percentage of TBSiMA and PEGMA, respectively, in the feed of the polymerisation.

Narrow, symmetric peaks from Figure 81 and the relative low dispersity (M_w/M_n < 1.27, Table 26) confirmed the effective controlled character of both the homopolymerisation of TBSiMA, and its copolymerisation with PEGMA.

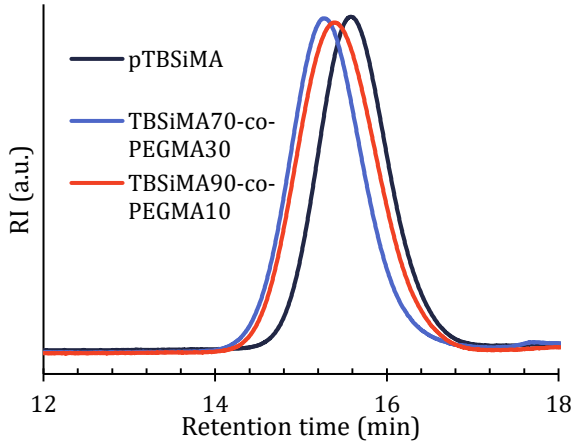

Figure 81: TD-SEC traces of pTBSiMA, TBSiMA70-*co*-PEGMA30 and TBSiMA90-*co*-PEGMA10.

Table 26: Physical-chemical characterisation of pTBSiMA and TBSiMAx-*co*-PEGMAy.

	pTBSiMA	***TBSiMA70-co-PEGMA30***	***TBSiMA90-co-PEGMA10***
M_n *(conv)*[b]	8500	13900	12600
M_n[a] *(g/mol)*	7200	12100	9800
M_w/M_n[a]	1.25	1.23	1.27

a Number average molecular weight and dispersity by TD-SEC in THF.
b Number average molecular weight determined by ^{1}H NMR, at final conversion.

A second set of *in situ* ^{1}H NMR monitored polymerisation were carried out to characterise TiPSiMA reactivity. Selected spectra of TiPSiMA homopolymerisation were reported in Figure 82. The vinyl signals from the monomers appeared at 5.3 and 6.1 ppm and decreased in intensity as they were consumed in the production of polymer. Accordingly, the C-CH_3 signal from monomer at 1.9 decreased. As the polymerisation proceeded, signals of the methacrylate backbone grew, at around 1 ppm (for C-CH_3) superimposed with isopropyl side groups signals, and with a broad peak around 2.4 ppm (for CH_2 in the main chain).

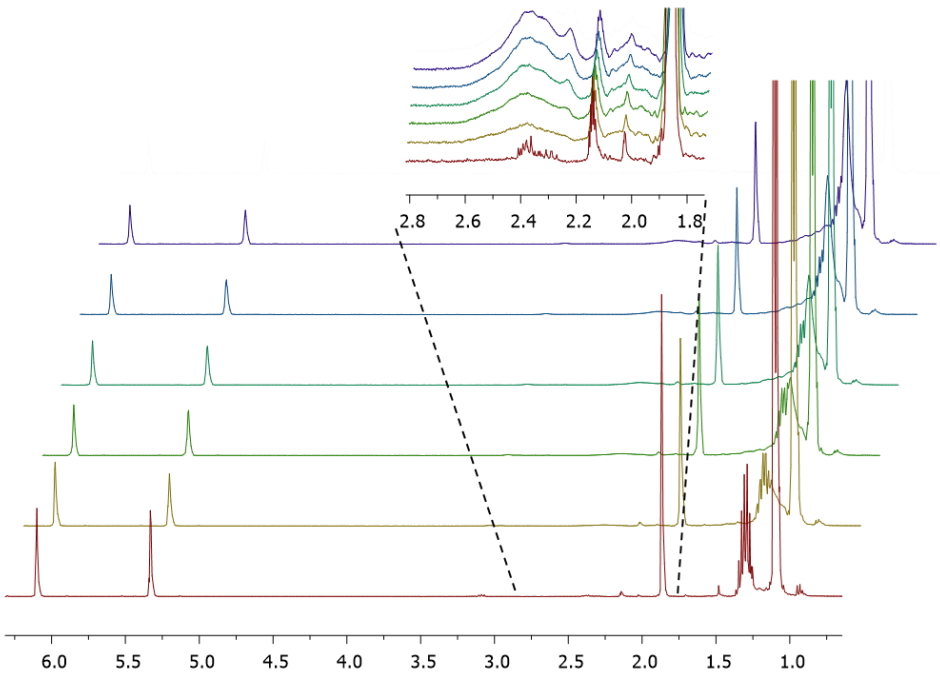

Figure 82: Selection of ^{1}H NMR spectra recorded during the homopolymerisation (at intervals of approximately 135 min from bottom to top) of TiPSiMA with CDMP in toluene-d_8.

Conversion vs time, first order kinetics plot and average molecular weight vs conversion are reported in Figure 83. TiPSiMA homopolymerisation with CDMP in toluene-d_8 at 70°C ($M_{n\ target}$ = 10000 g/mol) was much slower than TBSiMA homopolymerisation, giving 48% conversion in the observed 14.5 hours. As confirmed by the kinetics plot, the chain growth was well controlled by the RAFT system, and average molecular weight increased linearly, in excellent agreement with the theoretical trend expected.

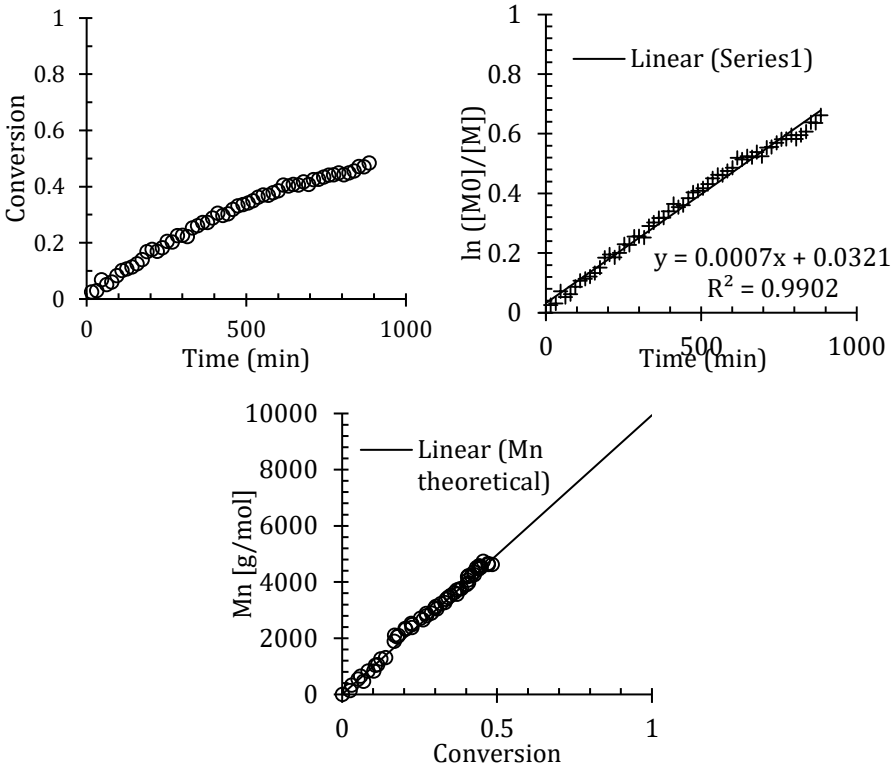

Figure 83: Conversion vs time (top left) and kinetic plot (top right) and number average molecular weight evolution vs conversion (bottom) for TiPSiMA *in situ* NMR monitored RAFT polymerisation with CDMP.

Subsequently, evaluations of *in situ* NMR monitored copolymerisation of TiPSiMA and PEGMA were performed. TiPSiMA:PEGMA molar ratios were used (90:10, 70:30, 50:50, 30:70) with a $M_{n\,\text{target}}$ = 15000 g/mol. The case of the 50:50 reaction will be discussed in detail. Polymerisation was observed for longer time (2.5 days), selected spectra were shown in Figure 84. A differentiation of vinylic protons from TiPSiMA and PEGMA, at 5.35 and 5.30, respectively, offered the opportunity of detecting the depletion of the two monomeric species separately, and showed a faster consumption of PEGMA with respect to TiPSiMA (Figure 85). Exact feed composition was 54% mol of TiPSiMA, while residual monomer was enriched in TiPSiMA up to 74% mol. Bulky isopropyl silyl ester proved to actually depress the monomer reactivity, providing slower kinetics, both in homopolymerisation and copolymerisation, compared with the TBSiMA and PEGMA system previously analysed.

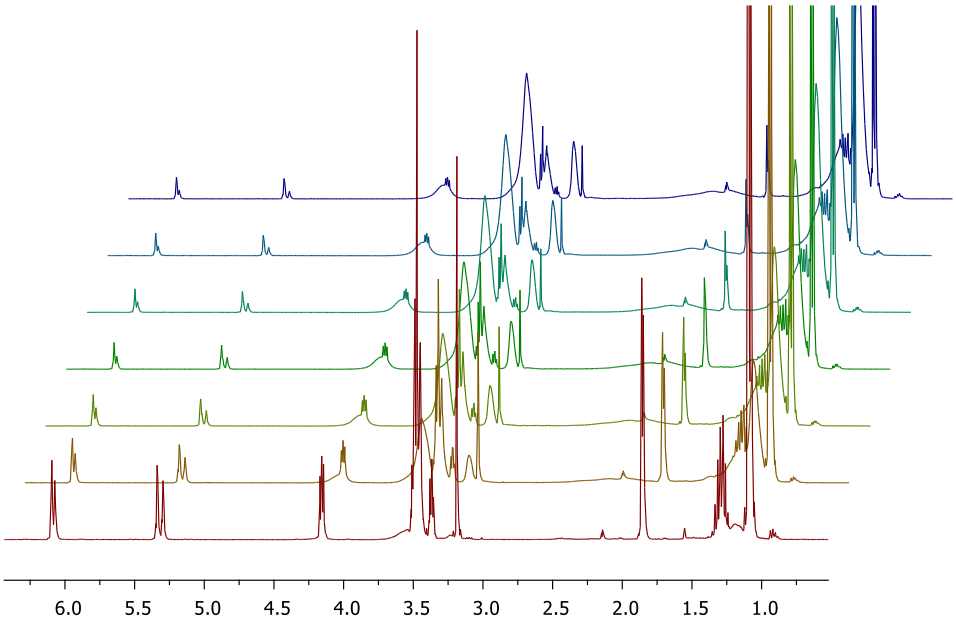

Figure 84: Selection of ^{1}H NMR spectra recorded during random copolymerisation (at intervals of approximately 6.5 hours from bottom to top) of TiPSiMA:PEGMA (50:50 molar ratio) with CDMP in toluene-d_8.

A good control on copolymerisation was maintained up to 770 minutes, at 67% of total conversion, corresponding to 60% and 73% conversions for TiPSiMA and PEGMA, respectively (Figure 85).

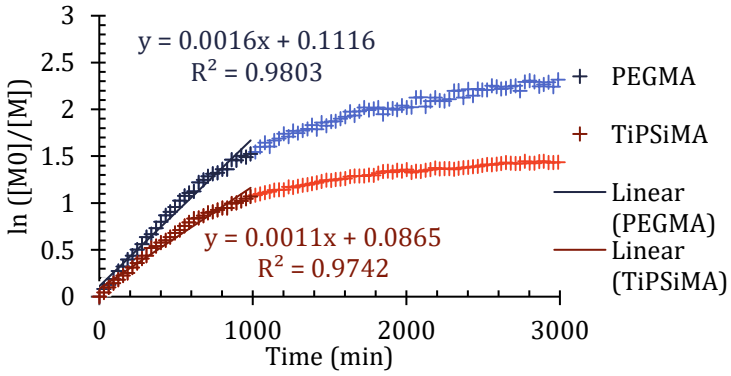

Figure 85: Kinetics plot for RAFT copolymerisation of the two monomers in TiPSiMA:PEGMA 50:50 molar ratio reaction.

Chain growth linearly varied with conversion, good agreement was observed between experimental and theoretical average degree of polymerisation, with a more obvious deviation at conversions higher than 70%, when probably the incidence of termination reaction became more significant (Figure 86).

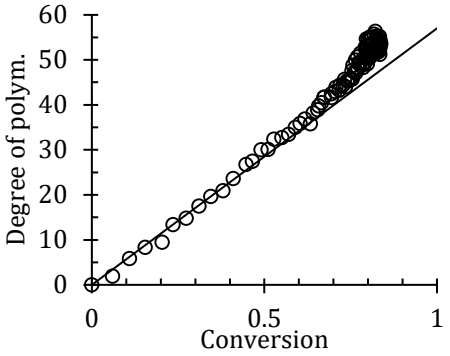

Figure 86: Average degree of polymerisation evolution vs conversion for TiPSiMA:PEGMA (50:50 mol) *in situ* NMR monitored RAFT polymerisation with CDMP.

Unfortunately, the low polymerisation yield did not provide sizeble amount of purified polymer to be submitted to TD-SEC analysis.

Finally, reactivity ratio (r_1 and r_2) were calculated from the ^{1}H NMR data. F_1 and F_2 were used to define molar fraction of comonomers in the copolymer, and f_1 and f_2 were used for molar fraction of monomer in the feed. Index 1 was used for PEGMA and 2 for TRSiMA. Well known Kelen-Tudos and Fineman-Ross methods were applied. Moreover, curve fitting of the instantaneous form of the copolymerisation equation (Eq. 25), expressed in terms of mole fraction, allowed to evaluate r_1 and r_2 values using least square analysis.

$$F_1 = \frac{r_1 f_1^2 + f_1 f_2}{r_1 f_1^2 + 2 f_1 f_2 + r_2 f_2^2} \qquad \text{Eq. 25}$$

Reactivity ratios for monomers TBSiMA and PEGMA were reported in Table 27. Both reactivity ratios were smaller than 1, thus demonstrating that the two monomers had a higher tendency to cross-polymerise than to add a second identical unit. Moreover, such a pair displayed an azeotropic composition (Figure 87), where feed molar fraction and polymer molar fraction are the same (F_1=f_1=0.35). The higher r_2 value should lead to a higher probability of formation longer sequences of TBSiMA in the copolymers.

Table 27: Reactivity ratios for the TBSiMA and PEGMA pair of monomers, with different methods.

	r₁ PEGMA	***r₂ TBSiMA***
Kelen-Tudos	0.35	0.61
Finemann-Ross	0.48	0.71
Fit	0.46	0.71

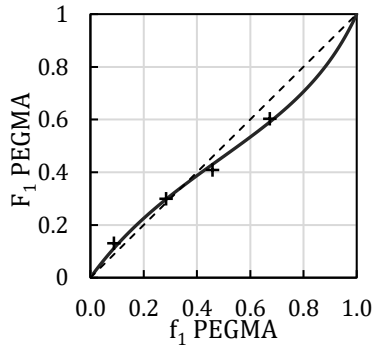

Figure 87: Copolymerisation equation resulting from best fit value of r_1 and r_2 for TBSiMA and PEGMA RAFT copolymerisation in the presence of CDMP.

Reactivity ratios for monomers TiPSiMA and PEGMA were reported in Table 28. Higher $r_1 > 1$ indicated that PEGMA terminated chains were likely adding a PEGMA unit again, while $r_2 < 1$ showed the higher tendency to crosspolymerise of TiPSiMA units. $r_1\ r_2 \approx 1$ suggested that the copolymerisation tended to the ideal random incorporation of monomers, but being $r_1 > r_2$ PEGMA was more reactive towards both TiPSiMA and PEGMA terminated chains, resulting in a copolymer always enriched in PEGMA units (Figure 88).

Table 28: Reactivity ratios for the TiPSiMA and PEGMA pair of monomers, with different methods.

	r₁ PEGMA	***r₂ TiPSiMA***
Kelen-Tudos	1.42	0.70
Finemann-Ross	1.65	0.85
Fit	1.50	0.82

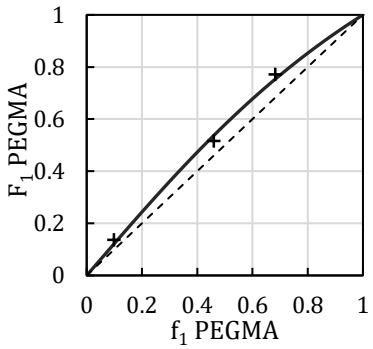

Figure 88: Copolymerisation equation resulting from best fit value of *r*1 and *r*2 for TiPSiMA and PEGMA RAFT copolymerisation in presence of CDMP.

3.1.1.2 Macro chain-transfer agent synthesis

CDMP was proved to be effective in the control of the polymerisation of TBSiMA and TiPSiMA whether alone and along PEGMA. Therefore, it was selected for the continuation of this study, and it was used for the preparation of a macromolecular PDMS-based chain transfer agent, taking advantage of its carboxylic acid functionality. This macro-CTA for RAFT polymerisation was synthesised by Steglich esterification of a commercial monohydroxyl-terminated poly(dimethylsiloxane) (PDMS-OH) with the carboxylic acid end-functionalised trithiocarbonate RAFT agent CDMP (Scheme 16).[111] In detail, a molar ratio of reactive agents [PDMS-OH]:[CDMP]:[DCC]:[DMAP] of 1:1.5:2:0.2 was used. A dropwise addition of both CDMP and DCC solutions at room temperature, followed by 15 hours of dichloromethane reflux resulted in complete conversion of PDMS-OH. Product formation was confirmed by ^{1}H NMR disappearance and shift of the methylene protons adjacent to the hydroxyl group of the PDMS chain, from approximately 3.73 ppm to 4.25 ppm. The final product was named PDMS-CTA.

The number of dimethylsiloxane repeating units per chain and number-average molecular weight was estimated by ^{1}H NMR spectra from the CH_3 groups in dimethylsiloxane chain peak at 0.08 ppm and the ester CH_2 group at 4.25 ppm. SEC traces in toluene showed a narrow, monomodal distribution (Figure 89). From calibration with PMMA standards number average molecular weight of M_n = 5800 g/mol with M_w/M_n = 1.1 dispersity were evaluated. These values were in

good agreement with the M_n calculated from ^{1}H NMR (M_n = 5400, corresponding to 65 dimethylsiloxane repeating units). Moreover, the integration of the peak of methylene protons adjacent to the trithiocarbonate at 3.25 ppm and the integration of the peak at 4.25 ppm have similar values, confirming that there was only one RAFT chain transfer agent group per PDMS chain without residual unreacted CDMP.

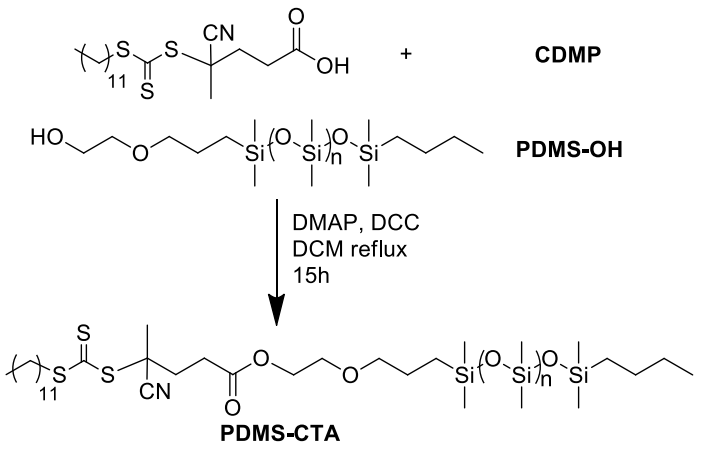

Scheme 16: Steglich esterification of CDMP and PDMS-OH to obtain the macromolecular chain transfer agent (PDMS-CTA).

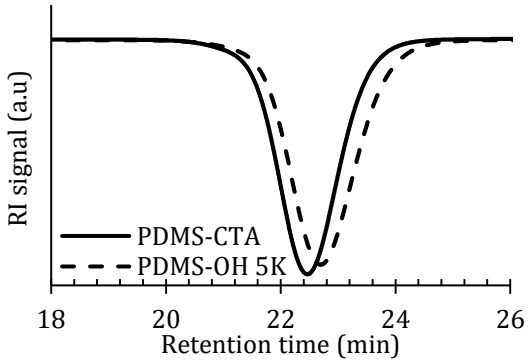

Figure 89: SEC curve of purified PDMS-CTA compared with its PDMS-OH precursor in toluene.

3.1.1.3 Synthesis of PDMS-based diblock copolymers

Amphiphilic hydrolysable block copolymers to be used as surface-active additives in polydimethylsiloxane marine coatings were synthesised via RAFT polymerisation. Two different series of copolymers were designed, with an architecture depicted in Figure 90. PDMS-based macro-CTA described in the previous paragraph became the first block, with a hydrophobic character and optimal compatibility with the PDMS network where the copolymer would be dispersed later on. A second block was attached via RAFT polymerisation, composed of a hydrolysable TRSiMA, either alone or copolymerised with hydrophilic PEGMA. The cleavage of the labile silyl ester bond in contact with water would increase the hydrophilicity of the second block, eventually leading to a completely water-soluble block.

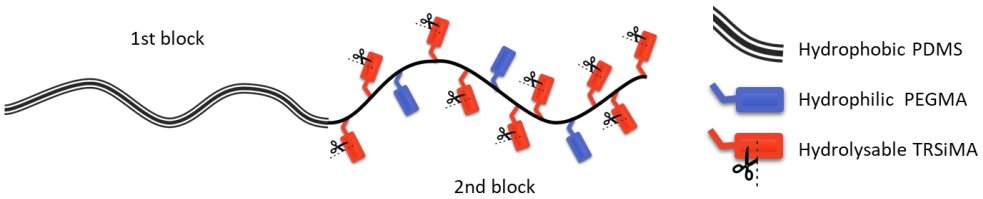

Figure 90: Schematic representation of amphiphilic hydrolysable block copolymer design.

Kinetics of CDMP mediated RAFT polymerisation of trialkylsilyl methacrylates (TBSiMA and TiPSiMA) and PEGMA was extensively studied by *in situ* NMR monitoring, with successful control on polymerisation. Thus, monomer concentration and molar ratio of macro-CTA:AIBN were fixed at 1.5 M and 5:1, respectively, and the reaction was carried out in anhydrous toluene at 70°C (Scheme 17 and Scheme 18). The macro-RAFT agent PDMS-CTA concentration was estimated, for every polymer, from a given target M_n value of the second block, at 100% of monomer conversion:

$$M_n = \frac{[Mon]_0 \, MW_{mon}}{[CTA]_0} p + MW_{CTA} \qquad \text{Eq. 26}$$

where $[Mon]_0$ is the initial monomer concentration, MW_{mon} is the molecular weight of the monomer, p is the conversion, $[CTA]_0$ is the initial concentration of macro-RAFT agent, and MW_{CTA} is the molecular weight of the PDMS-CTA. Relevant reaction conditions were reported in Table 29.

Copolymer composition was determined by ^{1}H NMR from characteristic signals. The signal relative to $Si(CH_3)_2$ for the PDMS block was identified, at 0.1 ppm. The signals from $COOCH_2$ and OCH_3, at 4.1 and 3.4 ppm, respectively, were assigned to PEGMA units. TBSiMA content was evaluated from $[C\underline{H}_2(CH_2)_2CH_3]_3$ of the butyl groups, at 0.7 ppm. For TiPSiMA copolymers, the composition was calculated from the signal at 1.1 ppm relative to the methacrylic methyl $CH_2C(\underline{CH}_3)$ and $Si[CH(\underline{CH}_3)_2]_3$ methyl characteristic of the TiPSiMA units. A correction was made for the contribution of PEGMA to $CH_2C(C\underline{H}_3)$ in main chain, on the signal at 1.1 ppm of copolymers containing both methacrylic units.

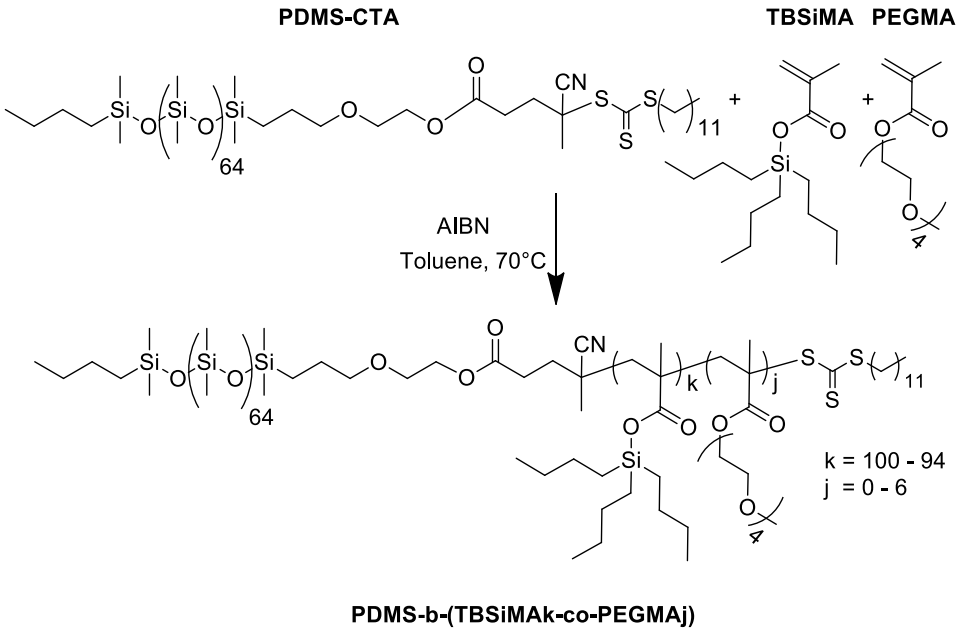

Scheme 17: Synthesis of amphiphilic hydrolysable copolymer via RAFT copolymerisation of TBSiMA and PEGMA.

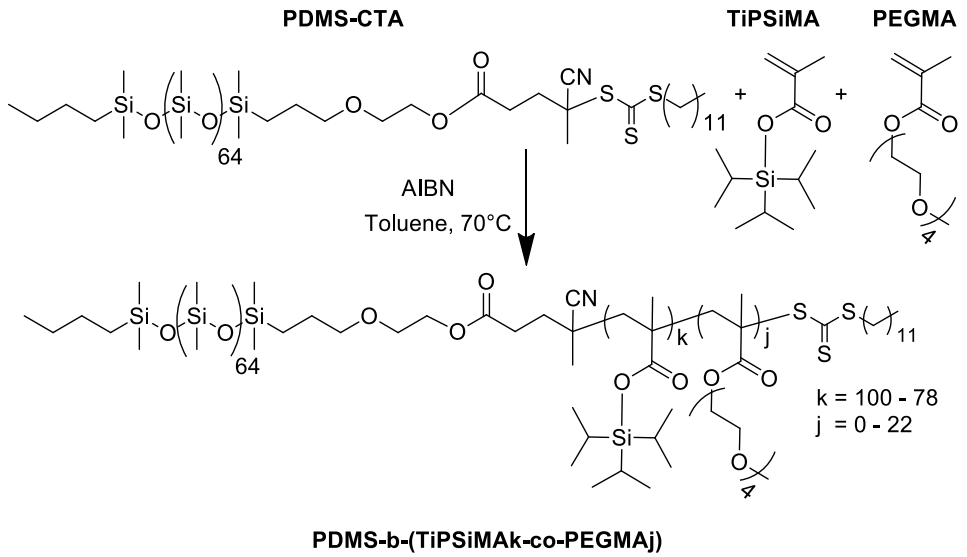

Scheme 18: Synthesis of amphiphilic hydrolysable copolymer via RAFT copolymerisation of TiPSiMA and PEGMA.

Table 29: Reaction conditions for RAFT polymerisation of PDMS-*co*-TRSiMA and PDMS-*b*-(TRSiMAk-*co*-PEGMAj) copolymers.

Copolymer	***$M_{n\ target}$[a] (g/mol)***	***Conv[b]***	***DMS[c] (%mol)***	***TRSiMA[d] (%mol)***	***PEGMA[e] (%mol)***
PDMS-b-TBSiMAa	15000	0.95*	65	35	--
PDMS-b-TBSiMAb	20100	0.92*	55	45	--
PDMS-b-(TBSiMA94-co-PEGMA6)	23600	0.90*	50	45	5
PDMS-b-TiPSiMA	15400	0.77+	60	40	--
PDMS-b-(TiPSiMA89-co-PEGMA11)	24200	0.78+	45	50	5
PDMS-b-(TiPSiMA78-co-PEGMA22)	24100	0.78+	45	40	15

a Target M_n used in Eq. 24.
b Final conversion determined by ^{1}H NMR after 24 hours (*), or 48 h (+).
c Molar percentage of DMS repeating units in PDMS-CTA, with respect to the monomers in the feed.
d Molar percentage of TRSiMA monomer in the feed.
e Molar percentage of PEGMA monomer in the feed.

Block copolymers PDMS-*b*-TiPSiMA and PDMS-*b*-TBSiMAn were synthesised, without the hydrophilic PEGMA units. The letter *n* = *a* or *b* was used to differentiate the copolymers with different length of the second block. Copolymers with the mixed second block were named PDMS-*b*-(TRSiMAk-*co*-PEGMAj), where *k* and *j* referred the mole percentage contents in the second block of the TRSiMA and PEGMA repeating units, respectively.

The RAFT polymerisation of TBSiMA, either alone or along with PEGMA, was found to proceed with high monomer conversion (≥ 92% after 24 hours, when the reaction was stopped). TiPSiMA reactivity, as already shown in the previous paragraph, was deeply affected by the noteworthy steric hindrance of the tri-isopropyl moieties linked to the silicon atom. Thus, for TiPSiMA, conversions were around 77% when the reaction was stopped after 48 hours.

Purified polymers were analysed by TD-SEC in THF to determine their d*n*/d*c* value and consequently their absolute molecular weights (Table 30). TD-SEC traces, reported in Figure 91, displayed narrow, monodisperse peaks, corresponding to average molecular weight distribution with M_w/M_n between 1.11 and 1.20.

Table 30: Physical-chemical properties PDMS-based block copolymers.

Copolymer	***M_n[a] (g/mol)***	***M_w/M_n[a]***	***TRSiMA[b] (%mol)***	***PEGMA[c] (%mol)***
PDMS-b-TBSiMAa	15800	1.17	32	--
PDMS-b-TBSiMAb	22400	1.18	40	--
PDMS-b-(TBSiMA94-co-PEGMA6)	23800	1.18	39	3
PDMS-b-TiPSiMA	17700	1.11	35	--
PDMS-b-(TiPSiMA89-co-PEGMA11)	24500	1.20	44	5
PDMS-b-(TiPSiMA78-co-PEGMA22)	24000	1.19	33	10

a Number average molecular weight and dispersity by TD-SEC in THF.
b Molar percentage of TBSiMA or TiPSiMA repeating units in the copolymer, determined by ^{1}H NMR.
c Molar percentage of PEGMA repeating units in the copolymer, determined by ^{1}H NMR.

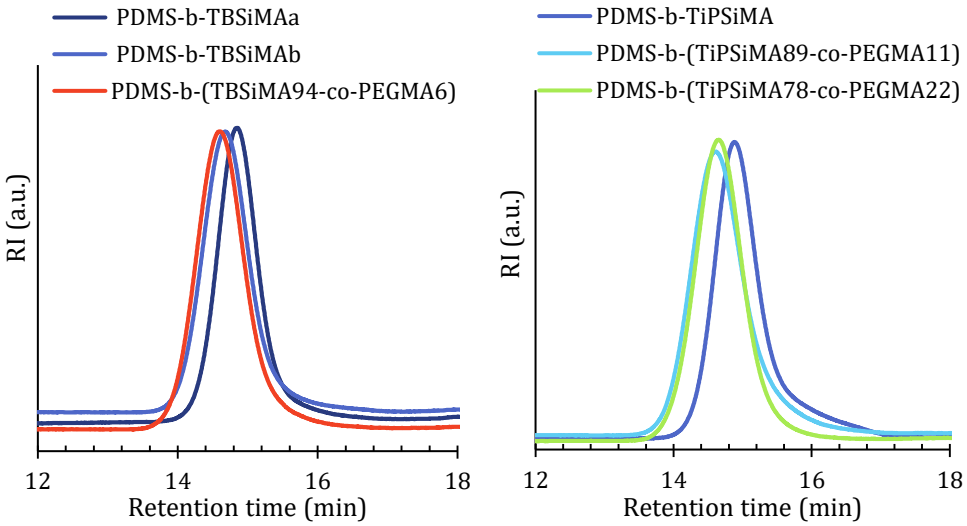

Figure 91: TD-SEC traces of PDMS-*b*-(TBSiMAk-*co*-PEGMAj) (left) and PDMS-*b*-(TiPSiMAk-*co*-PEGMAj)(right) in THF.

3.1.2 Hydrolysis kinetics of trialkylsilyl methacrylate copolymers

The hydrolysis kinetics of hydrolysable polymers based on tri-isopropylsilyl (meth)acrylate (TiPSi(M)A), tert-butyldimethylsilyl (meth)acrylate (TBDMSi(M)A), and tri-butylsilylmethacrylate (TBSiMA) was investigated by ^{1}H NMR spectroscopy in THF-d_8 as already reported in the literature.[116,117] These polymers, which are initially water-insoluble, could be solubilised by a hydrolysis reaction in contact with acidic or basic water. The hydrolysis of the ester bond leads to a polymer backbone bearing carboxylic acid or carboxylate side groups and a non-toxic R_3SiCl side product.[118] This latter tends to form siloxane-based compounds through hydrolysis as depicted in Scheme 19.

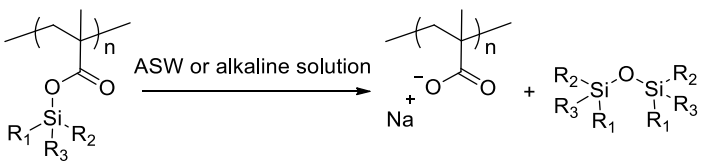

Scheme 19: Hydrolysis of trialkylsilyl methacrylic polymers in seawater or alkaline solution.

Generally, the silyl ester bond in the monomer species seems to have higher reactivity, that is enhanced through an electronic-accepting effect of the double bond. On the contrary, the macromolecular chain length of the polymer seems to limit the hydrolysis of the silyl ester side groups, through a steric hindrance effect. Moreover, a large range of hydrolysis kinetic rates were obtained depending on the structure of the hydrolysable moiety. Thus, an effect of the alkyl groups linked to the silicon atom was revealed. In the case of poly(tri-alkylsilyl (meth)acrylate)s with a noteworthy steric hindrance, such as the tri-isopropyl moiety, the lowest hydrolysis rates were observed. Intermediate hydrolysis rates were observed for TBSiMA.

The addition of a hydrophilic or hydrophobic comonomer to a silylated-based copolymer is another powerful tool to adjust hydrolysis kinetics, affecting initial polymer water solubility, and water diffusion to the cleavable bonds. It could also serve to improve other coating properties, such as mechanical stability and capacity of film formation. To prove this, in this work, the kinetics of hydrolysis of the silylated side groups of TBSiMA and TiPSiMA based polymers were investigated through the assessment of the molar percentage of non-hydrolysed silyl ester groups, by ^{1}H NMR analysis, in THF-d_8 solutions mixed with an aliquot of pH 10 ammonia buffer or artificial sea water.

Figure 92 showed a comparison of the hydrolysis, with pH 10 buffer, of TBSiMA homopolymer, and copolymers containing hydrophilic PEGMA comonomer or hydrophobic PDMS block. pTBSiMA and TBSiMAx-*co*-PEGMAy had a similar fast degradation profile, going to complete hydrolysis in about seven days. Initial reaction rate was faster with increasing PEGMA content, leading to 10%, 20% and 24% non-hydrolysed silyl esters after 24 hours in TBSiMA70-*co*-PEGMA30, TBSiMA90-*co*-PEGMA10 and pTBSiMA, respectively. Distinctly, PDMS-*b*-TBSiMAb copolymer presented a higher chemical stability in alkaline solution, with still 39% of non-hydrolysed silyl ester groups after the first day of degradation, and showing a slower hydrolysis profile during all the experiment.

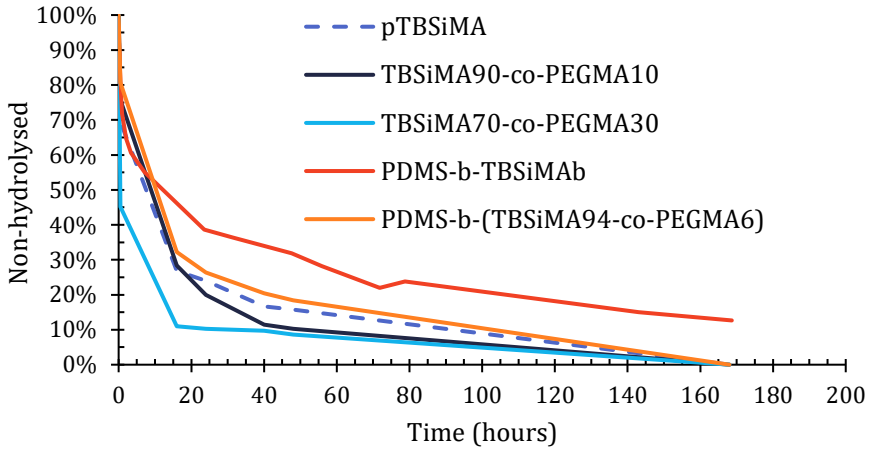

Figure 92: Evolution of the proportion of non-hydrolysed monomer units of several TBSiMA based polymer solutions in THF-d_8 with pH 10 buffer.

In copolymer PDMS-*b*-(TBSiMA94-*co*-PEGMA6) the stabilising effect of hydrophobic PDMS block and accelerating effect of hydrophilic PEGMA compensated each other and yielded a degradation profile intermediate between those of PDMS-*b*-TBSiMAb and TBSiMA90-*co*-PEGMA10.

TiPSiMA based copolymers displayed a greater chemical stability in alkaline solution, with pH 10 ammonia buffer (Figure 93). After 10 days of monitoring, 41 to 11% of non-hydrolysed silyl ester moieties were still present by ^{1}H NMR analysis. PDMS-*b*-TiPSiMA exhibited the slowest hydrolysis profile, with 86% of non-hydrolysed units after one day, more than twofold the value of the analogue PDMS-*b*-TBSiMAb. This confirmed the intrinsic lower hydrolysis rate of the sterically hindered triisopropyl silyl ester compared with tributyl silyl one. Adding the hydrophilic PEGMA comonomer enhanced TiPSiMA hydrolysis. Surprisingly, including more than 11% mol of PEGMA counits did not accelerate the degradation proportionally and PDMS-*b*-(TiPSiMA78-*co*-PEGMA22) maintained a hydrolysis profile almost superimposable to those of PDMS-*b*-(TiPSiMA89-*co*-PEGMA11).

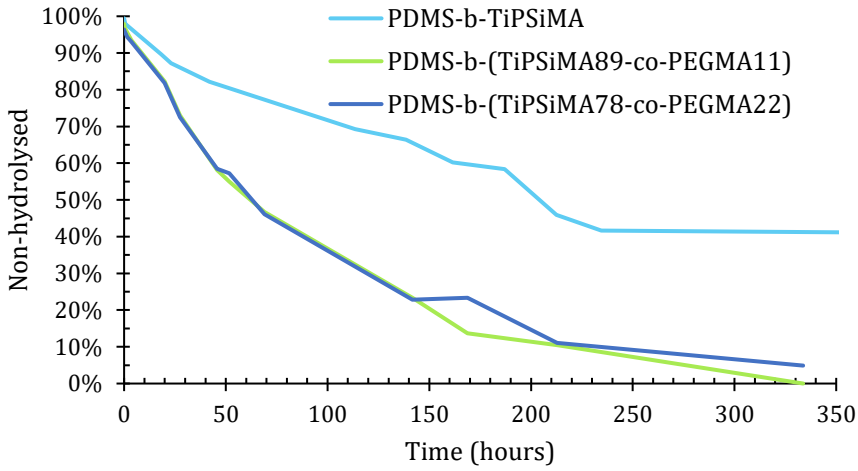

Figure 93: Evolution of the proportion of non-hydrolysed monomer units of several TiPSiMA based polymer solutions in THF-d_8 with pH 10 buffer.

Finally, in Figure 94, degradation profiles of selected copolymer solutions containing an aliquot of artificial sea water (ASW, pH 8.2 in accordance with ASTM D1141-98R13 standard) were compared to the corresponding solution with pH 10 ammonia buffer.

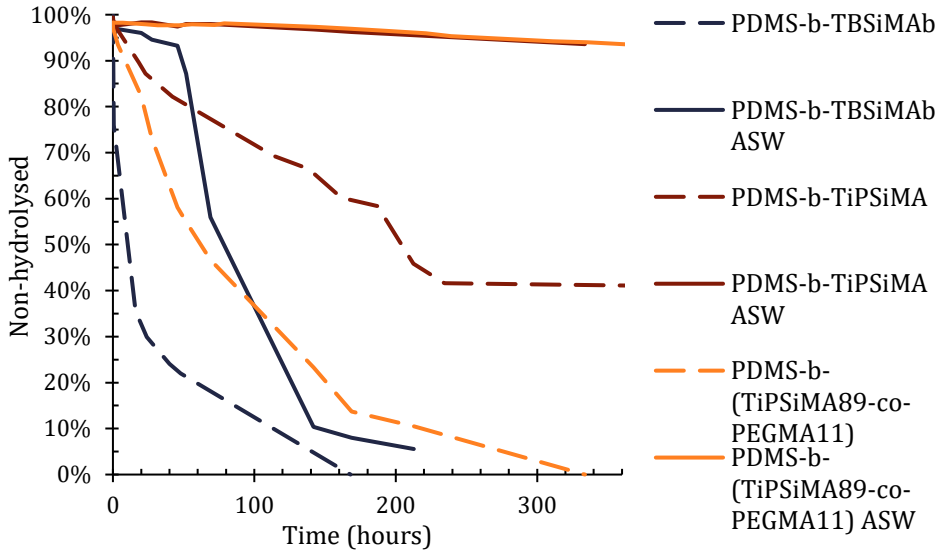

Figure 94: Evolution of the proportion of non-hydrolysed monomer units of selected TBSiMA and TiPSiMA based polymer solutions in THF-d_8 with pH 10 buffer and ASW.

PDMS-*b*-TBSiMA sample with ASW showed an induction period with little hydrolysis (93% non-hydrolysed groups after 46 h), which then substantially dropped to almost complete hydrolysis in about 160 hours, that is a time interval consistent with the degradation in contact with pH 10 buffer. TiPSiMA based copolymers, whose higher stability was already noted, exposed to less aggressive ASW (pH 8.2) produced only little hydrolysis, up to 93% non-hydrolysed ester groups after 15 days of observation. No significative differences were noted in the sample containing the hydrophilic comonomer PEGMA.

3.1.3 Film preparation

In order to study the surface properties and to evaluate antifouling properties with marine organisms in laboratory assay or field immersion, copolymer films in blend with a PDMS elastomeric matrix were prepared, according to the design depicted in Figure 95.

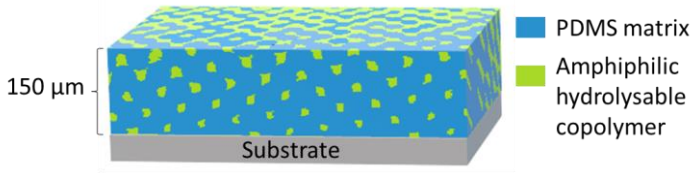

Figure 95: Schematic representation of film geometry.

The PDMS crosslinking reaction was performed by a sol-gel condensation cure reaction, reported in Scheme 20. Initial hydrolysis of labile ethoxy groups in poly(diethoxysiloxane) crosslinker (named ES40) started the condensation reactions with analogous Si-OH in ES40 and in disilanol terminated polydimethylsiloxane (HO-PDMS-OH) or to transesterify with residual Si-O-Et in ES40. A catalyst is needed to carry out film crosslinking, especially at room temperature. Synthesised amphiphilic hydrolysable copolymers were mixed to the matrix precursors in ethyl acetate solution before the addition of the catalyst, then the formulation was cast on the substrate of choice (clean glass slides or sandblasted PVC). Thus, the polymeric amphiphilic hydrolysable additive was only dispersed in the network of the matrix, stabilised by the PDMS

block that acted as a compatibiliser, without any covalent bond impeding the diffusion.

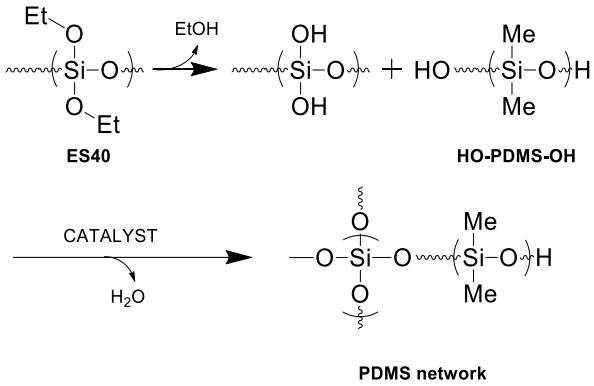

Scheme 20: PDMS crosslinking reaction scheme.

A typical formulation is reported in Table 31. A fixed amount of hydrolysable copolymer additive was used in every model coating (10% wt relative to PDMS). Initially, two catalysts were considered: tributyl ammonium fluoride (TBAF) and dioctyl tin dilaurate (TIB KAT 216).

Table 31: Solution blend formulation used to cast polymeric film coatings.

	Formulation	
Ethyl acetate	0.5 ml	50% vol/wt
HO-PDMS-OH	1 g	100% wt
ES40	25 mg	2.5% wt
Catalyst	10 mg	1% wt
Copolymer additive	100 mg	10% wt

In a recent work from our group, TBAF catalysed gel formation was proved to be very rapid at room temperature, reaching complete conversion in 24h with only 0.08 wt% catalyst content.[119] Moreover, ecotoxicological studies with *Vibrio fischeri* bacterium and the *Dunaliella tertiolecta* alga were carried out on the leachates of the TBAF catalysed PDMS films, demonstrating its lower

environmental impact with respect to other catalytic systems based on metals (tin or bismuth).[119]

Surprisingly, the formulations containing TBAF catalyst (from 0.08% to 0.5% wt) and amphiphilic hydrolysable copolymers of this work did not yield a complete sol-gel condensation, even after several days at room temperature and thermal curing at 120°C for 12 hours. A secondary reaction of TBAF with the trithiocarbonate moiety brought by the RAFT chain transfer agent was hypothesised. This was confirmed by UV-vis spectroscopy investigations. UV-vis spectra of 0.001 M solution of PDMS-CTA in ethyl acetate were acquired after the addition of one equivalent of TBAF. The characteristic trithiocarbonate band at 298 nm decreased in intensity, while a second band appeared at 350 nm.

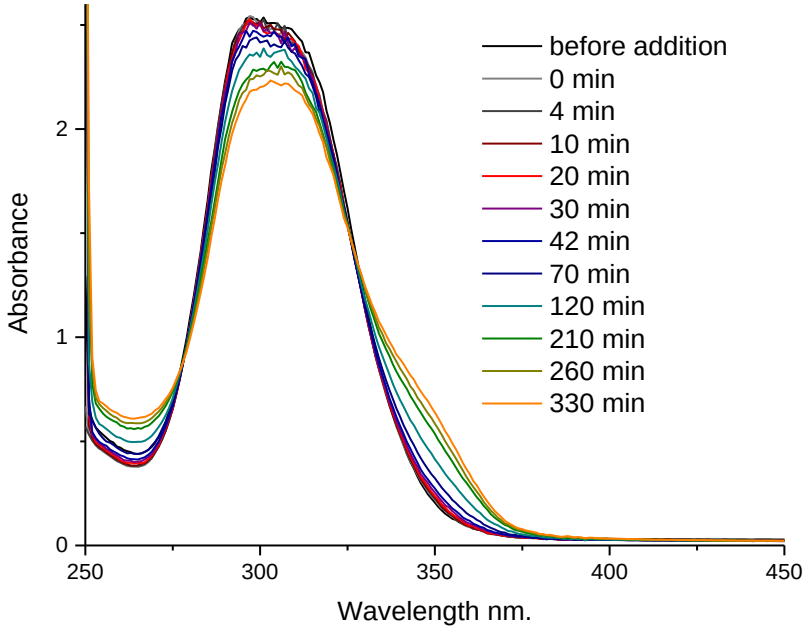

Figure 96: UV-vis spectra of PDMS-CTA:TBAF solution 1:1 mol in ethyl acetate, in 6 hours.

Therefore, 1% wt of a dioctyl tin dilaurate based catalyst (TIB KAT 216) was used. In this case, UV-vis spectroscopy measurements did not evidence any secondary reaction of the trithiocarbonate chain transfer agent (Figure 97).

All the formulations were successfully crosslinked at room temperature, after 1 to 4 days, to allow solvent evaporation and gel formation. Carboxylate moieties

on polymer chain, from little amount of hydrolysed repeating units, could chelate the metal centre of the catalyst, limiting its accessibility for the sol-gel process. To obtain a reasonably rapid crosslinking reaction, the highest amount of catalyst (1% wt) in the range recommended by the manufacturer was used.

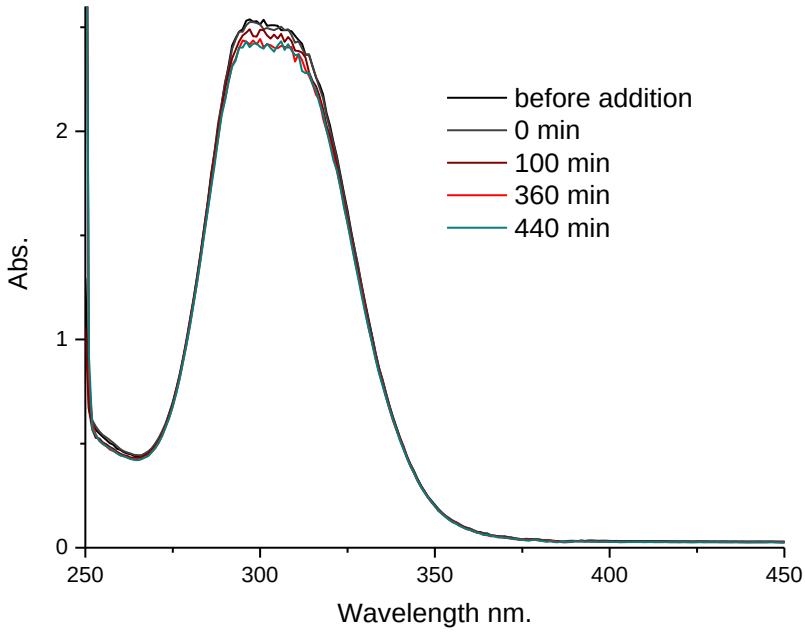

Figure 97: UV-vis spectra of PDMS-CTA:TIB KAT 216 solution 1:1 mol in ethyl acetate, in 6 hours.

Films were cast for every synthesised copolymer, all containing the same amount of copolymer additive (10% wt). Films were named as the added copolymer, as detailed in the following discussion. Blank films of PDMS matrix without any additive were prepared, and tested in the same conditions. While PDMS matrix was generally transparent, films containing the copolymer additive were translucent, but very homogenous (see Figure 98, as an example). No macroscopic phase separation was observed in time.

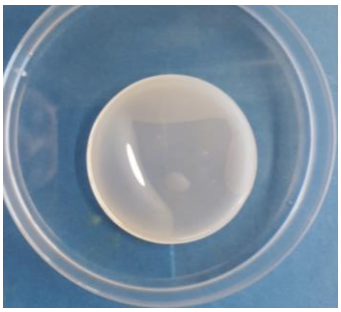

Figure 98: PDMS-*b*-(TBSiMA94-*co*-PEGMA6) in PDMS matrix, freestanding film in a Petri dish.

3.1.4 Wettability and surface free energy

Static contact angle measurements were performed with the sessile drop method on polymer blended films (150 µm thickness) prepared from the solution casting on clean glass slides. Deionised water and diiodomethane were used as interrogating liquids, in order to obtain contact angle values (θ), which were used for the calculation of polymer surface free energy according to the additive component approach from Owens, Wendt and Kaeble.

The values of θ with water and diiodomethane (Table 32) could be regarded as estimations of hydrophobicity (θ_w > 90°) and lipophobicity (θ_{di} > 60°), respectively. According to this criterion all the blend films resulted to be both hydrophobic (θ_w ≥ 108°) and lipophobic (θ_{di} ≥ 67°). Generally lower contact angle values were measured for the PDMS matrix without any copolymer additive (θ_w = 104°, θ_{di} = 67°). These results suggested that the hydrophobic character could rise from the close packing of the pendant methyl groups of the flexible siloxane chain and alkylsilyl moieties at the film-air interface.

Values of surface free energy (γ_s), calculated with Owens Wendt and Kaeble additive method, were reported in Table 32, along with the respective dispersive component (γ_s^d), that originates mainly from molecular interactions due to London forces, and polar component (γ_s^p) due to both hydrogen bonding and dipole-dipole interactions. All the films, containing the hydrolysable copolymer additive, displayed low surface energy, (15-25 mN/m), similar or slightly lower than the PDMS matrix alone. Surprisingly, the polar contribution γ_s^p to surface free energy is almost negligible in every case, including the

polymer blends containing PDMS-*b*-(TRSiMAk-*co*-PEGMAj) copolymers. For these copolymers the oxyethylene side chains was expected to add a significant polar contribution to surface energy. Thus, supposedly, oxyethylene side chains were not available at the polymer-liquid interface, but were buried underneath the surface of the coating.

For water immersed films containing silylester-based polymers, θ_w decreased with immersion time, as the hydrophilic character of the coating surfaces increased with time (Figure 99). This result agreed with the expected hydrolysis reaction of the hydrophobic silyl ester groups of TRSiMA units into hydrophilic carboxylate groups in presence of water. Furthermore, the surface of the PDMS-based coating remained quite hydrophobic (θ_w = 102°-97° after 30 days of immersion), except for the film containing PDMS-*b*-TBSiMAb (final θ_w = 85°), that was the polymer with a high content of rapidly hydrolysable TBSiMA units.

Table 32: Static contact angle with water and diiodomethane on PDMS blends. Surface free energies and their components calculated with Owens Wendt and Kaeble method.

Film	θ_w (°)	θ_{di} (°)	γ_s (mN/m)	γ_s^d (mN/m)	γ_s^p (mN/m)
PDMS	104.2 ±0.9	66.7 ±1.9	25.0 ±1.5	24.6 ±1.3	0.4 ±0.2
PDMS-b-TBSiMAa	123.6 ±0.2	86.9 ±1.2	15.3 ±0.7	15.3 ±0.7	0.08 ±0.03
PDMS-b-TBSiMAb	113.6 ±0.4	73.5 ±1.0	21.9 ±0.7	21.9 ±0.7	0 ±0
PDMS-b-(TBSiMA94-co-PEGMA6)	122.3 ±1.1	79.0 ±2.5	20.2 ±1.8	19.9 ±1.6	0.3 ±0.2
PDMS-b-TiPSiMA	107.7 ±0.4	67.0 ±0.3	25.2 ±0.2	25.2 ±0.2	0.07 ±0.02
PDMS-b-(TiPSiMA89-co-PEGMA11)	108.6 ±0.3	68.4 ±0.2	24.5 ±0.2	24.4 ±0.1	0.06 ±0.01
PDMS-b-(TiPSiMA78-co-PEGMA22)	109.0 ±0.4	68.6 ±0.3	24.4 ±0.2	24.3 ±0.2	0.05 ±0.02

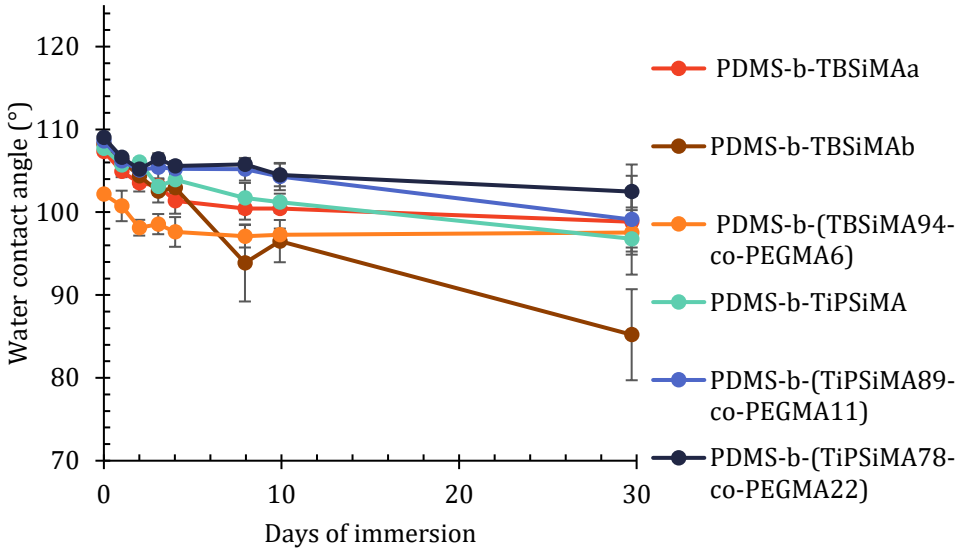

Figure 99: Evolution of water contact angle of the PDMS elastomer-based coatings containing amphiphilic hydrolysable copolymers during prolonged immersion in water.

The decrease in θ_w suggested a dynamic reconstruction of the surface, where the close packing of hydrophobic alkyl moieties was disrupted by the cleavage of silyl ester bonds, and the possible migration to the surface of hydrophilic oxyethylene side chains.

To examine the effect of water on the hydrophobicity/philicity and increasing heterogeneity of the surface, dynamic contact angle measurements were taken with the dynamic sessile drop method. Thus, a water was deposited on the surface. Then, water was first inflated and then sucked up from drop, and the advancing (θ_{adv}) and receding (θ_{rec}) angles were measured during these two steps, respectively. The results were reported in Table 33.

θ_{adv} could be related to the hydrophobic character of the surface, while θ_{rec} is a measure of the hydrophilic character of the surface. Generally, contact angle hysteresis on the polymer surface reflects the rearrangement of the surface structure, topological roughness, chemical heterogeneity, and surface defects. The values of θ_{adv} were relatively high (between 127° and 109°) and close to the values of the static water contact angles. In contrast, θ_{rec} was significantly lower

(with a hysteresis of between 43° and 22°) for films containing the TBSiMA based copolymers, while in case of TiPSiMA based copolymers lower hysteresis ≤ 7° was observed. Thus, the response of the surface to water might be explained by a variation in the chemical composition of the surface coming from the rapid hydrolysis of silyl ester groups within the copolymers and/or a reorganisation of the surface leading to an exposure of oxyethylene side chains, with both phenomena increasing the amount of polar groups available at the surface.

Table 33: Water advancing and receding contact angles and corresponding hystereses of the PDMS based coatings with the sessile drop method.

Film	θ_{adv} **(°)**	θ_{rec} **(°)**	***Hysteresis***[a]
PDMS	109.2±1.2	94.2±0.3	15.0
PDMS-b-TBSiMAa	127.4±3.4	84.1±2.2	43.3
PDMS-b-TBSiMAb	118.6±0.9	96.6±0.2	22.0
PDMS-b-(TBSiMA94-co-PEGMA6)	119.6±2.6	92.3±0.9	27.3
PDMS-b-TiPSiMA	109.2±1.6	103.6±1.7	5.6
PDMS-b-(TiPSiMA89-co-PEGMA11)	109.2±0.6	103.6±1.8	5.6
PDMS-b-(TiPSiMA78-co-PEGMA22)	110.2±1.0	103.1±1.9	7.1

a Calculated as $\theta_{adv} - \theta_{rec}$.

Sessile static and dynamic contact angle may be of less use in systems that are immersed in water for extended periods. Since marine organisms interact with wet surfaces the captive bubble technique is a superior measure of the surface energy as it relates to marine fouling. Captive bubble values are much more akin to receding angles than they are to advancing angles. Hence, to further investigate the response of the surfaces to the aqueous environment, the contact angles of a captive air bubble in water were measured. In this experimental setup (Figure 100) the substrate is facing downward in a square transparent glass vessel filled with deionised water. The air bubble is, then, released from beneath the substrate using a syringe with a J-shaped needle. Captive bubble advancing angle and receding angle could be measured as well subtracting and adding air to the bubble, respectively. All the results from captive air bubble water contact angle measurement were reported in Table 34.

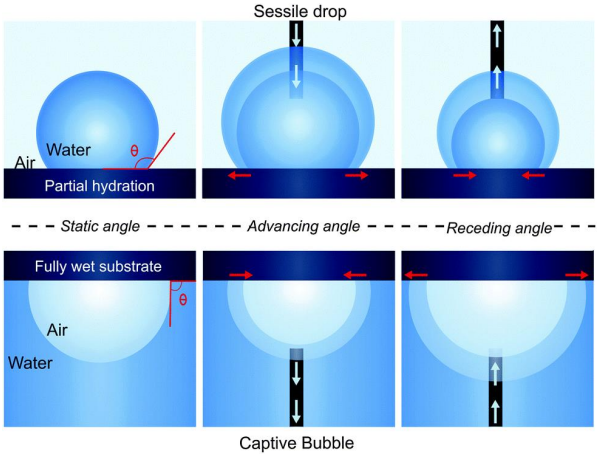

Figure 100: Illustration of three contact angle measurements used to characterise wettability with the sessile drop technique (above) and the captive bubble technique (bottom). Reproduced from ref.[120]

Table 34: Water static contact angle, and water advancing and receding contact angles, with corresponding hystereses, of the PDMS based coatings with the captive air bubble method.

Film	θ_{CBw} (°)	θ_{CBadv} (°)	θ_{CBrec} (°)	***Hys.***[a]
PDMS	104±1	102±2	111±3	9
PDMS-b-TBSiMAa	103.1±0.2	86±3	102.7±0.7	16.4
PDMS-b-TBSiMAb	106.7±0.5	100.8±0.7	104±2	3.4
PDMS-b-(TBSiMA94-co-PEGMA6)	102.4±0.3	92.9±0.6	100±1	7
PDMS-b-TiPSiMA	104.2±0.8	98±1	105±1	7
PDMS-b-(TiPSiMA89-co-PEGMA11)	105.0±0.1	96±3	101±1	5
PDMS-b-(TiPSiMA78-co-PEGMA22)	103.9±0.4	96±1	100.3±0.5	4.3

a Hysteresis calculated as $\theta_{CBrec} - \theta_{CBadv}$.

Captive bubble water contact angle (θ_{CBw}) were significantly lower than sessile drop contact angle (θ_w), and similar to receding contact angles (θ_{rec}) especially for polymers containing TiPSiMA. These previously showed a minor hysteresis in sessile drop dynamic contact angle. This was related to a reorganisation of the

surface that probably occurred in contact with water, as already suggested by sessile drop dynamic contact angle. Moreover, advancing and receding contact angles were measured in the captive bubble setup too, and resulted in a significant reduction of the hysteresis (between 17° and 4°). Thus, captive bubble contact angle measurements represented an improved evaluation of surface hydrophobicity/philicity, starting from a completely wetted surface.

These results suggested that the initial state of the system (exposed to air or water) was critical in determining the wetting (or dewetting) behaviour of the surface of the coatings. This behaviour is expected, as mixed surfaces comprising hydrophilic and hydrophobic moieties have been shown to reconstruct in different environments.[6,121] Moreover, the introduction in copolymers of hydrolytically labile moieties such as silyl esters, added to enhance the responsive character of the surface.

Finally, low surface energy coatings that underwent dynamical reconstruction when in contact with water were obtained, as revealed by sessile drop and captive air bubble contact angle measurements in dynamic conditions and over prolonged immersion of coating in water.

3.1.5 Antifouling and fouling release activity of coatings in static field immersion

Coatings were immersed in natural field in Toulon bay (Figure 101). In suitable racks, two 10 cm x 10 cm PVC panels coated with each tested formulation were immersed the 22nd of June 2017 (Figure 102). This allowed for duplicate inspection and evaluation of the coatings at different time intervals.

PVC panels were sandblasted on the front face, to increase the coating adhesion. The rear face and the edges were protected with a marine self-polishing commercial paint, to keep them clean during the campaign. Two panels coated with a commercial fouling release paint were immersed at the beginning of the campaign, as a benchmark (Hempasil X3 87500 from Hempel[122]). PDMS without any copolymer additive and uncoated PVC were used for comparison.

During regular inspection information was collected on the settled foulants species and the percentage of covered surface. A simple fouling release test was

performed by gently cleaning half panel with a sponge, to evaluate the strength of adhesion. Photographs were taken to record of the evolution of antifouling and fouling release performance of the coatings.

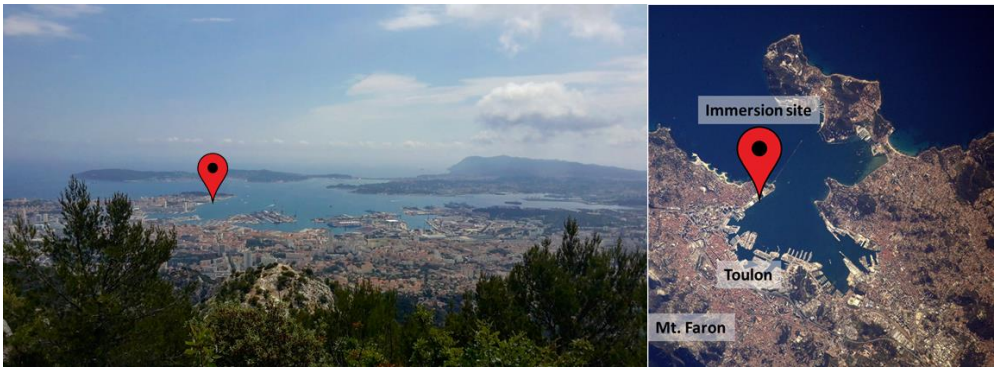

Figure 101: View of Toulon roadster from mount Faron, and satellite map of the immersion site (43°06'25''N; 5°55'41''E).

Figure 102: Rack for panel immersion.

The antifouling properties were estimated[112,123] through an intensity factor I, that is a measure the fouled area, and a severity factor S, which takes into account the frictional drag penalty of ship hulls owing to increased surface roughness due to foulants. Antifouling activity was evaluated with an efficacy parameter N defined as:

$$N = \sum I \; x \; S \qquad \text{Eq. 27}$$

where the sum extended to different identified species of foulants.

A coating was considered effective when:

$$N \leq \frac{N_{uncoated}}{3} \cong 13 \qquad \text{Eq. 28}$$

where $N_{uncoated}$ refers to the efficacy parameter of an uncoated panel immersed simultaneously with the coatings, to observe the biodiversity of marine organisms that have a chance to colonise an untreated surface in the specific coast area, during the immersion campaign (Figure 103). After the fast development of a biofilm in 9 weeks, several macrofoulers grew on the uncoated PVC surface (algae 33%, hydroids 10%, spirorbis 45%, bryozoans 2% and tubeworms 1%). Conversely, on model coatings containing amphiphilic hydrolysable copolymers, the surface was colonised only by spirorbis and hydroids in a limited percentage (2-5% and 1-2%, respectively). The diversity of marine macrofoulers was higher for the PDMS coating without additives, that in addition was colonised by red algae too.

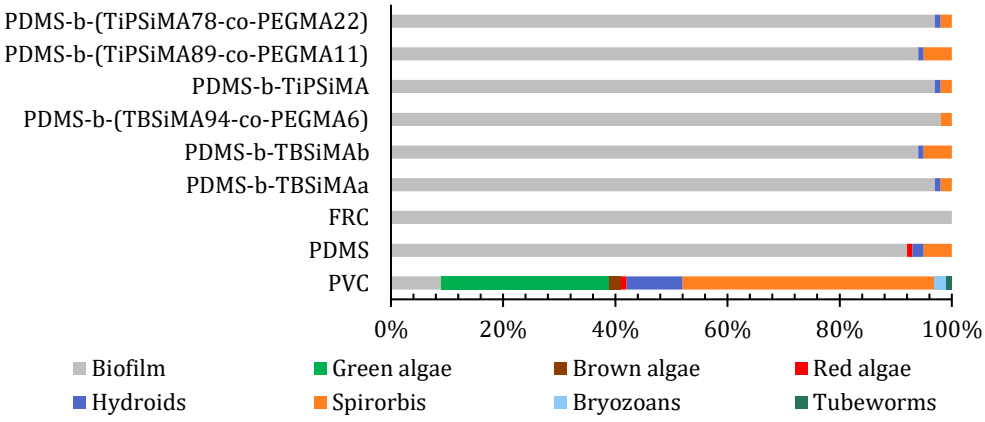

Figure 103: Relative diversity of marine organisms on PDMS based coating surfaces after immersion for 9 weeks in Toulon Bay.

This colonisation accounted for the relatively low efficacy parameter N, calculated for every coating and reported in Figure 104, averaged between the two panels. After 9 weeks, PDMS-*b*-(TBSiMA94-*co*-PEGMA6) and PDMS-*b*-(TiPSiMA89-*co*-PEGMA11) showed the most effective antifouling surface, with a value of N = 13, while the other coatings scored N = 15. Although the copolymer

additives lowered the N parameter with respect to the PDMS matrix (N=17), the values were borderline to be considered effective in absolute terms, and quite inefficient if compared with the commercial fouling-release coating FRC, that displayed an N = 5. After 17 weeks, TiPSiMA78-*co*-PEGMA22 showed the best efficacy parameter (N=9), lower than the commercial FRC (N=11), while the other formulations maintained an N between 13 and 18, near the threshold for good antifouling character.

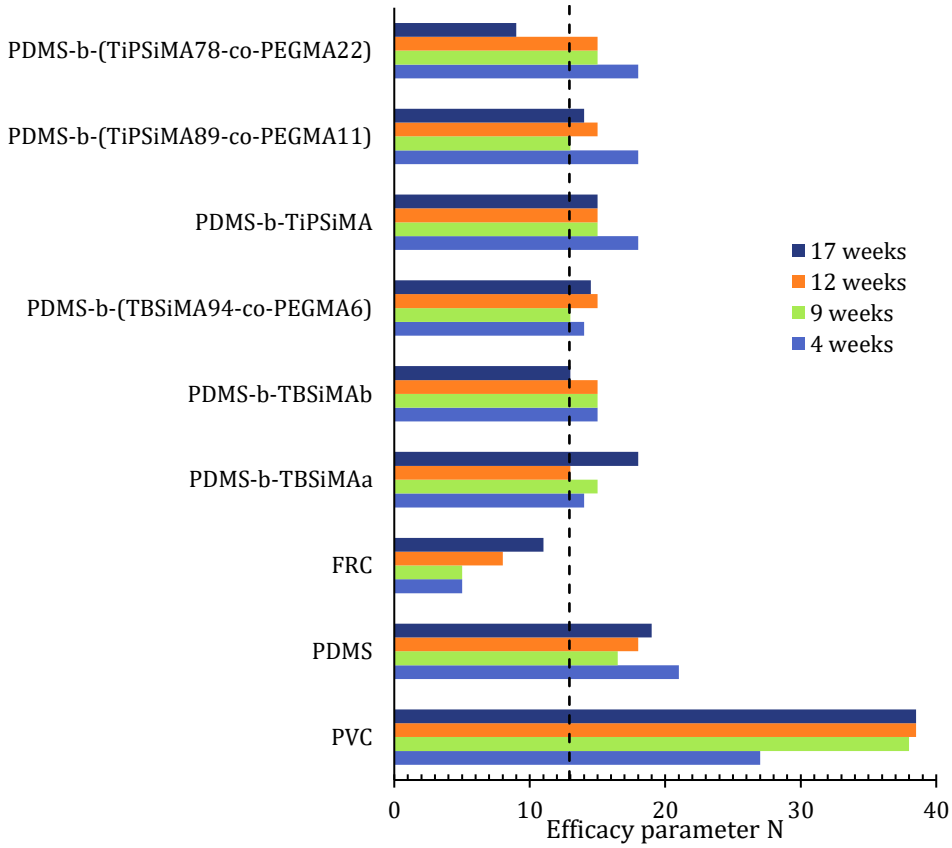

Figure 104: Values of efficacy parameter N of coatings after *in situ* immersion for 4, 9, 12 and 17 weeks inspections. Dashed line highlights N = 13.

Fouling-release property was evaluated by gently cleaning with a wet sponge half panel. Two points were assigned for complete removal of the biomass present on the coating, one point for partial removal and zero point if the biomass remain attached to the surface. The points were averaged for the two panels of every formulation. These results were reported in Table 35.

Table 35: Average scores for fouling-release test on panels during immersion in natural seawater up to 17 weeks.

Film	*4 weeks*	*9 weeks*	*12 weeks*	*17 weeks*
PDMS-b-TBSiMAa	2	2	1.5	2
PDMS-b-TBSiMAb	2	2	2	2
PDMS-b-(TBSiMA94-co-PEGMA6)	2	2	1.5	2
PDMS-b-TiPSiMA	1	2	1	1
PDMS-b-(TiPSiMA89-co-PEGMA11)	2	2	2	2
PDMS-b-(TiPSiMA78-co-PEGMA22)	2	2	2	2
PDMS	2	2	2	2
FRC	2	2	2	2

The removal of the formed biomass from the surface was complete for at least one panel of the two replicates, at every inspection, demonstrating the useful fouling-release character of the formulations containing amphiphilic hydrolysable copolymers. PDMS-*b*-TiPSiMA represented the only exception, suggesting that the slower hydrolysis rate of this copolymer could affect the efficacy of the coating. Nevertheless, the addition of PEGMA in PDMS-b-(TiPSiMA78-*co*-PEGMA22) proved to be beneficial, and considering both the fouling-release results and the N efficacy parameter it proved to be the most promising candidate in the set of model coatings investigated.

3.2 Conclusion

Amphiphilic hydrolysable copolymers were designed to combine two crucial features of amphiphilic fouling-release coatings (i.e. the low elastic modulus of PDMS bulk material and the nanostructured ambiguous surface provided by surface-active polymers) with a hydrolysable motif, inspired by the chemistry of self-polishing, erodible coatings.

RAFT polymerisation was essential for the synthesis of the designed block copolymers. A detailed investigation of the polymerisation kinetics of trialkylsilyl methacrylates TBSiMA and TiPSiMA with PEGMA in RAFT conditions was straightforward owing to *in situ* ^{1}H NMR monitoring of the reactions. Then the target amphiphilic hydrolysable block copolymers were synthesised from a macromolecular PDMS-based chain-transfer agent, used in the polymerisation of TRSiMA either alone or along with PEGMA. Different block lengths and compositions were obtained, while preserving an excellent control on average molecular weight distributions.

Hydrolysis profiles of the synthesised materials were investigated in controlled conditions by ^{1}H NMR. Interestingly, the degradation rate could be finely modulated as a function of the chemistry of the copolymer. TiPSiMA was more stable than TBSiMA toward alkaline hydrolysis. Moreover, the addition of the hydrophilic PEGMA component facilitated the reaction of the cleavable silyl ester bond with water. On the contrary, the presence of the hydrophobic PDMS block slowed down the hydrolysis rate.

All the amphiphilic hydrolysable block copolymers of this work were incorporated into a PDMS matrix to formulate model coatings for the study of wettability and surface free energy, and for the use in bioassay during an immersion campaign in natural seawater to evaluate antifouling and fouling-release properties in the field.

Sessile drop and captive air bubble contact angle measurements in static and dynamic conditions highlighted a noteworthy responsive character of the surface to aqueous environment and suggested a dynamic reconstruction of the surface, where the close packing of hydrophobic alkyl moieties was upset after the cleavage of silyl ester bonds, and the possible migration to the surface of hydrophilic oxyethylene side chains, which were initially hidden beneath the hydrophobic surface of the coating in equilibrium with air.

Immersion of coatings in natural field was carried out in Toulon bay, starting on the 22nd of June 2017. After 17 weeks, during inspection, few colonising organisms were found on the model coating, and some formulations scored an efficacy parameter similar to or lower than a reference commercial fouling-release coating. More inspections are scheduled in the future to continue monitoring of the antifouling and fouling-release properties.

3.3 Experimental

3.3.1 Materials

Dicloromethane (DCM) and toluene (Sigma Aldrich) were distilled over CaH_2 prior to use. 4-Cyano-4-(dodecylsulfanylthiocarbonyl)sulfanylpentanoic acid (CDMP), dicyclohexylcarbodiimide (DCC), 4-dimethylaminopyridine (DMAP) were purchased from Sigma Aldrich and used as received. 2,2'-Azobis(isobutyronitrile) (AIBN, Sigma Aldrich) was recrystallised from methanol. Tributylsilyl methacrylate (TBSiMA, Yuki Gosei Kogyo Co., Ltd. Düsseldorf, Germany), Tri-isopropylsilyl methacrylate (TiPSiMA, Yuki Gosei Kogyo Co., Ltd.) and poly(ethylene glycol) methyl ether methacrylate (PEGMA, Sigma Aldrich, M_n = 300) were dissolved in chloroform and passed through a column of basic alumina to remove inhibitors. α-Hydroxyethylpropoxyl-ω-propyl poly(dimethylsiloxane) (PDMS-OH, M_n = 5100 g/mol, Gelest) was used as received. Deuterated solvents (EURISO-TOP) were used as received. Common laboratory solvents and other reagents (Sigma Aldrich) were used as received.

3.3.2 Characterisation

Nuclear magnetic resonance (NMR)

^{1}H NMR measurements were carried out on a Brüker Advance 400 (400 MHz) spectrometer with deuterated solvents at room temperature.

For *in situ* NMR polymerisation experiments, 0.4 ml of a solution of monomer(s), AIBN and CDMP in deuterated toluene were transferred in a 5 mm heavy wall precision pressure/vacuum valve NMR sample tube (Wilmad 522-PV), equipped with a PTFE needle valve and a pyrex connector. The solution then was degassed through six freeze-pump-thaw cycles, then argon was introduced in the tube to maintain an inert atmosphere during the polymerisation. ^{1}H NMR spectra were acquired at 70°C, every 15.5 minutes. Spectra were processed with mnova software.

The hydrolysis reaction of the trialkylsilyl ester bonds was monitored by ^{1}H - NMR spectrometry. 10 mg of polymer were dissolved in THF-d_8 and 10 µl of

basic buffer (ammonium buffer solution at pH=10) or artificial sea water (ASW at pH = 8.2) were added. At time intervals, ^{1}H -NMR spectra were recorded. In the case of TBSiMA, from integration areas of peaks of protons Si[$\underline{CH_2}$-$(CH_2)_2$-$CH_3]_3$ in the polymer (I_p) and hydrolysis product (I_h), at 0.85 and 0.50 ppm respectively, the percentage of non-hydrolysed silyl ester groups was calculated as:

$$\%\ non-hydrolysed = 100 * \frac{(I_p/6)}{I_p/6+I_h/12} \qquad \text{Eq. 29}$$

Correspondingly, the percentage of the non-hydrolysed silylated side groups of TiPSiMA was calculated as:

$$\%\ non-hydrolysed = 100 * \frac{(I_p/19)-I_{CH_3}}{(I_p/19)-I_{CH_3}+I_h/36} \qquad \text{Eq. 30}$$

where I_p and I_h were the integration areas of ^{1}H NMR peaks of protons –Si[$\underline{CH}$-$(\underline{CH_3})_2]_3$ in polymer and hydrolysed product, respectively at 1.4-1.1 ppm and 1.03 ppm. I_{CH_3} represent a correction for the contribution of methyl protons from the methacrylic main chain that superimposed in the 1.4-1.1 ppm range.

Triple-detection size exclusion chromatography (TD-SEC)

The number-average molecular weight (M_n) and dispersity (M_w/M_n) of polymers were determined by triple detection size exclusion chromatography (TD-SEC). Analyses were performed on a Viscotek apparatus, composed of a GPC Max (comprising a degasser, a pump and an autosampler) with a TDA-302 (RI refractive index detector, right and low angle light scattering detector at 670 nm and viscometer) and an UV detector (λ = 298 nm). THF was used as the eluent with a flow rate of 1.0 mL min^{-1} at 30°C. For each purified polymer, the refractive index increment (dn/dc) was determined using the OmniSec software, from a solution of known concentration filtered through a 0.2 mm PTFE filter.

Contac angle

Static and advancing/receding contact angle (with sessile drop and captive bubble methods) were performed with a Kruss Drop Shape Analyzer DSA30, using water and diiodomethane as testing liquids. Surface energies were calculated with OWR method by the software.

Field tests

In situ seawater immersions were conducted in the Toulon Bay in a semienclosed pond of the military harbor (43°06′25″N, 5°55′41″E), which is the current immersion site for the assessment of antifouling paints for the MAPIEM laboratory. The plates were placed on racks and immersed in water at 1−1.4 m deep. Each coating was immersed in duplicate. A blank sand-blasted PVC plate was also immersed. At every inspection, the plates were rinsed with a water light jet and photographed and a detailed inspection of the plates was achieved. All the samples were immersed on June 22nd, 2017. A French practice adapted from French standard NF T 34-552 was used to assess the AF efficacy of coatings. This standard requires that one reports (i) the type of macrofoulants attached to the surface and (ii) the estimated percentage of the surface covered by each type of macrofoulants (intensity factor, i.e., I). The inspection was performed 1 cm from the edges of the panel. An efficacy parameter N was defined as follows: $N = \sum(I \times S)$, where the sum extended to different identified species of foulants and where S is defined as a severity factor, which takes into account the frictional drag penalty of ship hulls that can be attributed to increased surface roughness due to foulants (see Table 36).

Table 36: Table for the assessment of intensity factor and severity factor, for the calculation of the efficacy parameter N.

Intensity factor I : (% fouled area)		***Severity factor S :***	
No fouling	0	Biofilm	1
Up to 10%	1	Adherents algae	3
10 - 20%	2	Soft foulants	4
20 - 40%	3	Hard foulants	6
40 - 60%	4		
60 - 100%	5		

3.3.3 Synthesis

3.3.3.1 Synthesis of PDMS-CTA

20,00 g of PDMS-OH (3.99 mmol), 0.098 g of DMAP (0.80 mmol), and 70 mL of distilled methylene chloride were added to a 250 mL three-neck round bottom flask equipped with a magnetic stir bar, condenser and two dropping funnels, under a dried argon atmosphere. 2.416 g of CTA (5.99 mmol) in 35 mL distilled methylene chloride and 1.647 g of DCC (7.98 mmol) in 35 mL distilled methylene chloride were separately introduced in the dropping funnels and then added dropwise into the reactor while maintaining the argon flow rate and vigorous stirring. Then, the reaction mixture was placed in an oil bath preheated at 40 °C for 15 h. The flask was then cooled at -20°C and the reaction mixture was filtered to remove any solid impurities. The solvent was removed under reduced pressure. 50 mL of hexane was added and the mixture was cooled and filtered one more time. The resulting solution was diluted with hexane and extracted three times with methanol. The hexane phase was washed first with a saturated NaCl solution and then with deionised water. The solution was dried over magnesium sulfate, filtered, and the hexane was eliminated under reduced pressure. Finally, the product was passed on a silica gel column with a mixture of hexane/ethyl acetate as eluent (10/1 vol/vol). The final pale yellow liquid product was obtained by drying under vacuum. Final yield 80%.

^{1}H-NMR ($CDCl_3$, δ in ppm): 4.25 (2 H, $COOCH_2$), 3.6 (2 H, $COOCH_2\underline{CH_2}$), 3.4 (2 H, $COOCH_2$ $CH_2O\underline{CH_2}$), 3.3 (2 H, SCH_2), 2.7 (2 H, CH_2COO), 2.3-2.6 (2 H, $\underline{CH_2}CH_2COO$), 1.9 (3 H, CH_3CCN), 1.8-1.5 (4 H, $SCH_2\underline{CH_2}$, $\underline{CH_2}CH_2O$), 1.5-1.2 (22 H, CH_2), 0.9 (6 H, CH_3), 0.5 (4 H, $SiCH_2$), 0.5 (396 H, $SiCH_3$).

3.3.3.2 Synthesis of PDMS-*b*-(TBSiMAk-*co*-PEGMAj)

The synthesis of PDMS-*b*-(TBSiMA94-*co*-PEGMA6) will be described. AIBN (0.0063 g, 0.038 mmol), PDMS-CTA (1.0281 g, 0.19 mmol), TBSiMA (3.2225 g, 11.32 mmol) and PEGMA (0.3775 g, 1.25 mmol) in dried toluene (8.4 ml) were charged into a dried flask along with a magnetic stirrer bar. The solution was then deoxygenated by bubbling argon for 30 min at room temperature. The

reaction flask was placed in an oil bath preheated to 70 °C. At the end of the reaction (24 hours), the reaction mixture was cooled to room temperature and the polymer was repeatedly precipitated in methanol from chloroform solutions. The obtained polymer was dried under vacuum to a constant weight.

TD-SEC (THF) M_n = 23800 g/mol M_w/M_n = 1.18

^{1}H-NMR ($CDCl_3$, δ in ppm): 4.0-4.4 (6 H, $COOCH_2$), 3.2-3.9 (48 H, OCH_2), 3.4 (9H, OCH_3) 2.2-1.5 (94 H, $\underline{CH_2}C(CH_3)$),1.35 (528 H, $SiCH_2\underline{CH_2}\underline{CH_2}CH_3$), 1.2 - 0.95 (537 H, $CH_2C(C\underline{H_3})$, $SiCH_2CH_2CH_2\underline{CH_3}$), 0.8 (264 H, $Si\underline{CH_2}CH_2CH_2CH_3$), 0.1 (390 H, $SiCH_3$).

In Table 37 the reaction conditions for the synthesis of the other copolymers of containing TBSiMA were summarised.

Table 37: Reaction conditions for the synthesis of amphiphilic hydrolysable block copolymers PDMS-*b*-TBSiMA.

Copolymer	***AIBN mg (mmol)***	***PDMS-CTA g (mmol)***	***TBSIMA g (mmol)***	**Toluene (ml)**
PDMS-b-TBSiMAa	6.6 (0.04)	1.0785 (0.20)	2.0097 (7.03)	4.7
PDMS-b-TBSiMAb	6.6 (0.04)	1.0795 (0.20)	3.0172 (10.54)	7.0

3.3.3.3 Synthesis of PDMS-*b*-(TiPSiMAk-*co*-PEGMAj)

The synthesis of PDMS-*b*-(TiPSiMA89-*co*-PEGMA11) will be described. AIBN (8.0 mg, 0.048 mmol), PDMS-CTA (1.306 g, 0.24 mmol), TBSiMA (3.7820 g, 15.60 mmol) and PEGMA (0.7180 g, 2.39 mmol) in dried toluene (12 ml) were charged into a dried flask along with a magnetic stirrer bar. The solution was then deoxygenated by bubbling argon for 30 min at room temperature. The reaction flask was placed in an oil bath preheated to 70 °C. At the end of the reaction (48 hours), the reaction mixture was cooled to room temperature and the polymer was repeatedly precipitated in methanol from chloroform solutions. The obtained polymer was dried under vacuum to a constant weight.

TD-SEC (THF) M_n = 24500 g/mol M_w/M_n = 1.20

^{1}H-NMR ($CDCl_3$, δ in ppm): 4.0-4.4 (14 H, $COOCH_2$), 3.2-3.9 (112 H, OCH_2), 3.4 (21 H, OCH_3) 2.3-1.5 (126 H, $\underline{CH_2}C(CH_3)$), 1.5-0.9 (1365 H, $CH_2C(C\underline{H_3})$, $SiCH(\underline{CH_3})_2$, $Si\underline{CH}(CH_3)_2$) 0.1 (390 H, $SiCH_3$).

In Table 38 the reaction conditions for the synthesis of the other copolymers of containing TiPSiMA were summarised.

Table 38: Reaction conditions for the synthesis of amphiphilic hydrolysable block copolymers PDMS-*b*-(TiPSiMAk-*co*-PEGMAj).

Copolymer	***AIBN mg (mmol)***	***PDMS-CTA g (mmol)***	***PEGMA g (mmol)***	***TiPSIMA g (mmol)***	***Toluene (ml)***
PDMS-b-TiPSiMA	6.6 (0.04)	1.0795 (0.20)	--	2.0045 (8.25)	5.5
PDMS-b-(TiPSiMA78-co-PEGMA22)	7.8 (0.05)	1.2887 (0.24)	1.4326 (4.77)	3.0674 (12.65)	11.6

4 REFERENCES

(1) Raffa, P.; Wever, D. A. Z.; Picchioni, F.; Broekhuis, A. A. Polymeric Surfactants: Synthesis, Properties, and Links to Applications. *Chem. Rev.* **2015**, *115* (16), 8504–8563 DOI: 10.1021/cr500129h.

(2) BASF. Pluronic http://product-finder.basf.com/group/corporate/product-finder/en/brand/PLURONIC (accessed Sep 30, 2017).

(3) Pitto-Barry, A.; Barry, N. P. E. Pluronic® Block-Copolymers in Medicine: From Chemical and Biological Versatility to Rationalisation and Clinical Advances. *Polym. Chem.* **2014**, *5* (10), 3291–3297 DOI: 10.1039/C4PY00039K.

(4) Batrakova, E. V; Kabanov, A. V. Pluronic Block Copolymers: Evolution of Drug Delivery Concept from Inert Nanocarriers to Biological Response Modifiers. *J. Control. Release* **2008**, *130* (2), 98–106 DOI: 10.1016/j.jconrel.2008.04.013.

(5) Hadjichristidis, N.; Pitsikalis, M.; Pispas, S.; Iatrou, H. Polymers with Complex Architecture by Living Anionic Polymerization. *Chem. Rev.* **2001**, *101* (12), 3747–3792 DOI: 10.1021/cr9901337.

(6) Galli, G.; Martinelli, E. Amphiphilic Polymer Platforms: Surface Engineering of Films for Marine Antibiofouling. *Macromol. Rapid Commun.* **2017**, *38* (8), 1600704 DOI: 10.1002/marc.201600704.

(7) Wever, D. A. Z.; Picchioni, F.; Broekhuis, A. A. Polymers for Enhanced Oil Recovery: A Paradigm for Structure–property Relationship in Aqueous Solution. *Prog. Polym. Sci.* **2011**, *36* (11), 1558–1628 DOI: 10.1016/j.progpolymsci.2011.05.006.

(8) Riess, G. Micellization of Block Copolymers. *Prog. Polym. Sci.* **2003**, *28* (7), 1107–1170 DOI: 10.1016/S0079-6700(03)00015-7.

(9) Mok, M. M.; Thiagarajan, R.; Flores, M.; Morse, D. C.; Lodge, T. P. Apparent Critical Micelle Concentrations in Block Copolymer/ionic Liquid Solutions: Remarkably Weak Dependence on Solvophobic Block Molecular Weight. *Macromolecules* **2012**, *45* (11), 4818–4829 DOI: 10.1021/ma300399c.

(10) Kim, J.-W.; Ko, J.-Y.; Park, J.-G.; Jun, J.-B.; Chang, I.-S.; Suh, K.-D. Fine Polystyrene Latexes with Reactive Poly(ethylene Oxide) -Poly(propylene Oxide)-Poly(ethylene Oxide) Triblock Macrosurfactants in Modified Miniemulsion Polymerization. *J. Appl. Polym. Sci.* **2002**, *85* (2), 328–332 DOI: 10.1002/app.10636.

(11) Moughton, A. O.; Hillmyer, M. a.; Lodge, T. P. Multicompartment Block Polymer Micelles. *Macromolecules* **2012**, *45* (1), 2–19 DOI: 10.1021/ma201865s.

(12) Gohy, J. Block Copolymer Micelles. In *Block Copolymers II*; Springer-Verlag: Berlin/Heidelberg, 2005; pp 65–136.

(13) Gröschel, A. H.; Schacher, F. H.; Schmalz, H.; Borisov, O. V; Zhulina, E. B.; Walther, A.; Müller, A. H. E. Precise Hierarchical Self-Assembly of Multicompartment Micelles. *Nat. Commun.* **2012**, *3*, 710 DOI: 10.1038/ncomms1707.

(14) Li, L.; Raghupathi, K.; Song, C.; Prasad, P.; Thayumanavan, S. Self-Assembly of Random Copolymers. *Chem. Commun.* **2014**, *50* (88), 13417–13432 DOI: 10.1039/C4CC03688C.

(15) Zhu, X.; Liu, M. Self-Assembly and Morphology Control of New L -Glutamic Acid-Based Amphiphilic Random Copolymers: Giant Vesicles, Vesicles, Spheres, and Honeycomb Film. *Langmuir* **2011**, *27* (21), 12844–12850 DOI: 10.1021/la202680j.

(16) Mecerreyes, D.; Lee, V.; Hawker, C. J.; Hedrick, J. L.; Wursch, A.; Volksen, W.; Magbitang, T.; Huang, E.; Miller, R. D. A Novel Approach to Functionalized Nanoparticles: Self-Crosslinking of Macromolecules in Ultradilute Solution. *Adv. Mater.* **2001**, *13* (3), 204–208 DOI: 10.1002/1521-4095(200102)13:3<204::AID-ADMA204>3.0.CO;2-9.

(17) Altintas, O.; Barner-Kowollik, C. Single Chain Folding of Synthetic Polymers by Covalent and Non-Covalent Interactions: Current Status and Future Perspectives. *Macromol. Rapid Commun.* **2012**, *33* (11), 958–971 DOI: 10.1002/marc.201200049.

(18) Altintas, O.; Barner-Kowollik, C. Single-Chain Folding of Synthetic Polymers: A Critical Update. *Macromol. Rapid Commun.* **2016**, *37* (1), 29–46 DOI: 10.1002/marc.201500547.

(19) Ouchi, M.; Badi, N.; Lutz, J.-F.; Sawamoto, M. Single-Chain Technology Using Discrete Synthetic Macromolecules. *Nat. Chem.* **2011**, *3* (12), 917–924 DOI: 10.1038/nchem.1175.

(20) Berda, E. B.; Foster, E. J.; Meijer, E. W. Toward Controlling Folding in Synthetic Polymers: Fabricating and Characterizing Supramolecular Single-Chain Nanoparticles. *Macromolecules* **2010**, *43* (3), 1430–1437

DOI: 10.1021/ma902393h.

(21) Gonzalez-Burgos, M.; Latorre-Sanchez, A.; Pomposo, J. A. Advances in Single Chain Technology. *Chem. Soc. Rev.* **2015**, *44* (17), 6122–6142 DOI: 10.1039/C5CS00209E.

(22) Sanchez-Sanchez, A.; Pérez-Baena, I.; Pomposo, J. a. Advances in Click Chemistry for Single-Chain Nanoparticle Construction. *Molecules* **2013**, *18* (3), 3339–3355 DOI: 10.3390/molecules18033339.

(23) Lyon, C. K.; Prasher, A.; Hanlon, A. M.; Tuten, B. T.; Tooley, C. a.; Frank, P. G.; Berda, E. B. A Brief User's Guide to Single-Chain Nanoparticles. *Polym. Chem.* **2015**, *6* (2), 181–197 DOI: 10.1039/C4PY01217H.

(24) Huo, M.; Wang, N.; Fang, T.; Sun, M.; Wei, Y.; Yuan, J. Single-Chain Polymer Nanoparticles: Mimic the Proteins. *Polym. (United Kingdom)* **2015**, *66*, A11–A21 DOI: 10.1016/j.polymer.2015.04.011.

(25) Seo, M.; Beck, B. J.; Paulusse, J. M. J.; Hawker, C. J.; Kim, S. Y. Polymeric Nanoparticles via Noncovalent Cross-Linking of Linear Chains. *Macromolecules* **2008**, *41* (17), 6413–6418 DOI: 10.1021/ma8009678.

(26) Foster, E. J.; Berda, E. B.; Meijer, E. W. Metastable Supramolecular Polymer Nanoparticles via Intramolecular Collapse of Single Polymer Chains. *J. Am. Chem. Soc.* **2009**, *131* (20), 6964–6966 DOI: 10.1021/ja901687d.

(27) Terashima, T.; Mes, T.; De Greef, T. F. a; Gillissen, M. a J.; Besenius, P.; Palmans, A. R. a; Meijer, E. W. Single-Chain Folding of Polymers for Catalytic Systems in Water. *J. Am. Chem. Soc.* **2011**, *133* (13), 4742–4745 DOI: 10.1021/ja2004494.

(28) Appel, E. A.; Dyson, J.; Delbarrio, J.; Walsh, Z.; Scherman, O. A. Formation of Single-Chain Polymer Nanoparticles in Water through Host-Guest Interactions. *Angew. Chemie - Int. Ed.* **2012**, *51* (17), 4185–4189 DOI: 10.1002/anie.201108659.

(29) Akagi, T.; Piyapakorn, P.; Akashi, M. Formation of Unimer Nanoparticles by Controlling the Self-Association of Hydrophobically Modified Poly(amino Acid)s. *Langmuir* **2012**, *28* (11), 5249–5256 DOI: 10.1021/la205093j.

(30) Basasoro, S.; Gonzalez-Burgos, M.; Moreno, A. J.; Verso, F. Lo; Arbe, A.; Colmenero, J.; Pomposo, J. A. A Solvent-Based Strategy for Tuning the Internal Structure of Metallo-Folded Single-Chain Nanoparticles. *Macromol. Rapid Commun.* **2016**, *37* (13), 1060–1065 DOI: 10.1002/marc.201600139.

(31) Chen, M.; Riddles, C. J.; Van De Mark, M. R. Electroviscous Contribution to the Rheology of Colloidal Unimolecular Polymer (CUP) Particles in Water.

Langmuir **2013**, *29* (46), 14034–14043 DOI: 10.1021/la4026552.

(32) Terashima, T.; Sugita, T.; Fukae, K.; Sawamoto, M. Synthesis and Single-Chain Folding of Amphiphilic Random Copolymers in Water. *Macromolecules* **2014**, *47* (2), 589–600 DOI: 10.1021/ma402355v.

(33) Koda, Y.; Terashima, T.; Sawamoto, M.; Maynard, H. D. Amphiphilic/fluorous Random Copolymers as a New Class of Non-Cytotoxic Polymeric Materials for Protein Conjugation. *Polym. Chem.* **2015**, *6* (2), 240–247 DOI: 10.1039/C4PY01346H.

(34) Ashraf, S.; Pelaz, B.; Pino, P.; Escudero, A.; Parak, W. J.; Soliman, M. G.; Zhang, Q.; Carrillo-carrion, C. *Light-Responsive Nanostructured Systems for Applications in Nanomedicine*; Sortino, S., Ed.; Topics in Current Chemistry; Springer International Publishing: Cham, 2016; Vol. 370.

(35) Tirotta, I.; Dichiarante, V.; Pigliacelli, C.; Cavallo, G.; Terraneo, G.; Bombelli, F. B.; Metrangolo, P.; Resnati, G. 19 F Magnetic Resonance Imaging (MRI): From Design of Materials to Clinical Applications. *Chem. Rev.* **2015**, *115* (2), 1106–1129 DOI: 10.1021/cr500286d.

(36) Artar, M.; Terashima, T.; Sawamoto, M.; Meijer, E. W.; Palmans, A. R. a. Understanding the Catalytic Activity of Single-Chain Polymeric Nanoparticles in Water. *J. Polym. Sci. Part A Polym. Chem.* **2014**, *52* (1), 12–20 DOI: 10.1002/pola.26970.

(37) Haidekker, M. A.; Nipper, M.; Mustafic, A.; Lichlyter, D.; Dakanali, M.; Theodorakis, E. A. Dyes with Segmental Mobility: Molecular Rotors. In *Advanced Fluorescence Reporters in Chemistry and Biology I*; Demchenko, A. P., Ed.; Springer Series on Fluorescence; Springer Berlin Heidelberg: Berlin, Heidelberg, 2010; Vol. 8, pp 267–308.

(38) Mei, J.; Hong, Y.; Lam, J. W. Y.; Qin, A.; Tang, Y.; Tang, B. Z. Aggregation-Induced Emission: The Whole Is More Brilliant than the Parts. *Adv. Mater.* **2014**, *26* (31), 5429–5479 DOI: 10.1002/adma.201401356.

(39) Haidekker, M. a; Theodorakis, E. a. Environment-Sensitive Behavior of Fluorescent Molecular Rotors. *J. Biol. Eng.* **2010**, *4*, 11 DOI: 10.1186/1754-1611-4-11.

(40) Ponjavic, A.; Dench, J.; Morgan, N.; Wong, J. S. S. *In Situ* Viscosity Measurement of Confined Liquids. *RSC Adv.* **2015**, *5* (121), 99585–99593 DOI: 10.1039/C5RA19245E.

(41) Goh, W. L.; Lee, M. Y.; Joseph, T. L.; Quah, S. T.; Brown, C. J.; Verma, C.; Brenner, S.; Ghadessy, F. J.; Teo, Y. N. Molecular Rotors As Conditionally Fluorescent Labels for Rapid Detection of Biomolecular Interactions. *J. Am. Chem. Soc.* **2014**, *136* (17), 6159–6162 DOI: 10.1021/ja413031h.

(42) Vyšniauskas, A.; Qurashi, M.; Kuimova, M. K. A Molecular Rotor That

Measures Dynamic Changes of Lipid Bilayer Viscosity Caused by Oxidative Stress. *Chem. - A Eur. J.* **2016**, *22* (37), 13210–13217 DOI: 10.1002/chem.201601925.

(43) Vaccaro, G.; Bianchi, A.; Mauri, M.; Bonetti, S.; Meinardi, F.; Sanguineti, A.; Simonutti, R.; Beverina, L. Direct Monitoring of Self-Assembly of Copolymeric Micelles by a Luminescent Molecular Rotor. *Chem. Commun.* **2013**, *49* (76), 8474 DOI: 10.1039/c3cc44590a.

(44) Thompson, A. J.; Herling, T. W.; Kubánková, M.; Vyšniauskas, A.; Knowles, T. P. J.; Kuimova, M. K. Molecular Rotors Provide Insights into Microscopic Structural Changes During Protein Aggregation. *J. Phys. Chem. B* **2015**, *119* (32), 10170–10179 DOI: 10.1021/acs.jpcb.5b05099.

(45) Kubánková, M.; López-Duarte, I.; Bull, J. A.; Vadukul, D. M.; Serpell, L. C.; de Saint Victor, M.; Stride, E.; Kuimova, M. K. Probing Supramolecular Protein Assembly Using Covalently Attached Fluorescent Molecular Rotors. *Biomaterials* **2017**, *139*, 195–201 DOI: 10.1016/j.biomaterials.2017.06.009.

(46) Frochot, C.; Mascherin, M.; Haumont, A.; Viriot, M.-L.; Marie, E. Fluorescence Spectroscopy as a Non Invasive Tool to Follow in Situ the Polymerization in Miniemulsion. *J. Appl. Polym. Sci.* **2011**, *119* (1), 219–224 DOI: 10.1002/app.32511.

(47) Martini, G.; Martinelli, E.; Ruggeri, G.; Galli, G.; Pucci, A. Julolidine Fluorescent Molecular Rotors as Vapour Sensing Probes in Polystyrene Films. *Dye. Pigment.* **2015**, *113*, 47–54 DOI: 10.1016/j.dyepig.2014.07.025.

(48) Iasilli, G.; Martini, F.; Minei, P.; Ruggeri, G.; Pucci, A. Vapochromic Features of New Luminogens Based on Julolidine-Containing Styrene Copolymers. *Faraday Discuss.* **2017**, *196*, 113–129 DOI: 10.1039/C6FD00151C.

(49) Borelli, M.; Iasilli, G.; Minei, P.; Pucci, A. Fluorescent Polystyrene Films for the Detection of Volatile Organic Compounds Using the Twisted Intramolecular Charge Transfer Mechanism. *Molecules* **2017**, *22* (8), 1306 DOI: 10.3390/molecules22081306.

(50) Woods Hole Oceanographic Institution. Barnacle and Biofilm https://www.whoi.edu/page.do?pid=10095&tid=7342&cid=155889 (accessed Oct 2, 2017).

(51) Nurioglu, A. G.; Esteves, A. C. C.; de With, G. Non-Toxic, Non-Biocide-Release Antifouling Coatings Based on Molecular Structure Design for Marine Applications. *J. Mater. Chem. B* **2015**, *3* (32), 6547–6570 DOI: 10.1039/C5TB00232J.

(52) George, P. A.; Donose, B. C.; Cooper-white, J. J. Biomaterials Surface

Coatings : Resistance to Protein and Cell Adhesion. *Biomaterials* **2009**, *30* (13), 2449–2456 DOI: 10.1016/j.biomaterials.2009.01.012.

(53) Magin, C. M.; Cooper, S. P.; Brennan, A. B. Non-Toxic Antifouling Strategies. *Mater. Today* **2010**, *13* (4), 36–44 DOI: 10.1016/S1369-7021(10)70058-4.

(54) Ytreberg, E.; Karlsson, J.; Eklund, B. Comparison of Toxicity and Release Rates of Cu and Zn from Anti-Fouling Paints Leached in Natural and Artificial Brackish Seawater. *Sci. Total Environ.* **2010**, *408* (12), 2459–2466 DOI: 10.1016/j.scitotenv.2010.02.036.

(55) Callow, J. a; Callow, M. E. Trends in the Development of Environmentally Friendly Fouling-Resistant Marine Coatings. *Nat. Commun.* **2011**, *2*, 244 DOI: 10.1038/ncomms1251.

(56) Callow, J. a; Callow, M. E. Trends in the Development of Environmentally Friendly Fouling-Resistant Marine Coatings. *Nat. Commun.* **2011**, *2*, 244 DOI: 10.1038/ncomms1251.

(57) Mccollin, T.; Brown, L. Native and Non Native Marine Biofouling Species Present on Commercial Vessels Using Scottish Dry Docks and Harbours. *Manag. Biol. Invasions* **2014**, *5* (2), 85–96 DOI: 10.3391/mbi.2014.5.2.02.

(58) Ciriminna, R.; Bright, F. V.; Pagliaro, M. Ecofriendly Antifouling Marine Coatings. *ACS Sustain. Chem. Eng.* **2015**, *3* (4), 559–565 DOI: 10.1021/sc500845n.

(59) Lejars, M.; Margaillan, A.; Bressy, C. Fouling Release Coatings: A Nontoxic Alternative to Biocidal Antifouling Coatings. *Chem. Rev.* **2012**, *112* (8), 4347–4390 DOI: 10.1021/cr200350v.

(60) Baier, R. E. Surface Behaviour of Biomaterials: The Theta Surface for Biocompatibility. *J. Mater. Sci. Mater. Med.* **2006**, *17* (11), 1057–1062 DOI: 10.1007/s10856-006-0444-8.

(61) Brady, R. F.; Singer, I. L. Mechanical Factors Favoring Release from Fouling Release Coatings. *Biofouling* **2000**, *15* (1–3), 73–81 DOI: 10.1080/08927010009386299.

(62) Banerjee, I.; Pangule, R. C.; Kane, R. S. Antifouling Coatings: Recent Developments in the Design of Surfaces That Prevent Fouling by Proteins, Bacteria, and Marine Organisms. *Adv. Mater.* **2011**, *23* (6), 690–718 DOI: 10.1002/adma.201001215.

(63) Hayashi, T.; Hara, M. Nonfouling Self-Assembled Monolayers: Mechanisms Underlying Protein and Cell Resistance. *Curr. Phys. Chem.* **2011**, *1* (2), 90–98 DOI: 10.2174/1877946811101020090.

(64) Nesvadba, P. Radical Polymerization in Industry. In *Encyclopedia of Radicals in Chemistry, Biology and Materials*; 2012; pp 1–36.

(65) Jenkins, A. D.; Jones, R. G.; Moad, G. Terminology for Reversible-Deactivation Radical Polymerization Previously Called "controlled" radical Or "living" radical Polymerization. *Pure Appl. Chem.* **2009**, *82* (2), 483–491 DOI: 10.1351/PAC-REP-08-04-03.

(66) Gregory, A.; Stenzel, M. H. Complex Polymer Architectures via RAFT Polymerization: From Fundamental Process to Extending the Scope Using Click Chemistry and Nature's Building Blocks. *Prog. Polym. Sci.* **2012**, *37* (1), 38–105 DOI: 10.1016/j.progpolymsci.2011.08.004.

(67) Matyjaszewski, K.; Tsarevsky, N. V. Macromolecular Engineering by Atom Transfer Radical Polymerization. *J. Am. Chem. Soc.* **2014**, *136* (18), 6513–6533 DOI: 10.1021/ja408069v.

(68) Destarac, M. Controlled Radical Polymerization: Industrial Stakes, Obstacles and Achievements. *Macromol. React. Eng.* **2010**, *4* (3–4), 165–179 DOI: 10.1002/mren.200900087.

(69) Chiefari, J.; Chong, Y. K. B.; Ercole, F.; Krstina, J.; Jeffery, J.; Le, T. P. T.; Mayadunne, R. T. A.; Meijs, G. F.; Moad, C. L.; Moad, G.; Rizzardo, E.; Thang, S. H. Living Free-Radical Polymerization by Reversible Addition−Fragmentation Chain Transfer: The RAFT Process. *Macromolecules* **1998**, *31* (16), 5559–5562 DOI: 10.1021/ma9804951.

(70) Moad, G.; Rizzardo, E.; Thang, S. H. A RAFT Tutorial. *Strem Chem.* **2011**, *25* (1), 2–10.

(71) Ouchi, M.; Terashima, T.; Sawamoto, M. Transition Metal-Catalyzed Living Radical Polymerization: Toward Perfection in Catalysis and Precision Polymer Synthesis. *Chem. Rev.* **2009**, *109* (11), 4963–5050 DOI: 10.1021/cr900234b.

(72) Matyjaszewski, K. A.; Xia, J. Atom Transfer Radical Polymerization. *Chem. Rev.* **2001**, *101* (9), 2921–2990 DOI: 10.1021/cr940534g.

(73) Matyjaszewski, K. Atom Transfer Radical Polymerization (ATRP): Current Status and Future Perspectives. *Macromolecules* **2012**, *45* (10), 4015–4039 DOI: 10.1021/ma3001719.

(74) Matyjaszewski, K.; Xia, J. Atom Transfer Radical Polymerization. *Chem. Rev.* **2001**, *101* (9), 2921–2990 DOI: 10.1021/cr940534g.

(75) Matyjaszewski, K.; Coca, S.; Gaynor, S. G.; Wei, M.; Woodworth, B. E. Zerovalent Metals in Controlled/"Living" Radical Polymerization. *Macromolecules* **1997**, *30* (23), 7348–7350 DOI: 10.1021/ma971258l.

(76) Percec, V.; Guliashvili, T.; Ladislaw, J. S.; Wistrand, A.; Stjerndahl, A.; Sienkowska, M. J.; Monteiro, M. J.; Sahoo, S. Ultrafast Synthesis of Ultrahigh Molar Mass Polymers by Metal-Catalyzed Living Radical Polymerization of Acrylates, Methacrylates, and Vinyl Chloride Mediated

by SET at 25 °C. *J. Am. Chem. Soc.* **2006**, *128* (43), 14156–14165 DOI: 10.1021/ja065484z.

(77) Zhang, Q.; Wilson, P.; Li, Z.; McHale, R.; Godfrey, J.; Anastasaki, A.; Waldron, C.; Haddleton, D. M. Aqueous Copper-Mediated Living Polymerization: Exploiting Rapid Disproportionation of CuBr with Me 6 TREN. *J. Am. Chem. Soc.* **2013**, *135* (19), 7355–7363 DOI: 10.1021/ja4026402.

(78) Anastasaki, A.; Nikolaou, V.; Nurumbetov, G.; Wilson, P.; Kempe, K.; Quinn, J. F.; Davis, T. P.; Whittaker, M. R.; Haddleton, D. M. Cu(0)-Mediated Living Radical Polymerization: A Versatile Tool for Materials Synthesis. *Chem. Rev.* **2016**, *116* (3), 835–877 DOI: 10.1021/acs.chemrev.5b00191.

(79) Canning, S. L.; Smith, G. N.; Armes, S. P. A Critical Appraisal of RAFT-Mediated Polymerization-Induced Self-Assembly. *Macromolecules* **2016**, *49* (6), 1985–2001 DOI: 10.1021/acs.macromol.5b02602.

(80) Charleux, B.; Delaittre, G.; Rieger, J.; D'Agosto, F. Polymerization-Induced Self-Assembly: From Soluble Macromolecules to Block Copolymer Nano-Objects in One Step. *Macromolecules* **2012**, *45* (17), 6753–6765 DOI: 10.1021/ma300713f.

(81) Sugihara, S.; Armes, S. P.; Lewis, A. L. One-Pot Synthesis of Biomimetic Shell Cross-Linked Micelles and Nanocages by ATRP in Alcohol/Water Mixtures. *Angew. Chemie Int. Ed.* **2010**, *49* (20), 3500–3503 DOI: 10.1002/anie.201000095.

(82) Wang, G.; Schmitt, M.; Wang, Z.; Lee, B.; Pan, X.; Fu, L.; Yan, J.; Li, S.; Xie, G.; Bockstaller, M. R.; Matyjaszewski, K. Polymerization-Induced Self-Assembly (PISA) Using ICAR ATRP at Low Catalyst Concentration. *Macromolecules* **2016**, *49* (22), 8605–8615 DOI: 10.1021/acs.macromol.6b01966.

(83) Kapishon, V.; Whitney, R. A.; Champagne, P.; Cunningham, M. F.; Neufeld, R. J. Polymerization Induced Self-Assembly of Alginate Based Amphiphilic Graft Copolymers Synthesized by Single Electron Transfer Living Radical Polymerization. *Biomacromolecules* **2015**, *16* (7), 2040–2048 DOI: 10.1021/acs.biomac.5b00470.

(84) Brusseau, S.; D'Agosto, F.; Magnet, S.; Couvreur, L.; Chamignon, C.; Charleux, B. Nitroxide-Mediated Copolymerization of Methacrylic Acid and Sodium 4-Styrenesulfonate in Water Solution and One-Pot Synthesis of Amphiphilic Block Copolymer Nanoparticles. *Macromolecules* **2011**, *44* (14), 5590–5598 DOI: 10.1021/ma2008282.

(85) Groison, E.; Brusseau, S.; D'Agosto, F.; Magnet, S.; Inoubli, R.; Couvreur, L.; Charleux, B. Well-Defined Amphiphilic Block Copolymer Nanoobjects via Nitroxide-Mediated Emulsion Polymerization. *ACS Macro Lett.* **2012**, *1*

(1), 47–51 DOI: 10.1021/mz200035b.

(86) Derry, M. J.; Fielding, L. A.; Armes, S. P. Polymerization-Induced Self-Assembly of Block Copolymer Nanoparticles via RAFT Non-Aqueous Dispersion Polymerization. *Prog. Polym. Sci.* **2016**, *52*, 1–18 DOI: 10.1016/j.progpolymsci.2015.10.002.

(87) Nguyen, N. H.; Leng, X.; Sun, H. J.; Percec, V. Single-Electron Transfer-Living Radical Polymerization of Oligo(ethylene Oxide) Methyl Ether Methacrylate in the Absence and Presence of Air. *J. Polym. Sci. Part A Polym. Chem.* **2013**, *51* (15), 3110–3122 DOI: 10.1002/pola.26718.

(88) Nguyen, N. H.; Kulis, J.; Sun, H.; Jia, Z.; Beusekom, B. Van; Levere, M. E.; Wilson, D. A.; Monteiro, J.; Percec, V. A Comparative Study of the SET-LRP of Oligo (Ethylene Oxide) Methyl Ether Acrylate in DMSO and in H 2 O. *Polym. Chem.* **2013**, *2* (0), 144–155 DOI: 10.1039/c2py20782f.

(89) Bouilhac, C.; Cloutet, E.; Cramail, H.; Deffieux, A.; Taton, D. Functionalized Star-Like Polystyrenes as Organic Supports of a Tridentate Bis(imino)pyridinyliron/Aluminic Derivative Catalytic System for Ethylene Polymerization. *Macromol. Rapid Commun.* **2005**, *26* (20), 1619–1625 DOI: 10.1002/marc.200500430.

(90) Samanta, S. R.; Cai, R.; Percec, V. SET-LRP of Semifluorinated Acrylates and Methacrylates. *Polym. Chem.* **2014**, 5479–5491 DOI: 10.1039/c4py00635f.

(91) Dadayli, D.; Harris, R. K.; Kenwright, A. M.; Say, B. J.; Sünnetçioğlu, M. M. Solid-State 1H N.m.r. Studies of Polypropylene. *Polymer (Guildf).* **1994**, *35* (19), 4083–4087 DOI: 10.1016/0032-3861(94)90579-7.

(92) Borsacchi, S.; Cappellozza, S.; Catalano, D.; Geppi, M.; Ierardi, V. Solid State NMR Investigation of the Molecular Dynamics of Cocoon Silks Produced by Different Bombyx M Ori (Lepidoptera) Strains. *Biomacromolecules* **2006**, *7* (4), 1266–1273 DOI: 10.1021/bm0510092.

(93) Meiboom, S.; Gill, D. Modified Spin-Echo Method for Measuring Nuclear Relaxation Times. *Rev. Sci. Instrum.* **1958**, *29* (8), 688–691 DOI: 10.1063/1.1716296.

(94) Trzebicka, B.; Szweda, D.; Rangelov, S.; Kowalczuk, A.; Mendrek, B.; Utrata-Wesołek, A.; Dworak, A. (Co)polymers of Oligo(ethylene Glycol) Methacrylates-Temperature-Induced Aggregation in Aqueous Solution. *J. Polym. Sci. Part A Polym. Chem.* **2013**, *51* (3), 614–623 DOI: 10.1002/pola.26410.

(95) Szweda, D.; Szweda, R.; Dworak, A.; Trzebicka, B. Thermoresponsive Poly[oligo(ethylene Glycol) Methacrylate]s and Their Bioconjugates – Synthesis and Solution Behavior. *Polimery* **2017**, *62* (4), 298–310 DOI:

10.14314/polimery.2017.298.

(96) Connolly, M. L. Solvent-Accessible Surfaces of Proteins and Nucleic Acids. *Science* **1983**, *221* (4612), 709–713.

(97) Varshney, A.; Brooks, F. P.; Wright, W. V. Computing Smooth Molecular Surfaces. *IEEE Comput. Graph. Appl.* **1994**, *14* (5), 19–25 DOI: 10.1109/38.310720.

(98) Kwok, D. Y.; Neumann, A. W. Contact Angle Measurement and Contact Angle Interpretation. *Adv. Colloid Interface Sci.* **1999**, *81* (3), 167–249 DOI: 10.1016/S0001-8686(98)00087-6.

(99) Li, D.; Neumann, A. W.; Press, A. A Reformulation of the Equation of State for Interfacial Tensions. *J. Colloid Interface Sci.* **1990**, *137* (1), 1–4.

(100) Wang, J.; Wolf, R. M.; Caldwell, J. W.; Kollman, P. A.; Case, D. A. Development and Testing of a General Amber Force Field. *J. Comput. Chem.* **2004**, *25* (9), 1157–1174 DOI: 10.1002/jcc.20035.

(101) Bayly, C. I.; Cieplak, P.; Cornell, W.; Kollman, P. A. A Well-Behaved Electrostatic Potential Based Method Using Charge Restraints for Deriving Atomic Charges: The RESP Model. *J. Phys. Chem.* **1993**, *97* (40), 10269–10280 DOI: 10.1021/j100142a004.

(102) Jorgensen, W. L.; Chandrasekhar, J.; Madura, J. D.; Impey, R. W.; Klein, M. L. Comparison of Simple Potential Functions for Simulating Liquid Water. *J. Chem. Phys.* **1983**, *79* (2), 926–935 DOI: 10.1063/1.445869.

(103) and, T. F.; Kollman*, P. A. Application of the RESP Methodology in the Parametrization of Organic Solvents. **1998** DOI: 10.1021/JP9717655.

(104) Brouwer, A. M. Standards for Photoluminescence Quantum Yield Measurements in Solution (IUPAC Technical Report). *Pure Appl. Chem.* **2011**, *83* (12), 2213–2228 DOI: 10.1351/PAC-REP-10-09-31.

(105) Owens, D. K.; Wendt, R. C. Estimation of the Surface Free Energy of Polymers. *J. Appl. Polym. Sci.* **1969**, *13* (8), 1741–1747 DOI: 10.1002/app.1969.070130815.

(106) Kaelble, D. H.; Moacanin, J. A Surface Energy Analysis of Bioadhesion. *Polymer (Guildf).* **1977**, *18* (5), 475–482 DOI: 10.1016/0032-3861(77)90164-1.

(107) Shirley, D. A. High-Resolution X-Ray Photoemission Spectrum of the Valence Bands of Gold. *Phys. Rev. B* **1972**, *5* (12), 4709–4714 DOI: 10.1103/PhysRevB.5.4709.

(108) Moulder, J. F.; Chastain, J. *Handbook of X-Ray Photoelectron Spectroscopy : A Reference Book of Standard Spectra for Identification and Interpretation of XPS Data*; Physical Electronics Division, Perkin-Elmer Corp, 1992.

(109) Lejars, M.; Margaillan, A.; Bressy, C. Synthesis and Characterization of Diblock and Statistical Copolymers Based on Hydrolyzable Siloxy Silylester Methacrylate Monomers. *Polym. Chem.* **2014**, *5* (6), 2109 DOI: 10.1039/c3py01603j.

(110) Charles, L.; Lejars, M.; Margaillan, A.; Bressy, C. Fragmentation Pathways of Methacrylic Homopolymers with Labile Trialkylsilyl Ester Side-Groups - A Mass Spectrometric Investigation of the RAFT Process. *Int. J. Mass Spectrom.* **2012**, *311*, 31–39 DOI: 10.1016/j.ijms.2011.11.015.

(111) Duong, T. H.; Bressy, C.; Margaillan, A. Well-Defined Diblock Copolymers of Poly(tert-Butyldimethylsilyl Methacrylate) and Poly(dimethylsiloxane) Synthesized by RAFT Polymerization. *Polym. (United Kingdom)* **2014**, *55* (1), 39–47 DOI: 10.1016/j.polymer.2013.11.034.

(112) Duong, T. H.; Briand, J. F.; Margaillan, A.; Bressy, C. Polysiloxane-Based Block Copolymers with Marine Bacterial Anti-Adhesion Properties. *ACS Appl. Mater. Interfaces* **2015**, *7* (28), 15578–15586 DOI: 10.1021/acsami.5b04234.

(113) Aguilar, R.; Gallardo, A.; Ferna, M. In Situ Quantitative 1 H NMR Monitoring of Monomer Consumption: A Simple and Fast Way of Estimating Reactivity Ratios. **2002**, 2036–2041.

(114) Perrier, S.; Haddleton, D. M. In Situ NMR Monitoring of Living Radical Polymerization. In *In Situ Spectroscopy of Monomer and Polymer Synthesis*; Springer US: Boston, MA, 2003; pp 125–146.

(115) Pound, G.; McLeary, J. B.; McKenzie, J. M.; Lange, R. F. M.; Klumperman, B. In-Situ NMR Spectroscopy for Probing the Efficiency of RAFT/MADIX Agents. *Macromolecules* **2006**, *39* (23), 7796–7797 DOI: 10.1021/ma061843z.

(116) Bressy, C.; NGuyen, M. N.; Tanguy, B.; Ngo, V. G.; Margaillan, A. Poly(trialkylsilyl Methacrylate)s: A Family of Hydrolysable Polymers with Tuneable Erosion Profiles. *Polym. Degrad. Stab.* **2010**, *95* (7), 1260–1268 DOI: 10.1016/j.polymdegradstab.2010.03.017.

(117) Lejars, M.; Margaillan, A.; Bressy, C. Synthesis and Characterization of Diblock and Statistical Copolymers Based on Hydrolyzable Siloxy Silylester Methacrylate Monomers. *Polym. Chem.* **2014**, *5* (6), 2109 DOI: 10.1039/c3py01603j.

(118) Yebra, D. M.; Kiil, S.; Dam-Johansen, K. Antifouling Technology—past, Present and Future Steps towards Efficient and Environmentally Friendly Antifouling Coatings. *Prog. Org. Coatings* **2004**, *50* (2), 75–104 DOI: 10.1016/j.porgcoat.2003.06.001.

(119) Taddei, S. Macromolecular Engineering of Nanostructured Polymer Film Surfaces, PhD Thesis, University of Pisa, 2016.

(120) Duc, C.; Vlandas, A.; Malliaras, G. G.; Senez, V. Wettability of PEDOT:PSS Films. *Soft Matter* **2016**, *12* (23), 5146–5153 DOI: 10.1039/C6SM00599C.

(121) Martinelli, E.; Guazzelli, E.; Bartoli, C.; Gazzarri, M.; Chiellini, F.; Galli, G.; Callow, M. E.; Callow, J. A.; Finlay, J. A.; Hill, S. Amphiphilic Pentablock Copolymers and Their Blends with PDMS for Antibiofouling Coatings. *J. Polym. Sci. Part A Polym. Chem.* **2015**, *53* (10), 1213–1225 DOI: 10.1002/pola.27554.

(122) Hempel. Product list http://www.hempel.co.uk/en-GB/products/hempasil-x3-87500 (accessed Sep 16, 2017).

(123) Bressy, C.; Briand, J.-F.; Compère, C.; Réhel, K. Efficacy Testing of Biocides and Biocidal Coatings. In *Biofouling methods*; Wiley-Blackwell, 2014.